Hydrocarbon Pollution Detection & Quantification using Hyperspectral Remote Sensing and Geophysics

Regina Adokailey Brown

March, 2009

HYDROCARBON POLLUTION DETECTION & QUANTIFICATION USING HYPERSPECTRAL REMOTE SENSING AND GEOPHYSICS

by

Regina Adokailey Brown

Thesis submitted to the International Institute for Geo-information Science and Earth Observation in partial fulfilment of the requirements for the degree of Master of Science in Geo-information Science and Earth Observation, Specialisation: Applied Earth Science – Geo-Engineering

Thesis Assessment Board

Prof. Dr. F. D. van der Meer	Chair
Prof. Dr. J. van der Kruk	External Examiner
Dr. H. M. A. van der Werff	First Supervisor
Prof. Dr. F. D. van der Meer	Second Supervisor
Thi Tam Nguyen	Advisor (PhD student)
Drs. T. M Loran	Observer (AES Course Director)

INTERNATIONAL INSTITUTE FOR GEO-INFORMATION SCIENCE AND EARTH OBSERVATION
ENSCHEDE, THE NETHERLANDS

Disclaimer

This document describes work undertaken as part of a programme of study at the International Institute for Geo-information Science and Earth Observation. All views and opinions expressed therein remain the sole responsibility of the author, and do not necessarily represent those of the institute.

Abstract

Due to a global demand for energy and industrialization, there arises an annual increase in soil and groundwater contamination worldwide; which remains a major environmental problem. Since crude oil and its refined products are used around the world, hydrocarbon contamination can be expected anywhere which may occur during their handling, transportation or production. Due to the devastating effects of hydrocarbon pollution, early detection is of utmost importance. However, most methods used in curbing such damaging effects are usually conventional, including site investigations, sampling and analytical techniques which are time consuming, laborious and expensive. The main objective of this study is therefore, to quantify and map the extent and levels of hydrocarbon pollution in soil at Assen in the Northeast of the Netherlands; using a combination of hyperspectral remote sensing and geophysics which have been known from several studies to be rapid, non-invasive, time- and cost- effective techniques.

The methodology was by measuring spectra from vegetation using the ASD and applying different vegetation indices to identify vegetation stresses. Mid- and near- (shortwave) infrared spectra of soil samples taken at 0.5meter depths, till 8m depth from two different boreholes; – one from the centre of the plume and the other at the side of the plume, were measured using the FTIR spectrometer. Using absorption feature parameter analysis, absorption band positions and absorption band depths were extracted from soil spectra to identify and "quantify" hydrocarbon pollution. The last technique employed is bulk geophysical resistivity surveys from which "true" resistivities were obtained of the subsurface which may be associated with hydrocarbon pollution.

Results showed that, vegetation indices could be used as proof of the presence of hydrocarbons; and hydrocarbon pollution ("quantity") information could be extracted from soil spectra. Resistivity was also able to delineate "probable" pollution zones. Integration of vegetation indices and resistivity results showed almost no correlation with the correlation coefficient R^2 of 0.01. Integration of soil spectra results with resistivity results yielded a correlation coefficient R^2 of 0.55. A visual integration of results from vegetation and soil spectra was also assessed. A validation of soil spectral analysis with chemical analysis data resulted in a coefficient of correlation R^2 of 0.16 for wet samples and R^2 of 0.34 for dry samples.

Keywords: Hydrocarbon pollution; mid-infrared; shortwave- infrared; absorption feature parameters; REP; NDVI; OSAVI; bulk resistivity

Acknowledgements

Many are the individuals who through their support, encouragement and help, have contributed in getting this research to a successful completion and to whom I would forever be grateful. My first thanks goes to God Almighty and to Him be all glory for the strength and guidance granted me to accomplish this work. My sincerest gratitude also goes to the Netherlands government, who through the Netherlands Fellowship Program (NFP) offered me the needed sponsorship and opportunity to broaden my knowledge at ITC. I also extend my profound gratitude to my organisation, the Geological Survey Department of Ghana, and especially my former and current directors Messrs Amoako and Adjei-Duodu and to my immediate boss Mr. Kwame Boamah for their encouragement.

My deepest and sincerest gratitude goes to my supervisors Prof. Dr. Freek van der Meer and Dr. Harald van der Werff without whose suggestions, comments, and guidance this work wouldn't have been accomplished. Thank you very much for your constructive criticism and encouragement during the whole of the thesis period. I say, I can't thank you enough and would remain forever grateful to you.

To Dr. Mark van der Meijde, Mr. Chris Hecker, Drs. Boudewijn. de Smeth and Mr. H. Wilbrink, I can't thank you enough for your help and guidance during my field and laboratory work. Thank you very much. To Dr. David Rossiter, I say thanks for your help in acquisition of the soil map and for the translation from Dutch to English. My gratitude also goes to the NAM Oil Company for allowing me to use their field in this research and for the validation data. I am very grateful to PhD students Tam Nguyen and Mila Luleva for their advice and support.

I would like to extend my deepest gratitude to the past and present course directors of AES, Dr. Paul van Dijk and Drs. Tom Loran and to the entire staff of the AES department for sharing your knowledge with us. I say am really very grateful to you. I am very much grateful to the entire ITC staff and staff of the ITC International Hotel as well as to the library staff for their support and help during my stay and study at ITC. Thanks a lot for your wonderful support. Also to my classmates and Ghanaian friends, am very grateful for your help and support and the nice times we shared together.

Finally, my special thanks goes to my husband Patrick Mensah, daughter Ruby-Annelyn for leaving you at that tender age, my sister Agatha Brown for taking care of Maame, and to all my other siblings Adina, Robert, Ernest and Herbert and the rest of the family for their tireless support, love, encouragement and sacrifice in allowing me to follow this program. To you all I owe this achievement. Thank you.

Dedicated to my late parents and siblings, for your toil in helping me reach this far.

Table of contents

List of figures

List of tables

List of abbreviations

AGI	Advanced Geosciences Incorporated
ASCII	American Standard Code for Information Interchange
ASD	Analytical Spectral Devices
BTEX	Benzene Toluene Ethylbenzene Xylene
FTIR	Fourier Transform Infrared
GPR	Ground Penetrating Radar
HC	Hydrocarbon
MIR	Mid Infrared
NAM	Nederlandse Aardolie Maatschappij
NDVI	Normalized Difference Vegetation Index
NIR	Near Infrared
OSAVI	Optimized Soil Adjusted Vegetation Index
PAHs	Polycyclic Aromatic Hydrocarbons
REP	Red edge position
SWIR	Shortwave Infrared
USGS	United States Geological Survey
VES	Vertical Electrical Sounding
VIS	Visible (wavelength region)

1. Introduction

1.1. Background and Significance

Environmental contamination is a major problem of global concern, causing severe environmental and economic damage. Several factors may account for contamination, including accidental or even a deliberate release of organic and inorganic chemicals into the environment. Contaminated sites may include, surface and subsurface mining areas, industrial areas, crude oil production and petroleum refining facilities with e.g. methane (Etiope and Klusman, 2002) and benzene (C_6H_6). According to Serrano et. al. (2008), groundwater and soil contamination increases annually due to a global demand for energy and industrialization. Accidental spills or leakage, of underground storage tanks or pipes of crude oil and its refined products can therefore, be expected anywhere; during their handling, transportation or production, since they are used globally.

An installation by the Nederlandse Aardolie Maatschappij (NAM), a Dutch Oil Company, for transportation of benzene, toluene, ethylene and xylene (BTEX) condensates; in Assen have been noticed to be leaking. A survey by the NAM Oil Company with borehole data indicated a high concentration of hydrocarbon (HC) leakage into the soil (NAM, 2006). The leakage has developed into a pollution plume which may have adverse effects on the soil as well as the environment. The release of HCs can cause a narcotic effect and may cause a person to react irrationally. According to (PSA, 2008), hydrocarbon leakages may be an important factor with respect to long-term health effects; and stated that releases may entail high concentrations of compounds such as benzene. They noted that, benzene is carcinogenic, though mechanisms leading to the development of cancer are mostly unknown, but could not rule out the fact that, a brief exposure to high levels of it (benzene) could contribute to high risk of cancer. Due to the devastating effects of hydrocarbon leaks, early detection is of utmost importance.

To curb such damaging effects, most countries follow a methodology in detecting and treating contaminated sites. Methods used are usually conventional, including; site investigation, sampling and analytical techniques. Since hydrocarbon pipelines and storage tanks usually cover wide areas, the costs for field sampling and chemical analysis can be economically enormous. Many innovative 'state-of-the-art' techniques for leakage detection have been implemented, as for example stated by Geiger (2006) that, leak detection (and localization) systems (LDS) are to be installed with fluid-transporting pipelines, due to their hazardous nature. Fuchs and Riehle (1991) have also mentioned the effectiveness of acoustical techniques of leak detection. These systems of detection may, however,

fail with time or at any time. Additionally, environmental and municipal bodies, as well as oil companies and governments, may wish to have a monitoring system which in some way, is non-failing, and efficient to avoid the danger posed when hydrocarbon leakage goes undetected. Oil companies also get permission easily when they are able to show new monitoring activities.

Due to the expensive, destructive, time-consuming and laborious nature of detection when conventional methods are adopted (Nie et al., 2007; Zirnig et al., 2002) ; a field of remote sensing known as hyperspectral remote sensing has been used in several areas of leakage detection. Hyperspectral remote sensing also referred to as, imaging spectroscopy or imaging spectrometry (van der Meer and de Jong, 2001) is the "acquisition of images in hundreds of registered, contiguous spectral bands such that for each picture element of an image it is possible to derive a complete reflectance spectrum" (Goetz, 1992).

A study by (Horig et al., 2001) to detect hydrocarbons from oil-contaminated soil, was able to establish that, hyperspectral remote sensing is an efficient tool in HC detection, stating that, direct detection and location of HCs with respect to their spectral characteristics, does not require a HyMap atmospheric correction. Kuhn et al. (2004) demonstrated and confirmed the work done by previous researchers that, hydrocarbon-bearing materials could be detected; due to the characteristic absorption features observed when use is made of imaging spectrometry.

In ITC, remote sensing has been used widely in detecting HCs, as for example established by Scholte et al. (2005), that hyperspectral remote sensing is a relatively fast and cheap method in identifying hydrocarbons on volcanic mud surfaces, and from which they concluded that, hydrocarbon activity maps for exploration geology can be created and that, produced images could be used as alteration maps to guide in field investigations. Researchers like Noomen (2007), White (2007) and Winkelmann (2005) also investigated the use of imaging spectroscopy for the detection of HC gases, via vegetation. Noomen et al.(2008) demonstrated that, changes in plant and canopy reflectance may be an indication of gas pipeline leakage, though it could not be proven that, the reflectance change was due to lack of oxygen. Using field and imaging spectroscopy for detecting hydrocarbon liquid seepages due to a pipeline leakage in the Groningen and Friesland Provinces of the Netherlands have also been conducted by van der Meijde et al. (2005, 2006) and van der Werff et al. (2008) from which there was a conclusion that, there was a correlation between spectrally anomalous areas of vegetation and geochemically detected pollution.

Other non-invasive, non-destructive, time- and cost- effective methods for HC leakage detection are geophysical methods. Geophysical techniques, such as Ground Penetrating Radar (GPR) and Electrical Resistivity/ Conductivity (van der Meijde et al., 2008) have been widely used in

environmental investigations, such as hydrocarbon pollution detection. Atekwana et. al. (2004a) tried to assess a relationship between bulk conductivity measurements and geochemical analysis data of a hydrocarbon-impacted aquifer, where they concluded that, a combination of geophysics with biogeochemistry is able to delineate areas of microbial activity effects. Grandjean, (2006) has used seismic reflections in the characterization of a contaminated subsurface site from which there was a correlation in results with available bore hole data. Ground penetrating radar has been used to detect hydrocarbons within fracture zones in resistive zones in the USA e.g.(Grégoire et al., 2006). Fomenko et. al. (2008) have been able to detect groundwater contaminated sites due to hydrocarbons from geophysical studies, i.e. Nuclear Magnetic Resonance (NMR). Using in-situ vertical resistivity probes, Atekwana et al (2004b) were able to conclude that, higher bulk conductivity measurements, had a direct relation with light non-aqueous phase liquid (LNAPL)-impacted zones. Atekwana et. al. (2000) again concluded from an investigation that, much success have been attained, by applying geoelectrical techniques to hydro-geologic, monitoring of contaminant as well as remediation studies.

From the above discussions and more especially from ITC projects on pipelines, it can be established that, remote sensing and geophysical techniques have been widely used in pollution detection in many researches; though many recommendations have been made for a further investigation into the use of remote sensing and geophysics in plant stress analysis and pollution detection. For that reason then, this study aims to focus on quantifying pollution directly, from soil in the Assen area after detection; by integrating hyperspectral remote sensing in combination with absorption feature analysis and geophysical profiling methods, to fully understand the surface expression of spectral features relative to the subsurface.

1.1.1. Impacts of Hydrocarbons on the environment

Though hydrocarbon seeps may be an indication to underground hydrocarbon-bearing reservoirs, they also cause pollution to the environment (Luyendyk et al., 2005). According to the Petroleum Safety Authority (PSA), Norway (2008), hydrocarbon leaks may be a major accidental potential; citing an example of 167 lives being lost at the destruction of the Piper Alpha platform on the UK continental shelf in 1988. The PSA have also cited an example of the death of two people in 2003, after having inhaled high concentrations of hydrocarbons at a British hydrocarbon facility. Readman et al. (1992) and Sauer et al. (1993) have indicated the damage done to marine ecosystems caused by the spillage of petroleum products during the 1991 Gulf war. According to Etiope and Klusman (2002) methane (CH_4) plays an important role in the greenhouse gas effect as well as in the ozone layer depletion, and hence contributing to global warming (van der Meer et al., 2000).

1.1.1.1. Hydrocarbon seepage effects on soil

Pipeline leakages leave anomalous concentrations of hydrocarbons in the soil, hence causing a wide range of changes in the natural soil environment. Serrano (2008), has stated that, mainly aliphatic

hydrocarbons, when leaked into soils, remain persistently in the soil and causes major deterioration to the soils' physical properties, as well as changes in microbe populations. Hydrocarbon-impacted soils also causes alteration in mineralogy of soil, as well as in microbiological, biogeochemical and geobotanical anomalies which may be visible in the soil surface expression (Schumacher, 1996). Seepage of hydrocarbons could also affect soil oxygen significantly as indicated from a study by Steven et al. (2006), that, soil oxygen was considerably depleted due to a displacement by methane gas. Soil contamination due to oil spills is a limiting factor to fertility of soils and hence, crop productivity (Onwurah et al., 2007).

1.1.1.2. Effects of hydrocarbon leakage on vegetation

Plant growth is very much affected due to concentrations of hydrocarbons in the soil environment (Mendoza, 1998; Yuan L. et al., 1990). According to Morard and Silvestre (1996) significant "injuries" are caused to plants due to lack of oxygen in the root environment; thereby affecting their water and nutrient uptake (Urrestarazu and Mazuela, 2005). A study by Leyval and Binet (1998), have also shown that, the growth and survival of plants affected by polyaromatic hydrocarbons (PAHs) like benzene depended on the species of plant. Oxygen deficiency and an increase in carbon dioxide (CO_2) caused soybean plants to die as indicated in a study by Boru et al. (2003). They also showed that, plants which did not die showed severe symptoms of leaf chlorosis (less greenness in leaves due to chlorophyll deficiency) as well as root death.

Plants have shown visible symptoms of reduced growth and chlorosis due to increased natural gas from leaks and this is usually noticed as a decline in vegetation health or known as vegetation anomaly. Spectral responses of affected plants have shown increased reflectances in the visible (VIS) wavelengths and decreased reflectances in the near-infrared (NIR) (Smith et al., 2004a; 2004b) resulting in a shift of the slope between the red and NIR regions, referred to as the 'red-edge position' (van der Meer and de Jong, 2001). According to Noomen et al. (2008), visible changes in reflectance properties of vegetation above HC gas leakage points could serve as an indicator of gas leakage.

1.2. Research Problem

HC leakages can establish locally anomalous zones that favour the development of a wide range of chemical and mineralogical changes in soils and could cause severe danger; by affecting plant health and having subsequent effect on humans through food chains. Fuel hydrocarbon companies also lose much in revenue due to leakage. Early detection is therefore of utmost importance.

Hyperspectral remote sensing has been applied absolutely in the detection of hydrocarbon leakage; e.g. in the MSc. thesis of Batkhuyag (2008) and Cundill (2008), they tried to map pollution by means of abnormal vegetation response. Batkhuyag (2008) recommended that, a further research was needed to confirm the possibility of using reflectance spectroscopy in identifying benzene-induced plant stress. Cundill (2008), also recommended that future studies should investigate the migration of pollutants in the soil with respect to migration towards the surface. In this study therefore, we try to map pollution directly in soil at different depths (from a soil core) and establish a quantitative relationship between soil organic pollution and spectroscopic (soil and vegetation) properties.

Since geophysical and remote sensing techniques have proved to be time- and cost- effective, as well as non-destructive and non-invasive; correlating results from these two techniques will be done to quantify the pollution in this area. Numerous studies have also been limited to affected localized areas; however, this research would compare it to affected areas using hyperspectral images.

1.3. Research Objectives

The main objective of this study is to quantify and map the extent and level of HC pollution, in soil in the Assen area using a combination of field spectrometry, hyperspectral image and geophysical surveys (resistivity surveys).

1.3.1. Specific Objectives

- To develop statistical relationships between soil organic pollution (type, level) and spectroscopic soil properties
- To develop physical and statistical relationship between in-situ derived geophysical parameters and spectral reflectance
- To use spectra from anomalous (stressed) vegetation as an indicator of the presence of hydrocarbons in the soil
- To design and develop an integrated approach that links surface and subsurface measurements of soil pollution (direct, indirect) to derive an integral quantification of soil pollution

1.4. Research Questions

- Will there be a gradient in absorption features of soils taken at different depths (3D) in a borehole indicating less to highly polluted surfaces, and can these be quantified?
- How can geophysical measurements be related to spectra of soils taken at different depths?
- Can vegetation spectra be used as an intermediate source of information to link the surface to the subsurface using a HyMap Image?

- Will there be differences when expected results drawn from field spectrometry measurements are compared to the hyperspectral image of the contaminated site?

1.5. Research Hypothesis

- Using information about the pollution from drilling and laboratory analysis, it will be possible to draw a correlation and estimate the extent of the toxic anomalies. Without any ground validation the cause of the anomalies can not be determined.
- Sampling locations of geophysical and spectroscopic measurements will be partly overlapping thus, allowing a comparison between the two completely different methods
- Spectra parameters indicating vegetation health can be used as an intermediate source of information to link the surface to the subsurface
- Fewer differences are expected when spectrometry measurements are compared to the acquired HyMap image of the contaminated site.

1.6. Thesis Structure

The thesis covers field work preparation, field data collection and post field work activity which is summarised into eight chapters as follows: This chapter covers an introduction which specifies the significance of detecting and quantifying pollution in contaminated areas, using less costly, rapid, less labour intensive techniques like remote sensing and geophysics. Chapter two looks at a literature study of work done by previous researchers on identification of hydrocarbon contaminated sites by their characteristics and the use of techniques in their identification which is also adopted in this study. Chapter three encompassed the materials and methods used in this thesis. Vegetation indices are used in analysing plant stress in chapter four; whereas chapter five looked at the Geophysical investigation carried out. Chapter six then comprised the soil analysis of hydrocarbon and chapter seven integrated all results from the three techniques. Chapter eight then sums up the concluding remarks and recommendations of the thesis.

The field work preparation included reading of literature from previous works and reading of manuals in the operating of instruments to be used during the field data collection.

2. Literature Review

2.1. Characteristics of Hydrocarbon contaminated sites

Hydrocarbon contaminated sites are often identified when there is accidental spillage, gradual losses in the course of inventory, and when industrial facilities are earmarked for decommissioning, sale or for redevelopment. A historical hydrocarbon contamination long in the ground may often have weathered through a range of physical, chemical and microbiological processes (Pollard et al., 2004).

Locating hydrocarbon impacted sites have mostly been done through the observation of alterations of soil mineral components and their relations to soil organic components spatially. High groundwater levels in contaminated areas may leave sites with a change in colouring of soils surrounding tanks or reservoirs. Some HCs that solidify at low temperatures and liquefies at high temperatures, do remain visible at the surface as described by Winkelmann (2005) that, a marshland was affected due to spilled crude oil during the Iraq-Iran war in the 1980s. He also stated that, some parts of the contaminated area are sparsely covered by a particular species of grass.

If contaminated sites are covered by vegetation, depending on the concentration and mixture of the HC present, the vegetation may exhibit vegetation stress and may differ from vegetation in other uncontaminated areas. The difference in growth and other characteristics of plants is often regarded as vegetation anomaly (Winkelmann, 2005).

2.1.1. Spectral response of vegetation to stress

The use of remote sensing for detecting vegetation stress is based on the response of vegetation to incoming solar radiation. Numerous biological processes which take place in plants derive their main source of energy from the sun (solar radiation). Generally, healthy plants have a similar spectral response with respect to solar radiation; however, there may be differences in background soil types, plant morphology and physiology as well as in climate type (Li et al., 2005).

According to van der Meer and de Jong (2001), about 28% of absorbed energy known as photosynthetically active radiation (Hwang et al.), is used in conversion to high-energy compounds as well as for photosynthesis. The optical properties of leaves are however, dependent on factors such as, leaf surface area and cellular structure, thickness, water content, as well as on biochemical

composition. The leaf photosynthetic pigments such as chlorophyll and carotenoid absorb incoming radiation depending on the amount of light absorbed or transmitted and on its wavelength.

The spectrum of healthy plants tends to have a characteristic high reflectance in the near-infrared region of solar radiation and strong absorptions by pigments in the visible region, due to strong internal scattering of incident light from cell walls and intercellular spaces (Li et al., 2005). However, when plants become stressed or with advanced growth, an internal tissue (mesophyll) begins to dry out and cell walls disintegrate, resulting in considerably reduced intercellular surface area and pore space. Ageing and stressed plants therefore tend to reflect more red light, than in the near-infrared region in comparison to healthy plants. Due to the loss of photosynthetic pigments therefore, a greater reflection of red light is observed which results in less absorption.

2.1.2. Spectral characteristics of hydrocarbon impacted soils

Soils get contaminated due to buried pipeline spills or even during oil explorations for crude oil deposits. Numerous researchers have however, investigated the use of spectroscopy in identifying hydrocarbon impacted soils for e.g. (Cloutis, 1989; Horig et al., 2001; Li et al., 2005; Orlov et al., 1993). It has been established that there's an overall decrease in reflectance properties of oil impacted soils within the VIS-NIR (about 400-800nm) wavelength regions e.g. (Orlov et al., 1993). Most hydrocarbons have been found to have absorption features in the 3.4 μm, 2.35μm, 1.75μm and 1.35μm wavelength regions. According to Winkelmann (2005), however, substances such as plastics and asphalts show similar absorption features as those displayed in most hydrocarbons and hence care should be taken when measuring spectra of hydrocarbon–impacted soils. White (2007) also indicated the possible changes in soil structure such as changes in pH, mineralogy, organic matter content as well as water retention; when impacted by pipeline leakage and which had subsequent effects on reflectance properties of stressed plants. In addition chemical and mineralogical changes in soils which occur due to hydrocarbons have shown characteristic spectral features when soil surface expressions show some anomalies (Schumacher, 1996).

2.2. Methods for detecting polluted sites

Manifestations of hydrocarbon seepage on the surface can be observed in many forms, including anomalous concentrations of hydrocarbons in sediments and waters, microbial and botanical anomalies; mineralogic alterations; and changes in magnetic, electrical and seismic properties of near-surface sediments. These varied surface expressions have led to the development and usage of surface exploration techniques of which, some are biological (Oesch-Bartlomowicz et al., 2005; Yakubu, 2007; Young and Phelps, 2005); geochemical (Mukherjee et al., 2005; Nganje et al., 2007); explicitly geophysical and remote sensing methods (Atekwana et al., 2004a; Atekwana et al., 2004b; Bammel

and Birnie, 1994; Horig et al., 2001). The exploration methods used usually depends on several factors including the sites of investigation as well as the concentration of the hydrocarbon at the site. Recent studies suggest that an integrated approach of a combination of surface and subsurface exploration methods could reduce development risks and costs (Schumacher and Abrams, 1996).

2.2.1. The application of Remote Sensing in hydrocarbon detection

A variety of surface exploration remote sensing methods have been applied with success in the detection of hydrocarbons, for e.g. Martinez and Moreno (1996) and Topouzelis et al. (2007), have reported of the use of Synthetic Aperture Radar (Fabio Fava, 2004) images in detecting oil spills in a marine environment, stating its effectiveness in terms of low cost and less time.

"*Integration of remote sensing and GIS techniques has proved a powerful tool for analyses of the environmental sensitivity for potential oil spills*" (Abdel-Kader et al., 1998).

Xu et al. (2007) have reported on the use of hyperspectral remote sensing for exploring for gas by determining the reflectance spectra of surface anomalies from absorption band parameters and absorption features of HC from the field. A Landsat ETM+ image dataset and experimental spectra from GER 3700 spectroradiometer has been used for extracting information on the coasts of the United Arab Emirates. Results indicated that, spectra from the visible and near infrared images can be used in assessing thicknesses of hydrocarbon spills (Howari, 2004). An investigation from a Landsat thematic mapper and a confirmation from a ground truth data indicated anomalous concentrations of gaseous hydrocarbons in soils and the effects it has posed to the soils' natural environment in the Tucano Basin in Brazil (Almeida, 2002). Van der Meer et al. (2002) have shown that, changes in geochemical properties of soils and rocks caused by microseeps from oil and gas, could be observed indirectly from hyperspectral images. Effects of hydrocarbon microseepage on a wheat field and associated soil was tested by Yang et al. (1998) using field spectrometry as well as geochemical studies. Results revealed that, spectra of wheat on oil-fields shifted about 7nm towards longer wavelengths than off oil-field wheat spectra.

Stuart (1993) has also shown that, discovery of gas leaks such as methane and hydrocarbon liquid mixtures could be done by applying remote sensing techniques such as laser remote spectroscopy. A spatial spectral classification algorithm has been used by van der Werff et al. (2006) in detecting mineralogical and botanical alterations resulting from natural microseepage from hydrocarbons. Returned results indicated a success in the use of the image processing algorithm used. For reaching far regions of the world for difficult field observations in zones of HC alteration, Petrovic et al. (2008) have developed a technique based on a combination of remote sensing techniques (ASTER multispectral imagery, spectroscopy and SAR) and geochemical analysis for easy observation. In

general, the characteristic major absorption features of HC around 1.18- 1.38µm (Xu et al., 2008) and also 1730 nm (Heiden et al., 2007), as well as between 2350 - 3400nm have been used with respect to their detectability using imaging spectroscopy as shown in figure 2.1 (King and Clark, 1989).

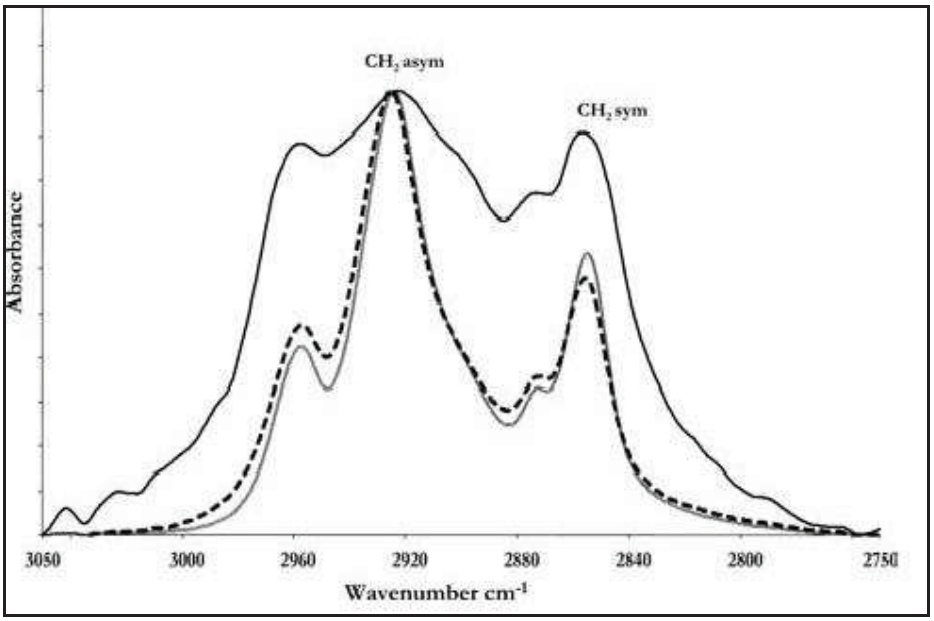

Figure 2.1: Hydrocarbon absorption band positions after Cann and Spikes (2005)

2.2.2. Hydrocarbon detection by geophysical means

Geophysical techniques have been used in the location of oil-bearing reservoirs as well as in the detection of HC polluted sites over the years. For example, seismic reflection studies have been able to evaluate and assess seismic reflection data for the location of hydrocarbon reservoirs as explained by Pitas and Venetsanopoulos (1993). In Antarctica, several geophysical techniques have proved to be efficient in locating hydrocarbon spills. Due to the fragile nature of many Antarctica soils, obtaining samples for site characterisation of contaminated areas using conventional methods may cause much more damage than expected. Therefore, non-destructive and non-invasive geophysical surveys – electromagnetic and ground penetrating radar (GPR) were employed to provide information on the nature of the subsurface; which proved to be very good techniques in locating the movement of hydrocarbon contaminants (Pettersson and Nobes, 2003).

Susceptibility measurements from magnetic surveys were used in the identification of anomalous regions within a sedimentary zone in the South China Sea; according to Hao et al. (2001), this method, proved to be very effective in detecting alteration zones caused by marine oil-gas seepage. Locating hydrocarbon-saturated rocks using shear wave velocities in combination with other geophysical parameters was performed with success as reported by Benson and Wu (1999).

The contamination of groundwater by immiscible hydrocarbon substances such as dense non-aqueous phase liquids (DNAPL) is a major environmental issue. However, the detection of DNAPL in the subsurface by GPR, was easily conducted where anomalous contrasting areas of contaminated areas was distinguished from uncontaminated regions (Hwang et al., 2008). Also, according to Atekwana et al. (2004a), hydrocarbon-impacted aquifers having zones of enhanced microbial activity could be located easily using bulk conductivity measurements of electrical resistivity.

2.2.2.1. The use of Electrical Resistivity Survey

Resistivity surveys are mostly used in the study of horizontal and vertical discontinuities in the electrical (resistivity) properties of the subsurface. Fields of application of this method includes exploration of bulk properties of materials, underground water supplies, and in engineering and construction site investigations. Other applicable areas are in waste site and pollutant investigations, cavity and karst detection, glaciology, geological and archaeological investigations *(from lecture notes)*.

One of five standard electrode arrays is usually used in resistivity data acquisition. These include Wenner, Schlumberger, dipole-dipole, pole-dipole and pole-pole. Generally, a set of profiling measurements for different depth levels constitutes the measurement procedure; which is carried out by means of a multielectrode system, for e.g.(Šumanovac et al., 2003). Electrodes are grounded at equally spaced intervals along a profile, and connected with suitable cables to a resistivity meter.

In ground resistivity measurements, a DC electric current is injected into the ground through two electrodes, say A and B. The resulting electric potential is then measured between two other electrodes, say M and N. An apparent resistivity value is derived from the injected current, a measured voltage and a geometric factor *(from lecture notes)*.

The measured data is then inverted to produce true subsurface resistivity distribution which is then correlated to the subsurface property by interpretation. Figure 2.2 shows a typical resistivity profile array.

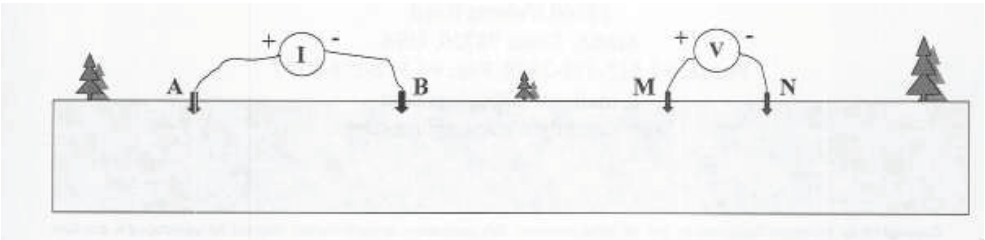

Figure 2.2: A typical resistivity profile array after (AGI, 2007) from lecture notes

The measured apparent resistivity value is represented as:

$$\rho = \frac{K\Delta V}{I} \quad \text{……(2.1)}$$

; ρ = Apparent resistivity (Ohm-m); I = Injected electric current (A)
ΔV = Measured potential difference (V); K = Geometric factor (m)

Where the geometric factor K, which depends on the arrangement of the four electrodes, is given by:

$$K = \frac{2\pi}{\frac{1}{AM} - \frac{1}{AN} - \frac{1}{BM} + \frac{1}{BN}};$$

A, B = current electrodes
M, N = potential electrodes

The Wenner and Schlumberger arrays have been known to provide good vertical resolution and generally, high signal-to-noise (S/N) data, but have moderate lateral resolution capabilities and are susceptible to electromagnetic coupling between cables connecting the current and potential electrodes; as compared to the pole-dipole and dipole-dipole arrays which are known to have good lateral resolutions. Several authors however, recommend that, for requirement of a good vertical resolution, the Wenner array could be an appropriate option, for 2D surveying (Stummer et al., 2004), and for good lateral resolutions, the dipole-dipole array could be an option. However, for surveying completely unknown or new areas, or for a high resolution requirement in all directions, it is not obvious which electrode configuration or combination of configurations could be used. A possibility would therefore, be to record data with a variety of electrode configurations and invert the combined data set.

Two well-known traditional DC electric explorational layouts are the vertical electrical sounding (VES) and the electric profiling (EP) techniques (Giao et al., 2003). Practically, both methods commonly employ the 4-electrode configuration. The VES method, however, is used for investigating the change of apparent resistivity with depth; where the electrode spacing is gradually extended on both sides apart from the central point. The EP method on the other hand, uses an electrode configuration of constant spacing that is moved along a profile line to detect lateral heterogeneity. A limitation though, of the VES method is that of an assumption of a layered medium, which is not very practical in many situations. The EP method also has a limitation of obtaining information in only one-depth level. However, the VES is employed in this study.

2.3. The Study area

The study area (fig. 2.3) is near Assen, located in the North-east of the Netherlands. It lies between latitudes 53^0 02' 10" and 53^0 02' 15" N and longitude 6^0 35' 40" and 6^0 35' 55" E.

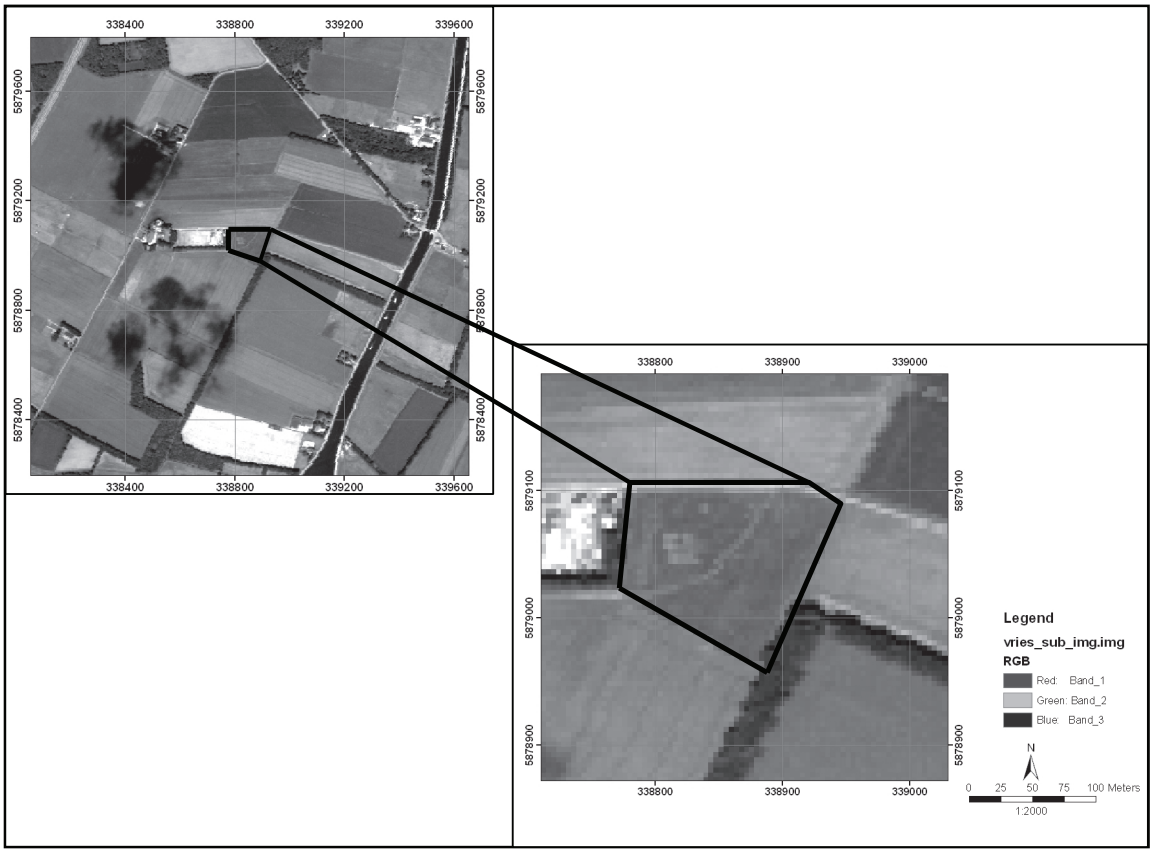

Figure 2.3: The study area showing the contaminated field from a HyMap image

The area covers approximately 100 * 80 sq. meters and geologically comprises mainly of (late – mid) Pleistocene sediments which are silty fine (cover) sands with or without boulder clay, reworked from tertiary marine clays. These soils (fig 2.4), are podsols, (Steur and Heijink, 1980), are well-drained and have fairly high humus content of about 4 -15%. The humus layer in this area is about 15-30cm, and has a pH range of between 4.5 – 5 (Stichting voor Bodemkartering (STIBOKA), 1991).

The Nederlandse Aardolie Maatschappij (NAM, Dutch Oil Company) has an installation in this area, which is expected to be leaking from a point source and hence has heavily polluted the environment (NAM, 2006). According to the NAM Oil Company, the area under investigation located in Assen has been known to be contaminated by Benzene, Toluene, Ethylbenzene and Xylene (BTEX) for over three years now from borehole investigations; and this has developed into dispersion plumes shown to have strong gradients in pollution levels (fig 2.5). The pollution gradients range from high to low from red to blue.

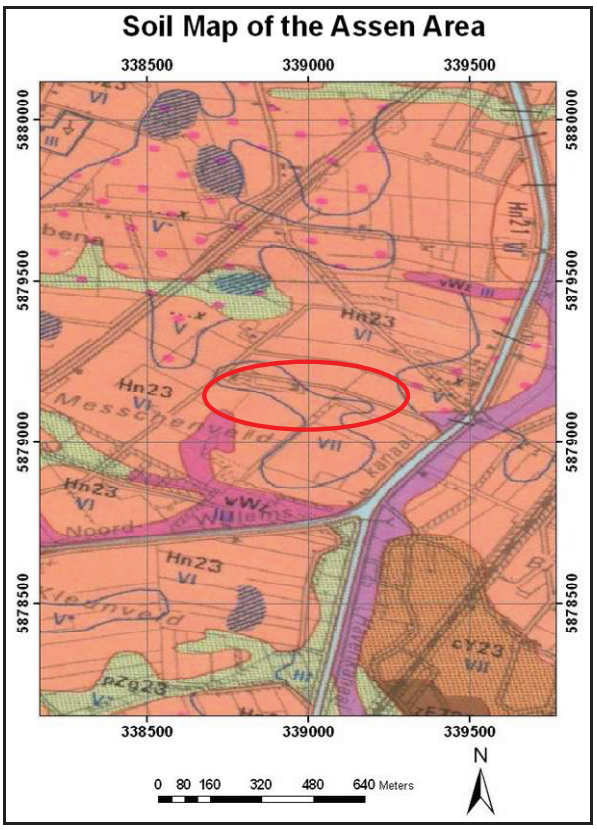

Figure 2.4: Soils of the study area- podsols (Hn23) shown in orange and bound in red (source:(Stichting voor Bodemkartering (STIBOKA), 1991))

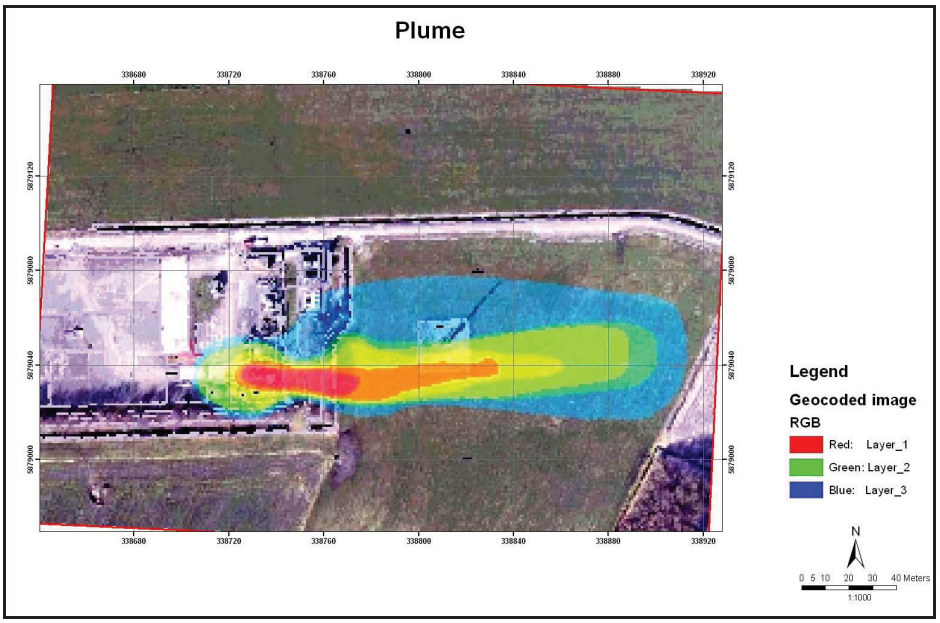

Figure 2.5: Pollution plume in Assen measured by groundwater sampling showing high to low concentration of BTEX from red to blue (source:(NAM, 2006))

3. Materials and Methods

3.1. Materials

The data used in this research is divided into two: secondary data extracted from ITC projects which were carried out in Groningen and Freisland Provinces, the Netherlands in 2004, 2005, and from MSc. and PhD theses; and primary (field) data in Assen which was done by the field work.

Table 3.1 Data extracted from different sources & obtained for use in this research

Data	Type of data	Source
Literature	Secondary data	ITC MSc. , PhD theses & projects
Study area (HyMap image)	Secondary data	From supervisors
Field spectrometry measurements	Primary data	Field work
Geophysical survey measurements	Primary data	Field work
Soil samples from drilling	Secondary data	Oil Company ordered by ITC

3.2. Methodology

The methodology followed in this research work consisted of four (4) main steps as follows:
1) Field data collection (field spectroscopy, geophysical profiling, and soil sampling techniques); 2) Data processing and analysis; 3) Results and Discussions); 4) Data validation.

3.2.1. Field spectroscopy measurement technique

Using the ASD FieldSpec Pro FR (spectrometer), spectra of vegetation (grass) were collected during two different field campaigns, both in July, 2008 for comparisons. One was done during a flight over the area with a HyMap sensor and the other was conducted three weeks after. During the flight, canopy reflectance measurement was done at 1m height above the ground (by Harald van der Werff); whereas that after the flight made use of a contact probe. The spectrometer had the following specifications:

Spectral Range	350 - 2500 nm
Spectral Resolution	3 nm @ 700 nm 10 nm @ 1400/ 2100 nm
Sampling Interval	1.4 nm @ 350 - 1050 nm 2 nm @ 1000 - 2500 nm
Scanning Time	100 milliseconds

Source: (ASD, 2008)

The ASD spectrometer was used in combination with a High Intensity Contact Probe (with internal light source and spot size of 10mm) and a calibrated spectralon reference panel (Labsphere Inc.); for measurements after the flight. Calibration of the ASD spectrometer was done by optimization, using the reference panel, to absolute reflectance. Reflectance signatures of vegetation in the area were then taken. To ensure that there are no signatures from the underlying soil, the vegetation was pushed underfoot, before measurements took place. After a couple of measurements, the spectralon panel was used in re-calibration, and measurements continued until all measurements were completed.

3.2.2. Resistivity profiling measurement technique

The resistivity imaging method was chosen for use in the investigation of the pollution plume due to its effectiveness in numerous environmental applications. The Schlumberger array was preferred for use because of its provision for very good vertical resolution since the pollution plume was expected to be at a certain depth; and it being able to determine the variation of electrical conductivity with depth (*from lecture notes*). It also has an advantage in areas with horizontal layering as well as with high water tables such as the case in this area.

The measurements were done to determine differences in contrast between 'supposedly clean' and 'unclean' areas. The Sting R1 resistivity meter from Advanced Geosciences Incorporated (AGI) was used with about 100mA of current sent and about 400mV of voltage recorded, however, most measurements, go to about 50mA.

With electrode spacing pegged at every 3m away and a total of 28 electrodes, and with transect spacing being 4.5 meters away from each other, x-coordinates were up to 81 meters long and y-coordinates were up to 40.5 meters, summing up to a total of 81 * 40.5 square meters. The first transect started at 15 meters away from the fence (on the eastern side) of the flare which is sited at approximately one-third of the field. In effect, a 10 by 28 rectangular survey grid was taken to visualize the pollution plume in 3-dimensions (3D) (i.e. 280 electrodes); however, this was performed as a set of parallel 2-dimensional (2D) surveys. With this method, measurements were conducted along one profile as in a 2D survey but combined into one as in 3D, also known as the 3-D roll-along technique (Dahlin and Bernstone, 1997). The 2D surveys were orientated parallel (28) and perpendicular (10) to the pollution plume. Measurements recorded on each profile were 138 and 1650 measurements were taken in total. Depth of investigation however depends on the electrode spacing as well as the profile length; hence in this case, the total profile length is 81 meters and the depth of investigation is about 20% or 0.2 of the total array length.
A combination of spectroscopy and resistivity profiling transects are as shown in figure 3.1 below:

Transects as shown on the field

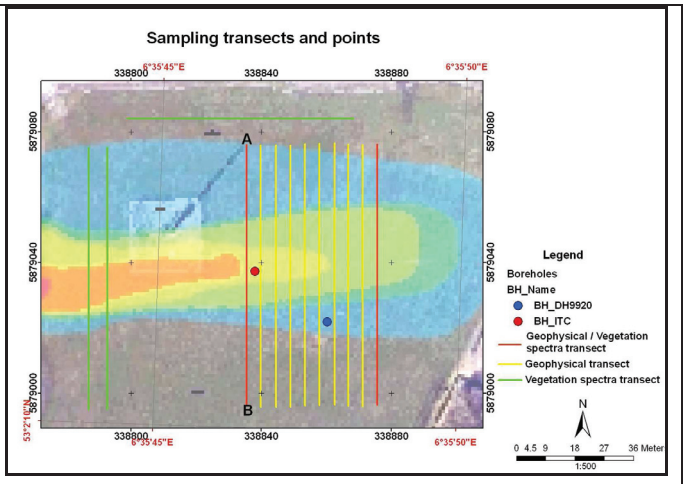

Transects as shown on Google earth image

Figure 3.1: Transects shown on the field and on HyMap image in North-South direction

Some observations made on the field are explained as follows:

- On transect 1 (A-B), at about 41m away, the ground looked relatively very wet, with some groundwater surfacing in the grass
- On transect 6, i.e. at 22.5 meters in y-direction, at electrode 18 (54m in x-direction on the profile), was a large hole in the ground
- The colour of the grass at this particular site was a bit more brownish compared to the surroundings
- Between transects 9 and 10, i.e. between 36 and 40.5 meters in y-direction, were mole hills and these were at electrode position 12 (36m in x-direction on both transects)

3.2.3. Soil sampling data acquisition technique

Since the field in question belonged to the NAM Oil Company, there were a few restrictions on data collection and more specifically, with the soil sample data collection. Soil samples were however drilled (by the oil company) from two locations – one at the centre of the pollution plume (BH-ITC); and the other, at a "supposedly clean" area, at the side of the plume (BH-DH9920). Both were 8meters deep and at every 0.5meters, soil samples were taken for laboratory analysis.

The samples taken for laboratory analysis at every 50 cm (0.5 m) were stirred thoroughly to have a relatively homogenous soil as a representative of that depth and delivered in tightly-capped bottles.

A summary of the methodology described above is as shown in figure 3.2 below:

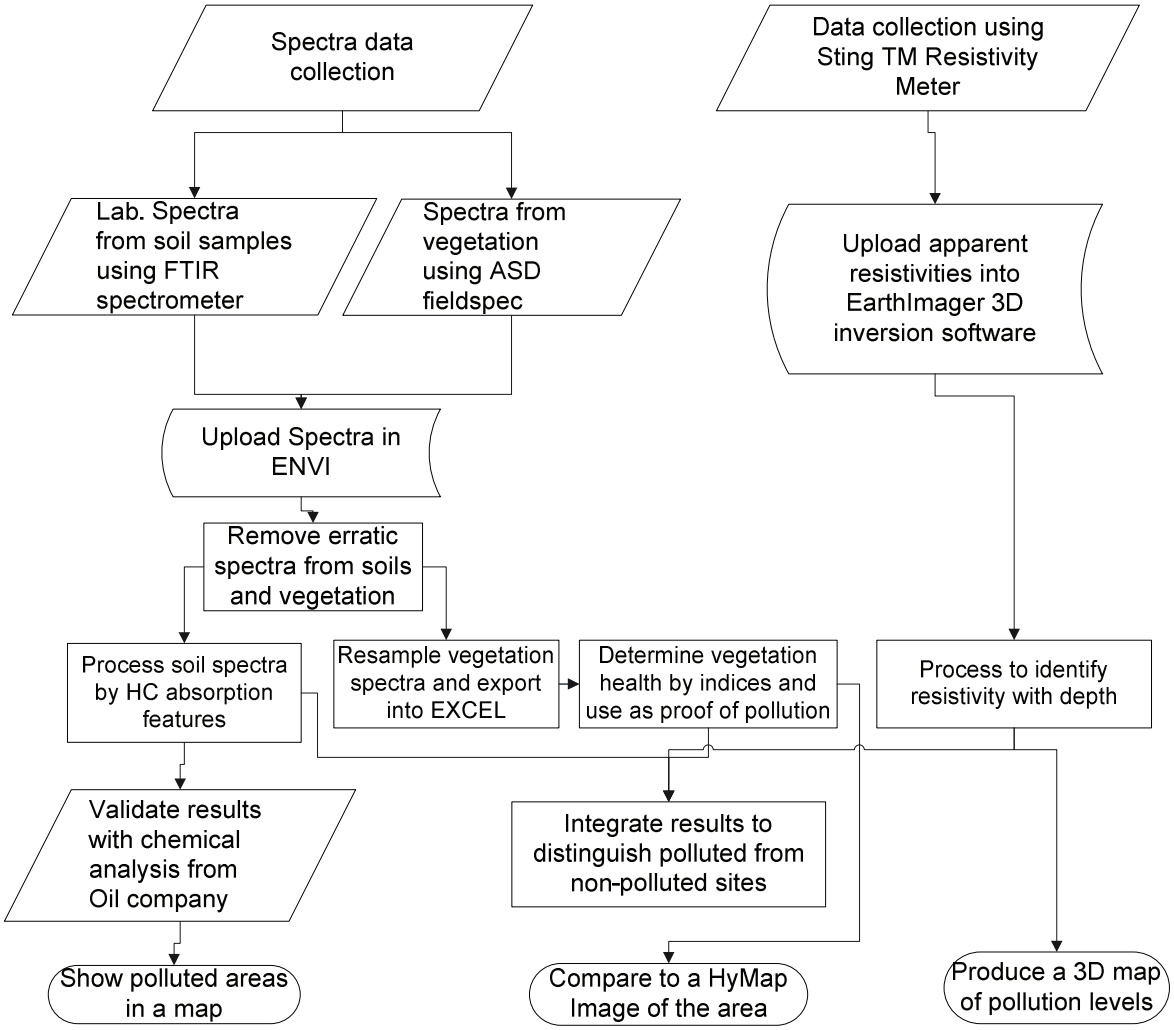

Figure 3.2: A summary of methodology used in this research work

3.2.3.1. Soil spectra measurements

The soil samples obtained were prepared for measurement of possible hydrocarbon spectra. Each bottled sample was again stirred thoroughly to ensure homogeneity of the represented depth and then, a considerable amount was placed in a Petri-dish and heaped to the brim. These were relatively wet soils and almost watery so were levelled at the brim.

Spectra were acquired on a Fourier transform infrared (FTIR) lab spectrometer (from Bruker Optics B. V.) fitted with a Rocksolid interferometer and a detector system. The instrument is first warmed by turning on measuring gadgets for about an hour before measurement starts. To ensure that all other

gases are out of the instrument, a purge gas ($N_2(g)$) is turned on to flush out all other gases. Sources, detectors and mirrors, are changed automatically via the associated Bruker proprietary OPUS software. However, a beam splitter for measurement of both the SWIR and MIR wavelength regions, need to be changed by hand.

The laboratory analysis were carried out at room temperature and spectra were acquired (128 scans and repetitions per wet sample or reference) in a range of 650 – 4000cm^{-1} (wavenumber); for measurement in the mid-infrared (MIR) region with an OPUS 6.5 (Bruker optics) software. This was however upgraded to allow an effective measurement range of the shortwave infrared (SWIR) region as well (32 scans and 16 repetitions per wet sample or reference). The repetitions were conducted to obtain considerably good signal to noise (S/N) ratio. All spectra (both MIR and SWIR) which were acquired for each sample were averaged after the completion of measurements leaving each sample with two representative spectra (for MIR and SWIR).

After measurements of the wet samples, all soil samples were dried and re-measured both in the MIR and SWIR. This was done to estimate whether the same absorption features could be observed in both dry and wet samples. The MIR spectra were 128scans and 80 repetitions per dry sample or reference whereas; the SWIR was 32scans and 12 repetitions per dry sample or reference. The same number of scans was performed to allow for a good comparison. The repetitions (MIR) were done for 128 times for the first sample and spectra were averaged for the first 64, 80, 96 and all 128 measurements. The first 80 were considered to give good S/N ratios after averaging, and hence the rest of the samples were measured for 80times and averaged. The SWIR measurements were, however done for 12 repetitions, which were considered to have good S/N ratio (Chris Hecker, personal communication).

Measurements were also done for an open port space, a gold sample, and for distilled water after measurement of the wet samples in the MIR, for comparisons, in case some spectra are found otherwise. For the SWIR region, spectralons (20, 50 and 100) were replaced with the gold sample and the others repeated. However, for the dry samples, the above were repeated with the exception of distilled water.

The unit of measurement which is in wavenumbers (cm^{-1}), was converted to micrometers (μm) by the following conversion; $1\mu m = \frac{10{,}000}{1cm^{-1}}$, but which was done automatically by the Bruker optics software. After conversion noisy spectra for MIR spectra were cut out from a range of 1 – 16.5 μm and for SWIR from 1.1 – 2.8 μm. These were then saved as data point table (.dpt) extension files, which could be assessed in ENVI as ASCII files.

4. Vegetation Indices as plant stress indicators

4.1. Vegetation Spectra Processing from field measurements and HyMap Image

The measured vegetation (grass) spectra from the field were uploaded into ENVI 4.4 (Environment for Visualizing Images) software. A separate spectral library was built for each transect taken.

The HyMap Image was also uploaded for visualization and from which spectra from vegetation from the image was built with respect to coordinates taken from the field measurements. All spectra had wavelength ranges between the visible (VIS) to short wave infrared (SWIR) regions; from about 400 to 2500 nm; and were in reflectance after processing with ATCOR (Atmospheric and Topographic Correction) by DLR (German Aerospace Center).

To perform analysis, spectra were resampled to different wavelengths from which vegetation indices (e.g. Red-edge Position Index (REPI); Normalized Difference Vegetation Index (NDVI); and Optimized Soil-Adjusted Vegetation Index (OSAVI)) were calculated.

4.1.1. Use of indices for analyzing vegetation spectra

Numerous vegetation indices have been devised for use in showing how certain properties of vegetation are affected through their reflectance properties. Leaf component factors which most importantly affect their spectral reflectance include pigments, water, carbon dioxide and nitrogen (Asner, 1998). Vegetation with a high concentration of chlorophyll is generally considered healthy, since it is the most well-known and important pigment causing the green coloration of plant leaves, and having absorption features around 660 and 680nm.

Identifying vegetation anomalies can therefore be observed in chlorophyll concentration of a plant, where anomalous (stressed) vegetation expresses itself in a shift of the so-called *red-edge* (which is the edge observed in spectra between 670 and 780nm wavelength between the absorption minimum in the red and the reflection maximum in the near infrared) (Guyot and Baret, 1988). The red-edge is known to shift towards the blue part of the electromagnetic spectrum when there is less chlorophyll concentration and towards the red part with an increase in concentration of chlorophyll. In vegetation spectra therefore, less chlorophyll concentration may result in a decrease in height of the infrared shoulder due to leaf structural damage as well as an increase in the reflectance of the chlorophyll absorption maximum. The red-edge shoulder also shifts in position towards shorter wavelengths.

Other most well-known and commonly used vegetation index in identifying vegetation anomaly is the Normalized Difference Vegetation Index (NDVI) (Ganguly et al., 2008; Jackson et al., 1983; Momeni and Saradjian, 2007) and the Optimized Soil Adjusted Vegetation Index (OSAVI) (Noomen, 2007; Zarco-Tejada et al., 2004).

The NDVI is used in remote sensing to assess vegetation health by obtaining plant distribution through plant density (Momeni and Saradjian, 2007) and by assessing morphological changes in plants affected by more or less, available soil nutrients. However, to minimize soil and atmospheric background effects especially in hyperspectral images where the NDVI sensitivity is limited, a number of vegetation indices including the OSAVI (Huete, 1988; Rondeaux et al., 1996) were proposed.

The above mentioned indices have been used in this study and are expressed in table 4.1 as follows:

Table 4.1: A summary of vegetation indices used in this thesis

Vegetation Index	Formula	Range of values	Literature
REP	$700 + 40 * \frac{(R_e - R_{700})}{(R_{740} - R_{700})}$	REP values shift towards shorter wavelengths (670-780 nm)	(Baret et al., 1992)
NDVI	$\frac{(\rho NIR - \rho RED)}{(\rho NIR + \rho RED)}$	NDVI values range between -1 and 1	(Boegh et al., 2002)
OSAVI	$1.16 * \frac{(b800 - b670)}{(b870 + b670 + 0.16)}$	OSAVI values range from 0 for very low vegetation cover to 1 for high vegetation cover	(Rondeaux et al., 1996) cited in (Steven, 1998)

R_e is known as the red-edge inflection point given by:

$R_e = (R_{670} + R_{780}) / 2$

R_{670}, R_{700}, R_{740}, R_{780} = spectral reflectance values at the respective wavelengths

ρNIR = spectral reflectance in the Near Infrared band; in this case at wavelength 750nm

ρRED = spectral reflectance in the Red band; in this case at wavelength 705nm

$b800$, $b670$ = spectral reflectance values at the respective wavelengths

Spectra obtained both during and after the flight were processed using the three indices and table 4.2 shows examples of the values obtained from the calculations for each index. The indices were also applied to a HyMap image from which spectra were collected only during the flight; since field measurements were done at the same time of the flight. The respective wavelength values were exported to Microsoft Excel as Ascii files and processed as a spreadsheet.

Table 4.2: The vegetation indices calculated for spectra taken during and after flight

X	Y	Posi-tion	REP after flight	NDVI after flight	OSAVI after flight	REP during flight	NDVI during flight	OSAVI during flight
338787	5879075	1	722.6	0.844	0.815	724.6	0.960	0.847
338787	5879073	2	722.5	0.843	0.814	724.7	0.955	0.852
338787	5879071	3	719.8	0.785	0.753	726.4	0.963	0.865
338787	5879069	4	719.4	0.794	0.758	725.1	0.957	0.843
338787	5879067	5	713.2	0.673	0.623	724.0	0.950	0.839
338787	5879065	6	719.1	0.887	0.857	725.9	0.962	0.850
338787	5879063	7	718.2	0.896	0.850	725.0	0.956	0.859
338787	5879061	8	718.3	0.844	0.804	725.2	0.953	0.863
338787	5879059	9	717.2	0.828	0.785	724.4	0.949	0.855
338787	5879057	10	716.6	0.878	0.825	725.7	0.958	0.863
338787	5879055	11	721.5	0.893	0.871	724.8	0.956	0.862
338787	5879053	12	717.8	0.778	0.711	725.3	0.956	0.851
338787	5879051	13	719.0	0.846	0.797	724.2	0.942	0.859
338787	5879049	14	718.5	0.886	0.849	725.5	0.948	0.876
338787	5879047	15	716.2	0.832	0.782	725.5	0.956	0.866
338787	5879045	16	715.8	0.819	0.756	725.0	0.952	0.875
338787	5879043	17	716.5	0.765	0.686	726.7	0.951	0.865
338787	5879041	18	718.7	0.849	0.813	725.0	0.941	0.862
338787	5879039	19	717.1	0.814	0.767	725.1	0.953	0.877
338787	5879037	20	718.9	0.870	0.844	724.5	0.946	0.884
338787	5879035	21	720.1	0.895	0.870	725.3	0.951	0.873
338787	5879033	22	718.5	0.863	0.822	725.4	0.955	0.873
338787	5879031	23	717.9	0.891	0.850	725.9	0.962	0.869
338787	5879029	24	719.2	0.836	0.805	725.2	0.954	0.884
338787	5879027	25	719.4	0.848	0.817	723.9	0.940	0.882
338787	5879025	26	719.7	0.856	0.826	723.1	0.940	0.883
338787	5879023	27	718.1	0.833	0.799	726.3	0.959	0.885
338787	5879021	28	717.7	0.818	0.768	726.1	0.955	0.876
338787	5879019	29	720.7	0.877	0.861	724.7	0.948	0.873
338787	5879017	30	721.4	0.870	0.844	723.4	0.937	0.871
338787	5879015	31	715.9	0.756	0.697	723.7	0.936	0.866

Since hydrocarbon seepage may have a chemical influence on the soil environment thereby reducing the soil's oxygen concentration and increasing the production of CO_2, it may form organic acids by the production of hydrocarbon-oxidising bacteria. These alterations in the soil's natural environment may affect the soil's pH and redox potential, which may consequently affect their root structure and hence their spectral reflectance (Noomen, 2007).

4.2. Results

4.2.1. Results from field observations

4.2.1.1. Red edge position indices

Red edge position values obtained from the data collected during and after the flight respectively is shown in fig. 4.1 (a) and (b) below. As shown from table 4.2 and on the maps, red edge values ranged from 722 to 727 nm during the flight and from 712 to 723 nm after the flight.

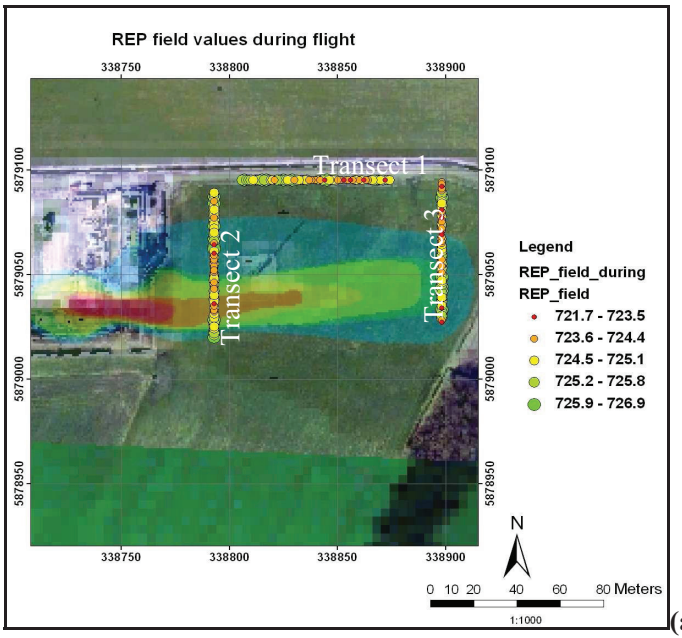

(a)

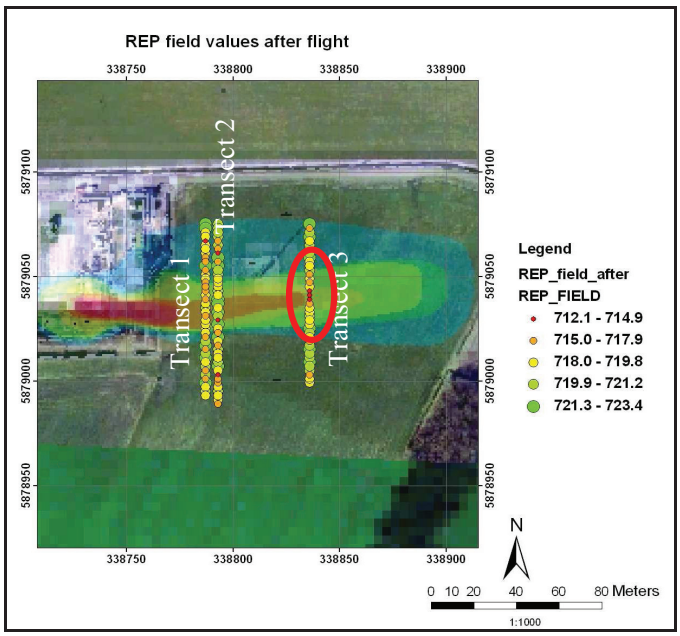

(b)

Figure 4.1: REP field values shows variation in vegetation health for each measured point, from healthy to less healthy from green to red. Red circle shows a similar trend at certain points after the flight

It is also visible from the plots (fig. 4.1) that, most values shifting to shorter wavelengths fall within the pollution plume (which ranges from high to less concentration from red to blue). There are however, some more healthy values falling within the plume after the flight.

4.2.1.2. Normalized Difference Vegetation Indices

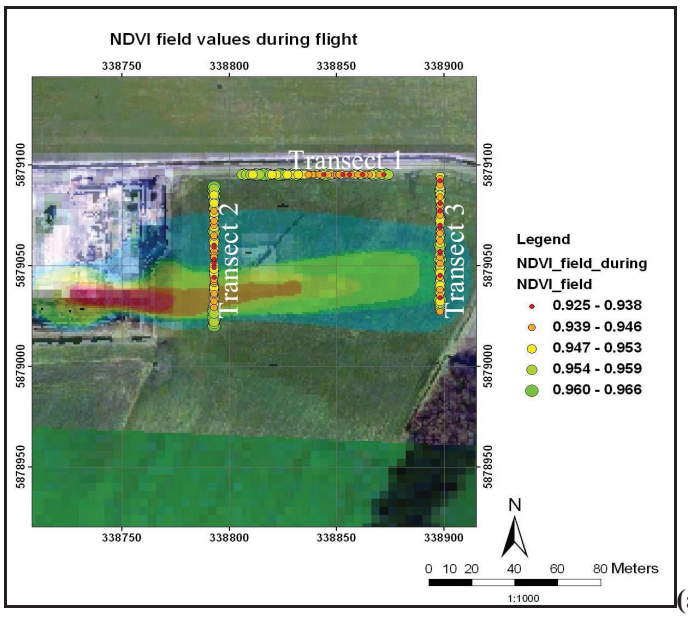

(a)

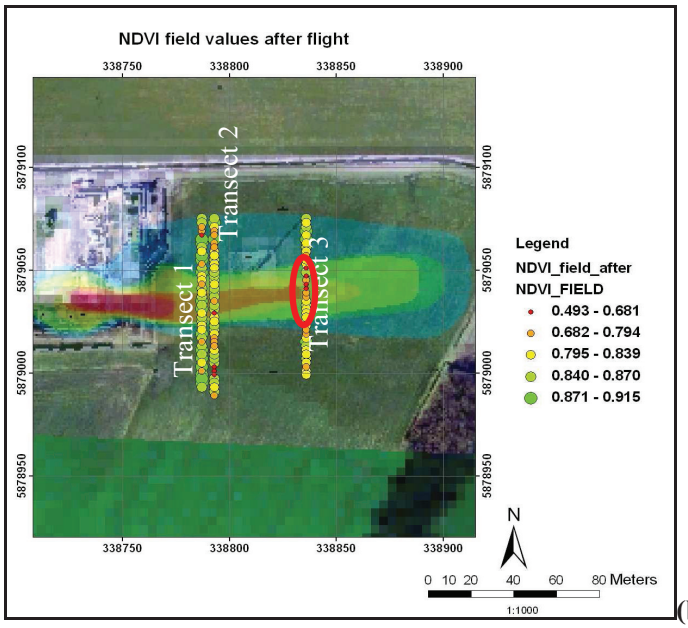

(b)

Figure 4.2: NDVI field values shows vegetation density for each measured point from denser to less dense from green to red. Red circle shows a similar trend at certain points after the flight

In fig. 4.2, plots of NDVI values are presented. Dense vegetation is seen to be within the plume zone during the flight (fig 4.2 (a)) depicted by a range of NDVI values from 0.92 - 0.96 and a few more dense values fall outside the plume; though there are some zones falling outside the plume which also seem to be less dense (transects 1 and 3). Comparatively, NDVI values after the flight (fig. 4.2 (b)) range from very less dense to dense (from 0.49 – 0.91) and do not seem to follow the trend of the

plume, with the exception of transect 3 , which seems to have very low values falling in the plume zone.

4.2.1.3. Optimized Soil Adjusted Vegetation Indices

With the application of the Optimized Soil Adjusted Vegetation Index, values seem to be higher during the flight (ranging from 0.77 – 0.89, fig. 4.3a); than after the flight (from 0.44 – 0.88, fig. 4.3b); the values during the flight seem to indicate a good leaf area cover than after the flight with the exception of transect 3 in fig. 4.3a, which also seems to have less leaf area cover even outside the plume zone.

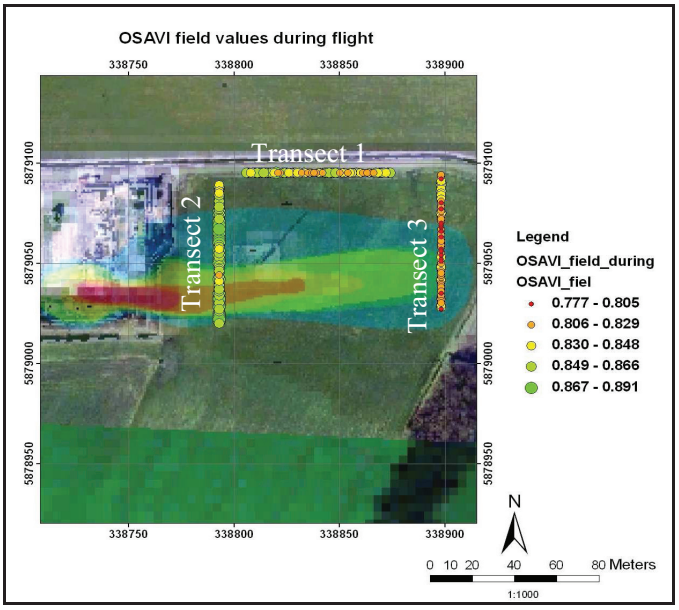

(a)

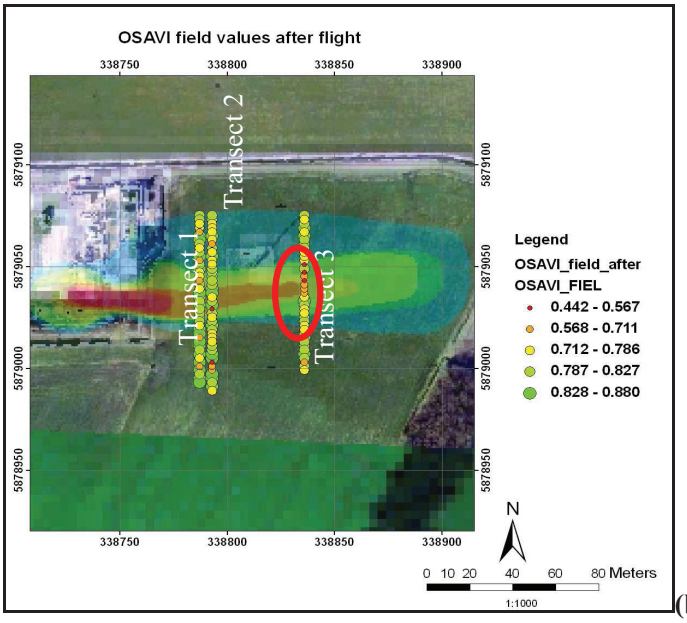

(b)

Figure 4.3: OSAVI field values shows vegetation cover for each individual point from much to less cover from green to red. Red circle shows a similar trend at certain points after the flight

A plot of field spectra measured and from which the above indices were calculated is shown in fig. 4.4. Spectra are compared with that from a standard library (USGS vegetation spectra) to bring out any differences and these are observed in the shape of the shoulders at around 680nm and in the chlorophyll absorption maximum, (van der Meer, 2004).

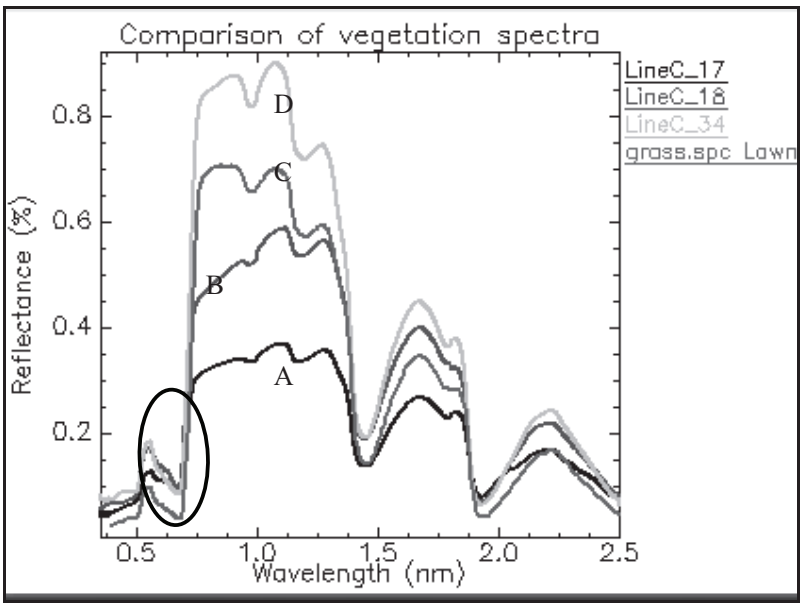

Figure 4.4: Field spectra are labelled as A, B and D and the library spectrum is labelled as C. Differences in the chlorophyll absorption maximum is bound in circle. Field spectra show a decrease in the absorption, whereas spectrum from library has a strong absorption of chlorophyll.

From section 3.2.1, since different measurement methods were adopted; (i.e. use of canopy reflectance measurement at 1m above ground during flight and use of contact probe after three weeks of flight), values obtained from the field measurements and from the image application, were compared to establish correlations. The indices were also applied to the image for the other ground data set, i.e. the one acquired after the flight (after 3weeks).

4.2.2. Results from image observations

4.2.2.1. Red edge position indices

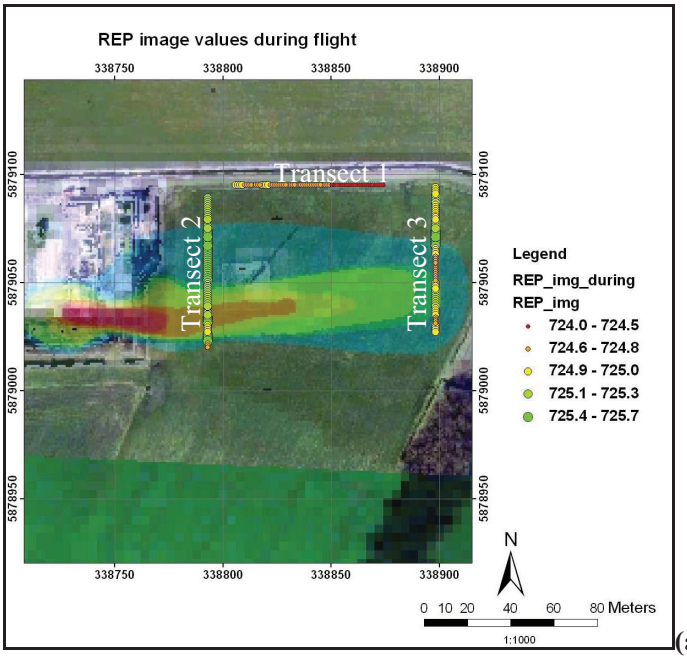

(a)

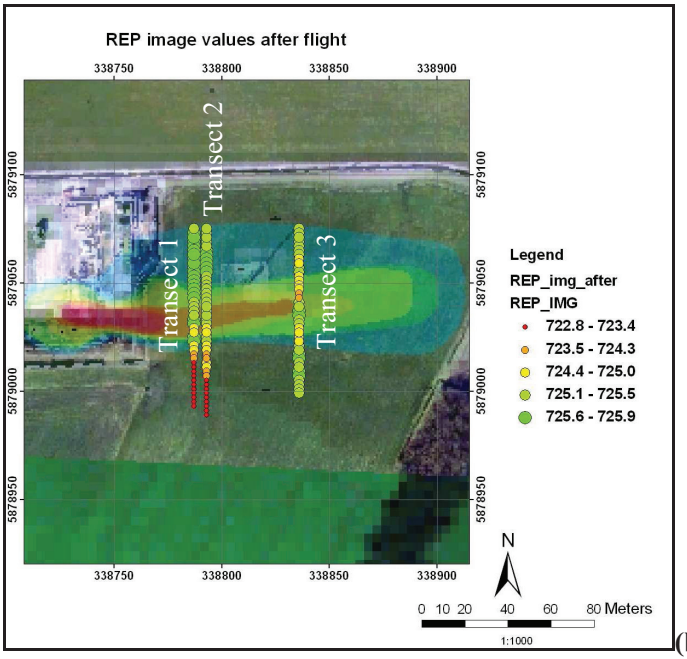

(b)

Figure 4.5*: *In comparison to field values, REP image values show a minor variation during flight but a huge variation after flight in vegetation health for each measured point, from green to red.

REP values from the image ranged from 724 to approximately 726 nm; and comparatively, from 722 to 727nm for the field (fig.4.1) during the flight. Some points falling within the plume show higher values, whereas outside, there are lower values. Image values were however, approximately between. 723 – 726 nm after the flight but comparatively for field values after the flight, they ranged between 712-723 nm.

4.2.2.2. Normalized Difference Vegetation Indices

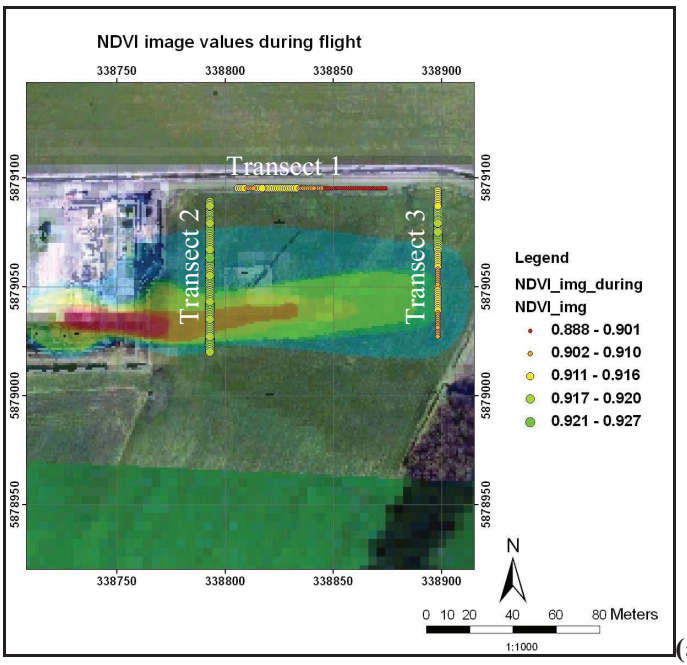

(a)

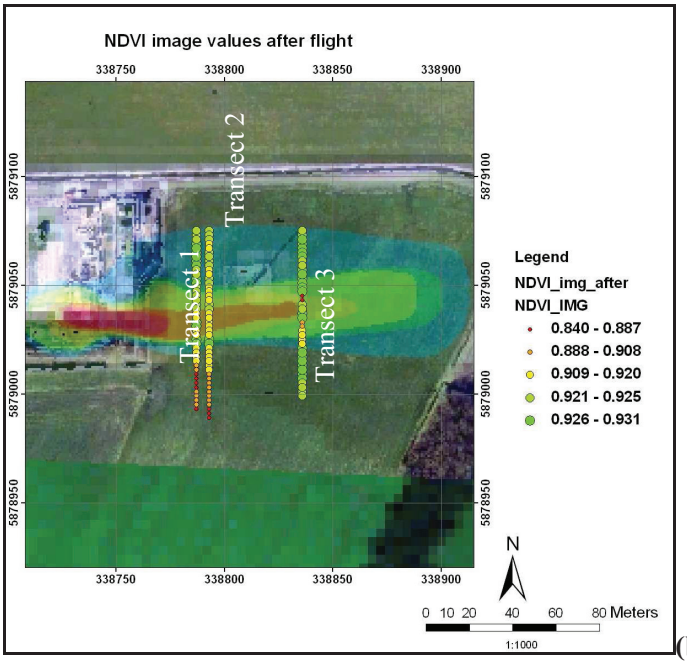

(b)

Figure 4.6: In comparison to field values, NDVI image values show a minor variation during flight but a huge variation after flight in vegetation density for each measured point from green to red.

From figure 4.6, it is observed that, the density of vegetation applied to the image is lesser and ranging between 0.88 and 0.93; comparatively, values from field observations (fig.4.2) during the flight are higher (0.92-0.96). The density of vegetation (from the image) after the flight is higher ranging between 0.84-0.93 and in comparison, field values ranged between 0.49-0.92; though some areas outside the pollution plume are seen to be relatively less dense whilst a few within the plume are higher.

4.2.2.3. Optimized Soil Adjusted Vegetation Indices

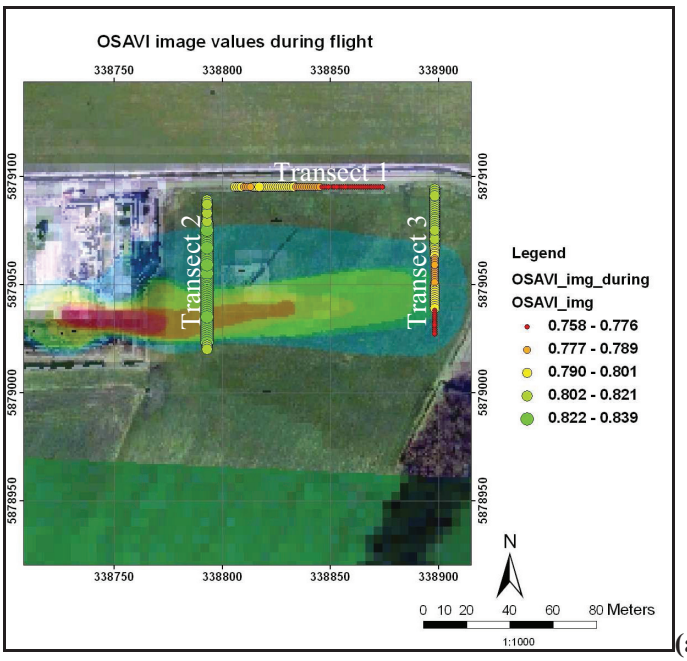

(a)

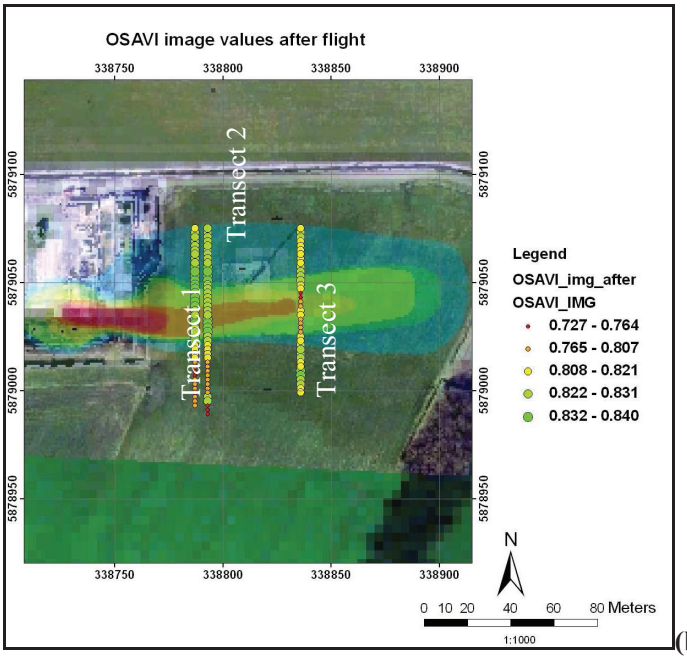

(b)

Figure 4.7: In comparison to field values, OSAVI image values show a minor variation during flight but a huge variation after flight in vegetation cover for each measured point, from green to red.

The value range depicted after applying OSAVI however, did not show much variation in both cases i.e. from the image and field observations. Values ranged between 0.76 – 0.84 for the image; but comparatively from 0.78 - 0.89 for the field (fig. 4.3) during the flight. Values fell between 0.73 - 0.84 for the image after the flight; whereas in comparison field values ranged from 0.44-0.88 Some zones outside the plume seem to have lower values, whereas some points within the plume are higher in value.

4.2.3. Ratios of indices from intersecting transects

To establish a correlation between indices observed from the field for both during and after the flight, a plot of the indices during the flight was done against that after the flight (for transect 2 in both cases since they intersect with each other), but less correlation was observed for all three indices. Fig. 4.8 thus shows an example for the observation for REP index and other indices are shown in appendix1.

Table 4.3: Ratio of indices for field values

X	Y	REP field during	REP field after	REP field ratio	NDVI field during	NDVI field after	NDVIfield ratio	OSAVI field during	OSAVI field after	OSAVI field ratio
338793	5879075	725.5	721.0	1.01	0.956	0.849	1.13	0.866	0.817	1.06
338793	5879073	726.7	720.2	1.01	0.951	0.875	1.09	0.865	0.821	1.05
338793	5879071	725.1	719.8	1.01	0.953	0.815	1.17	0.877	0.780	1.12
338793	5879069	725.3	720.5	1.01	0.951	0.785	1.21	0.873	0.748	1.17
338793	5879067	725.9	716.5	1.01	0.962	0.785	1.22	0.869	0.743	1.17
338793	5879065	723.9	720.9	1.00	0.940	0.875	1.07	0.882	0.837	1.05
338793	5879063	726.3	717.1	1.01	0.959	0.756	1.27	0.885	0.729	1.21
338793	5879061	724.7	713.0	1.02	0.948	0.725	1.31	0.873	0.687	1.27
338793	5879059	723.7	721.9	1.00	0.936	0.829	1.13	0.866	0.809	1.07
338793	5879057	723.9	716.4	1.01	0.945	0.807	1.17	0.836	0.755	1.11
338793	5879055	724.4	723.1	1.00	0.944	0.851	1.11	0.858	0.831	1.03
338793	5879053	724.0	720.5	1.00	0.931	0.816	1.14	0.866	0.785	1.10
338793	5879051	724.2	720.5	1.01	0.932	0.815	1.14	0.873	0.784	1.11
338793	5879049	724.6	718.1	1.01	0.925	0.845	1.09	0.861	0.794	1.08
338793	5879047	725.7	719.3	1.01	0.952	0.856	1.11	0.857	0.816	1.05
338793	5879045	724.6	719.6	1.01	0.951	0.865	1.10	0.864	0.826	1.05
338793	5879043	723.8	720.9	1.00	0.943	0.826	1.14	0.855	0.801	1.07
338793	5879041	724.6	719.3	1.01	0.946	0.840	1.13	0.848	0.806	1.05
338793	5879039	724.9	721.4	1.00	0.947	0.863	1.10	0.857	0.842	1.02
338793	5879037	724.8	721.4	1.00	0.949	0.862	1.10	0.852	0.841	1.01
338793	5879035	723.7	718.2	1.01	0.944	0.787	1.20	0.868	0.736	1.18
338793	5879033	724.1	721.5	1.00	0.951	0.851	1.12	0.873	0.823	1.06
338793	5879031	724.7	720.0	1.01	0.949	0.869	1.09	0.872	0.851	1.02
338793	5879029	724.9	712.1	1.02	0.944	0.493	1.91	0.880	0.477	1.84
338793	5879027	725.1	721.8	1.00	0.961	0.835	1.15	0.849	0.818	1.04
338793	5879025	724.7	719.1	1.01	0.962	0.812	1.18	0.891	0.785	1.14
338793	5879023	725.7	717.8	1.01	0.965	0.848	1.14	0.871	0.806	1.08
338793	5879021	725.7	721.8	1.01	0.959	0.860	1.12	0.871	0.845	1.03

Ratios were therefore, performed over transect 2 in both cases (i.e. during and after), and expected to have no or little differences if they have been affected by the pollution. For all three indices however, values were approximately 1.0 for each individual point measurement, with the exception of coordinate (338793, 5879029) which has an NDVI ratio of 1.91 and OSAVI ratio of 1.84. These values are shown in table 4.3. A plot of the ratios against average index values showed high correlation values with high correlation coefficients R^2 of 0.9338 for NDVI and 0.9047 and 0.6831 for OSAVI and REP respectively.

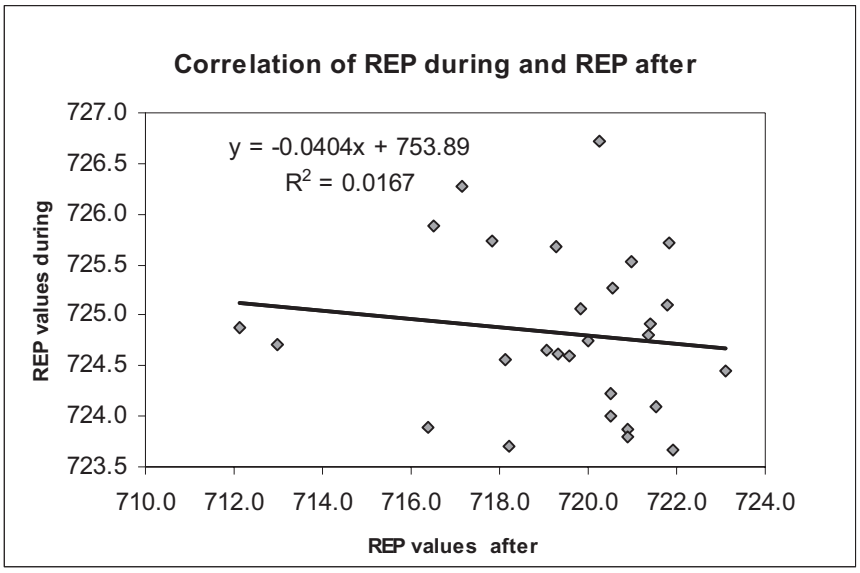

Figure 4.8: A plot of REP values during the flight against values after the flight

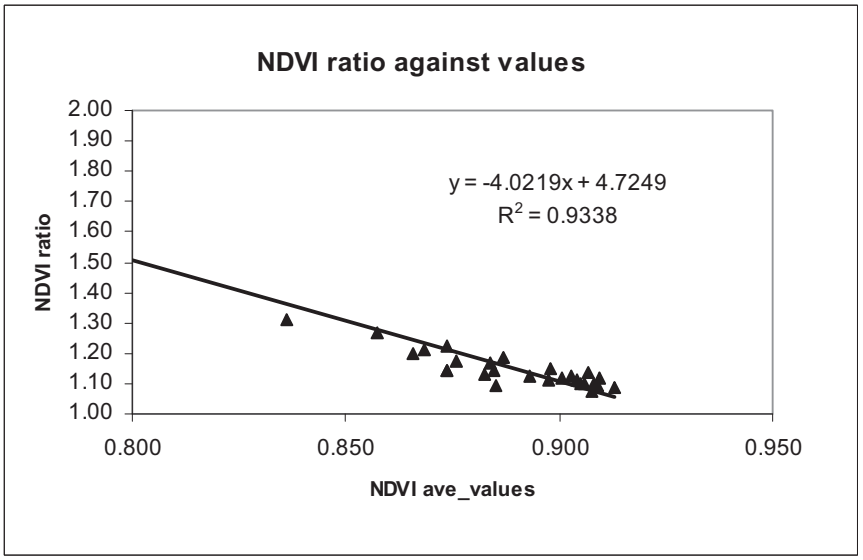

Figure 4.9: A plot of ratio of NDVI indices against NDVI averaged values

The plots shown in figs. 4.9 – 4.11 are NDVI, OSAVI and REP plots of ratio with average values respectively. Figure 4.12 shows a correlation in values of NDVI and OSAVI showing a very high coefficient of determination of R^2 of 0.9397.

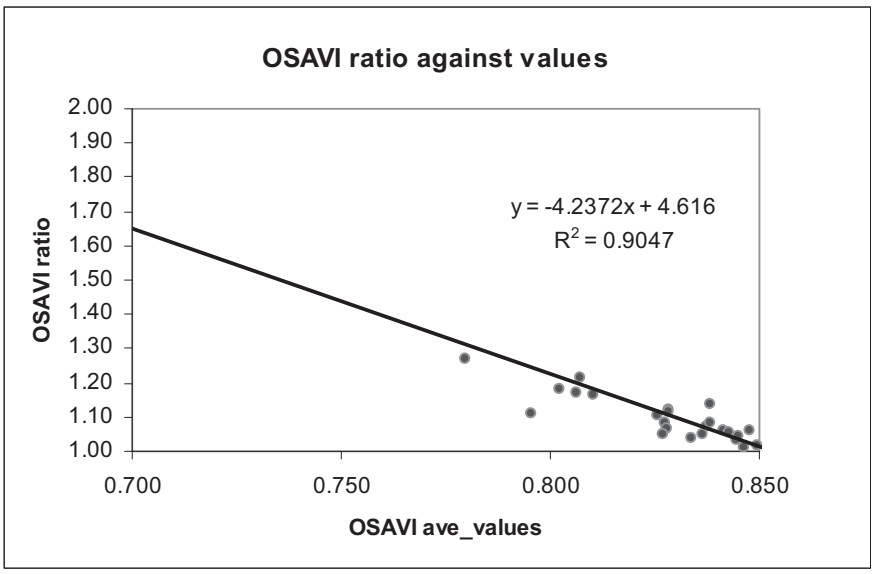

Figure 4.10: A plot of ratio of OSAVI indices against OSAVI averaged values

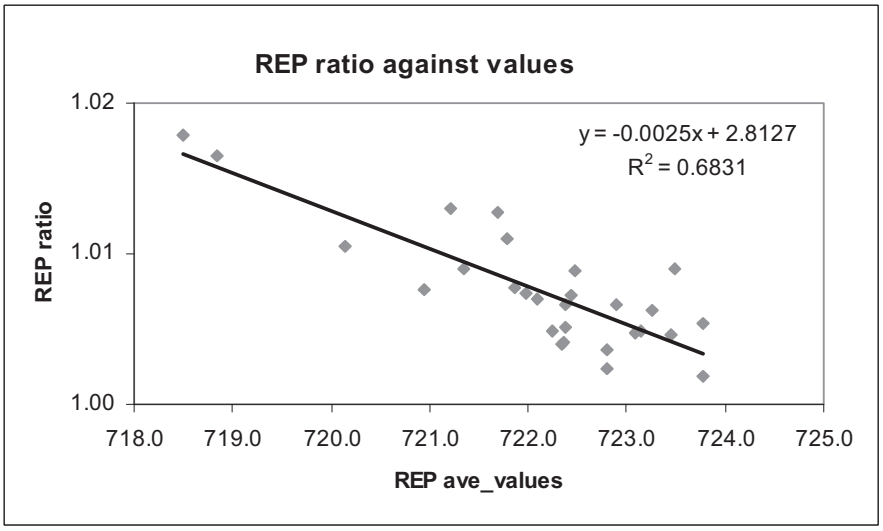

Figure 4.11: A plot of ratio of REP indices against REP averaged values

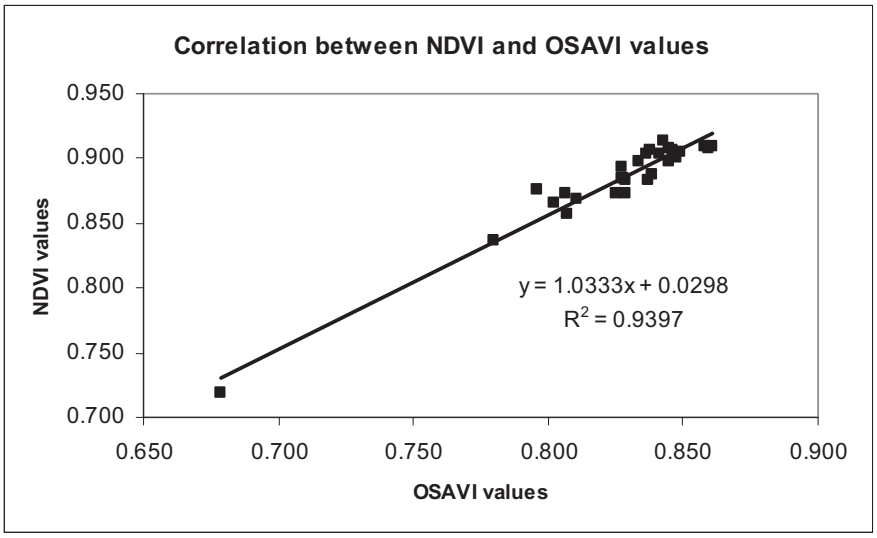

Figure 4.12: A plot of correlation between NDVI and OSAVI

4.3. Discussion

4.3.1. Discussion from field observations

From figure 4.4, it is observed that, spectrum A had a decrease in the height of the infrared shoulder and an increase in the reflectance of the chlorophyll absorption maximum; and comparatively to the grass spectrum (C) from the USGS library, the red-edge shoulder has shifted slightly in position towards shorter wavelengths, which is expected in stressed plants and is in agreement with van der Meer (2004). This may have been caused by the chlorophyll concentration of the grass at that particular point. However, spectrum D (fig. 4.4) which also has a less absorption compared to the standard library (C) seems to be higher in reflectance than the standard library spectrum; this could also be an indication of the chlorophyll content at the particular point.

In fig. 4.1, values of the red-edge during the flight though have shifted toward shorter wavelengths; they are relatively higher (721 – 726nm) than values after the flight (712 – 723nm). The REP values which are expected to fall between 670 and 780nm is as expected and in agreement with previous studies for e.g. (Cho and Skidmore, 2006; Dawson and Curran, 1998; Guyot and Baret, 1988), though shorter wavelengths are seen in values after the flight; and also with the presence of the pollution, more shorter wavelengths were expected to be seen, but which is not the situation in this case.

Since it has been stated by Jarlan et al (2008) that, the higher the NDVI value, the denser the vegetation may be, it is expected that, values falling within the plume would be much less than that falling outside, where the plume may then be said to have had an effect on the growth of the

vegetation. However, the trends in values do not seem to be as expected. During the flight though, some measured points outside the plume (transect 1 and 3) show relatively low values, i.e. 0.92 – 0.94 (fig. 4.2a), though these values are known to be high for a range of -1 to 1 for NDVI as explained by Jones (1996) cited in USGS website. Comparatively however, after the flight, NDVI values are relatively lower i.e. 0.49 – 0.91 (fig.4.2b), with lower values falling within the plume zone and a few outside. The density of vegetation during the flight could be said to be a lot higher than after the flight. Generally, there is not much difference between values from the two ground datasets, with only a couple of lower values; and the value of 0.49 could be an outlier which may have been due to measurement error or a lower shoulder in the spectrum between red and near infrared.

The values from OSAVI applications fell between 0 and 1 with most values closer to 1, indicating higher leaf area cover as explained by, and in agreement with Steven (1998). Values depicted during the flight however, seem to show more leaf area cover (0.77 - 0.89; figure 4.3a) than values observed after the flight (0.44 – 0.88; fig. 4.3b). With the pollution however, it was expected that, values will be closer to 0 than 1, which is not as indicated in this case.

From figs. 4.1 to 4.3 generally, all three indices seem to follow a similar trend showing lower values after the flight at certain points (bound in red circle) than during the flight. Also, transects 1 and 3 seem to show less values during the flight, though transect 1 falls outside the pollution plume.

The pollution plume which indicates zones of high to low concentration (fig.2.5) from red to blue though, has been interpolated from borehole data analysis in 2006. This therefore depicts the pollution from the subsurface and this must have sunk with time down into the groundwater. However, some perennial grasses are shallow-rooted (Schwinning et al., 2005) and therefore the pollution may have had less effect on the grass with time. Not only was there a time difference in the measurement of the two field data sets, but also differences in measurement methods (i.e., the canopy reflectance measurement at 1m height above ground for measurement during the flight; and a contact probe measurement after the flight). Since the difference in measuring method is that big as well as the time of data acquisition, not so much can be said about the pollution since the chlorophyll content of a plant is also a factor in plant stress analysis.

4.3.2. Discussion from comparison of image and field observations

Figure 4.5 shows image values obtained after the application of the REP to individual points measured both during and after the flight. Since the image was acquired at the same time of field measurement, image values during the flight ranged from approx. 724-726 nm, which shows a slight difference to that obtained for the field values (i.e. 722-727 nm) – (with reference to fig.4.1a) . The image values

(approx. 723 – 726 nm; fig 4.5b) after the flight however, differed greatly from that obtained from the field values after the flight (712 – 723 nm- fig.4.1b); however, the value ranges fall within the expected REP value range (670-780 nm) as explained by Guyot and Baret (1988), cited in (van der Meer and de Jong, 2001); and in agreement with results from an investigation carried out by Li et al (2005). The difference in values after the flight, however, may have been due to the different ground data set applied to the image.

NDVI values during the flight from the image ranged from 0.88-0.92 (fig.4.6a) and slightly contrasts with that from the field values (0.92 - 0.96 – fig. 4.2a) during the flight; though both value ranges seem to be in the expected range as discussed by Jarlan et al. (2008). The value range (0.84-0.93) from the image after the flight though, seems to largely contrast to some extent with that from the field values (0.49-0.92) after the flight. These values are also known to be higher as explained by Jones (1996) considering the value range of NDVI values from -1 to 1. This may also be due to the difference in time of acquisition of the two ground data sets. The low value observed after the flight is for only one point which could be due to a measurement error.

Values depicted after the application of OSAVI also follow a similar trend of having a minor variation in range of values from the image i.e. 0.76 - 0.84 as compared to the field values (0.78 -0.89 – fig. 4.3a) during the flight. In contrast however, image values after the flight (i.e. 0.73-0.84) have a wide variation compared to field values after the flight (i.e. 0.44-0.88). These ranges of values however, are higher and depict dense leaf area coverage in agreement with Steven (1998) who demonstrated that, a higher leaf cover fraction had a corresponding higher OSAVI value. However, the difference in measurement method as well as time of acquisition of data may account for the differences in observation.

Generally, since the pixel size of the image is 4 * 4 and the ground data sets were taken at every 1m interval during the flight and at 2m intervals after the flight, the values depicted from figs 4.5 to 4.7 falls within each pixel and seem to be repeated. Furthermore since measurements during the flight was at about 1m above the ground, the differences in values compared to the image are expected and could be said to be acceptable since the image have undergone atmospheric and radiometric corrections. The range of image values depicted after the flight however cannot be expected to be almost as that of the field values, since the field values were taken three (3) weeks after the flight; and also the values represent a different ground data set.

4.3.3. Discussion from correlation plots

From the plots, it is evident that there exists high correlation between ratio values and average values as well as between indices (with reference to fig. 4.12), which gives an indication that, there is not

much difference between the two different data takes and the minor differences could be said to be acceptable since the acquisition times were different. Therefore if indeed there is pollution, the effect on vegetation both during and after the flight seemed not to have changed much. From the correlation plot of REP during and after (fig. 4.8), there was almost no correlation – almost a zero correlation. Furthermore, the single points observed from plots in figs. 4.10 and 4.12, could be considered as outliers, since these may have occurred due to measurement errors.

5. Geophysical resistivity measurements

5.1. Measurements processing

The measured apparent resistivities were uploaded into the EarthImager 3D inversion software from AGI (Advanced Geosciences Incorporated). Erratic data were first of all corrected; these were from measurements taken from the first and fourth transects at 0 and 13.5 m respectively in y-coordinate direction. Electrode 25 on the first transect was mistakenly placed at 71m instead of 72m and electrode 11 on transect four was mistakenly placed at 29.31m instead of 30m. Before any processing was made, the actual positions were modified in the database.

In EarthImager 3D inversion software, settings were adjusted to suit the site parameters, such as setting minimum voltage to 1mV, maximum apparent resistivity to 10,000 ohm-m, setting error reduction to 2.0% and applying a forward modelling inversion. A maximum of three iterations were recorded showing how the data had been smoothed. The results of the inversion are shown in section 5.3.

5.2. Analyzing resistivity data

To analyze the inversion results, it is assumed that in a homogeneous soil media, resistivity calculated using equation 2.1 (with reference to section 2.2.2.1) is constant and independent of both electrode spacing and surface location (Samouëlian et al., 2005). However, with the existence of heterogeneities in the subsurface, there arises a wide range of variation in resistivity with respect to relative positions of the electrodes. The resulting resistivity after calculations is termed as the “apparent” resistivity. This according to Meheni et al. (1996) may allow for a qualitative evaluation of the electrical parameters of the medium; but does not give the true resistivity or shapes of possible anomalies.

Since there is the tendency of misinterpretation of graphical representation, a priori knowledge of the surrounding media is important (Lile et al., 1994); and hence, calculating the “true” resistivity values by inversion programs (RITZ et al., 1999). After conversion from apparent to “true” resistivity from mathematical inversions, quantitative information on resistivity distribution within the subsurface is obtained. The effective depth of investigation as stated above is dependent on the relative positions of both current and potential electrodes. For most earth materials however, electrical resistivity vary widely by several orders of magnitude as shown in table 5.1.

Table 5.1: Resistivity ranges of typical earth materials

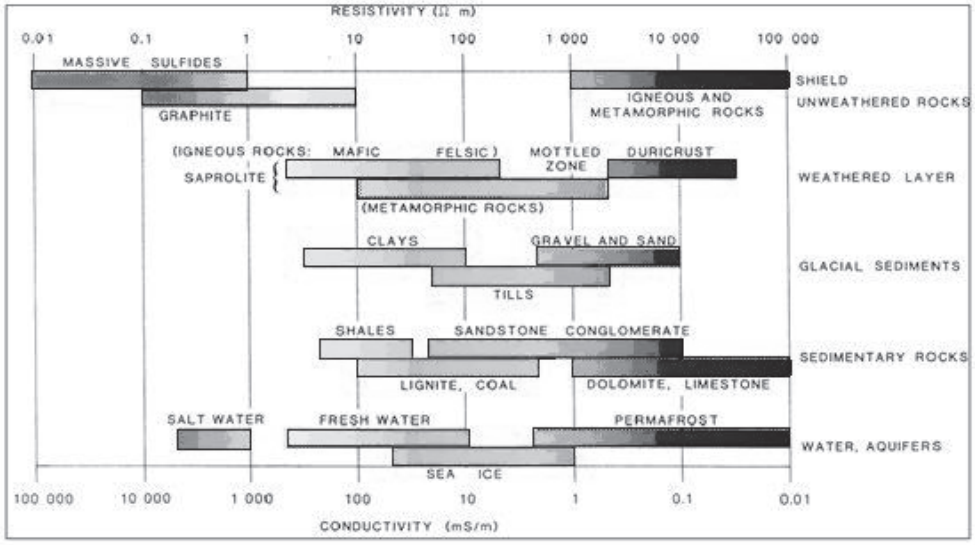

(Cited from Universtiy of British Columbia, Canada GIF website, after(Palacky, 1987))

5.3. Results and discussion from inversion

5.3.1. Results

After the removal of erratic data (about 6.8 %) (fig 5.1) and applying the inversion, an apparent resistivity cross plot yielded an RMS error of 3.2 %, which shows a reduction in data misfit between field measurements and predicted resistivity values of the reconstructed model after a second iteration. An RMS error of 5.1% was however, recorded after the first iteration, and hence reduced to 2.2% after removal of erratic data, which is satisfactory.

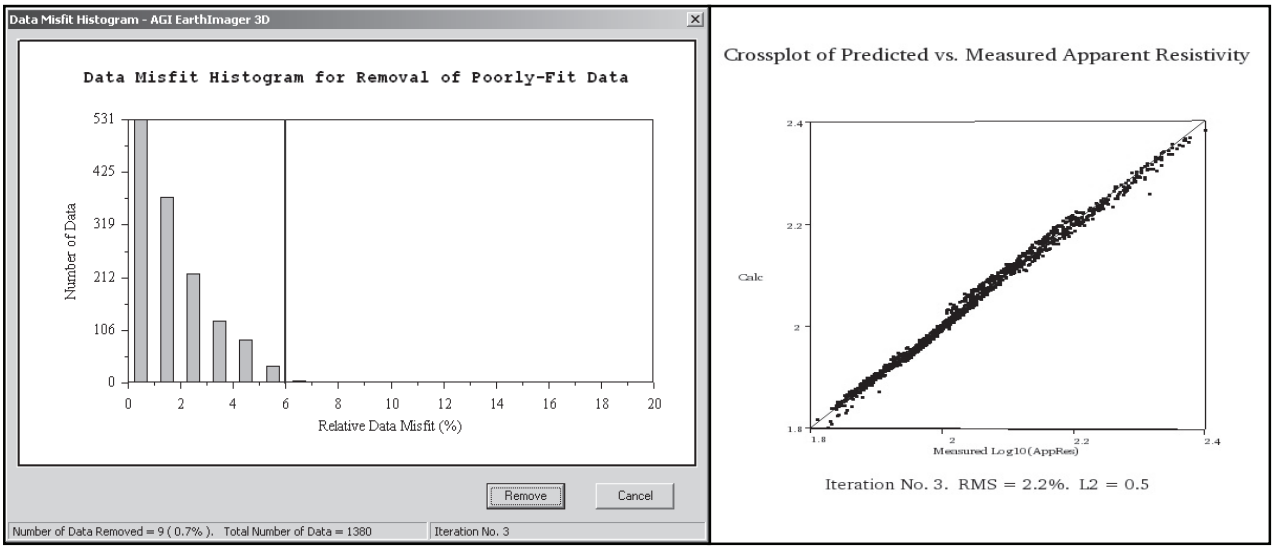

Figure 5.1 Data misfit histogram and apparent resistivity cross plot (between measured and calculated resistivity)

The model result (fig. 5.2) shows depth information up to about 18 meters; with the first few meters having resistivity values up to about 200 Ohm-m. About 6 meters below the surface, there is an even distribution of resistivity of about 130 Ohm-m; however, low resistivity values ranging from about 100 Ohm-m to 48 Ohm-m follows down to the end of the depth information.

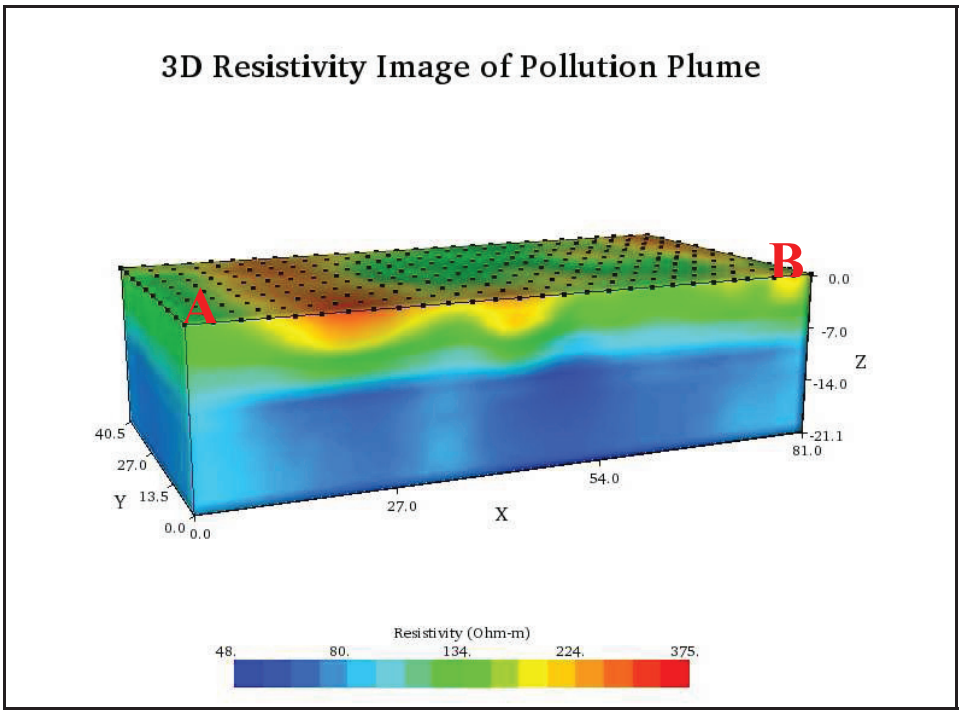

Figure 5.2: Modelled resistivity distribution within the study area

In fig. 5.3, the contour plots indicate zones of resistivity from the surface to below the maximum depth of investigations.

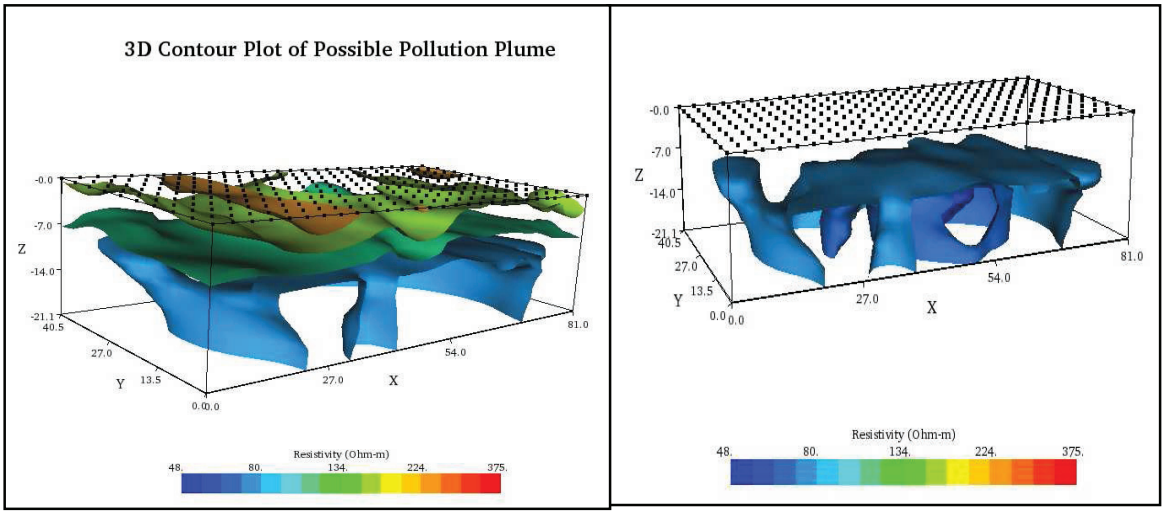

Figure 5.3: Contour plots showing resistive zones, the right picture shows the extent of a possible pollution plume after removal of the high resistivity colours from the left picture

Figure 5.4 shows a slice from A to B (with reference to fig. 5.2) which is also transect3 after the flight for comparisons with vegetation indices later in chapter 7; and fig. 5.5 shows variability of resistivity with different depths from the slice.

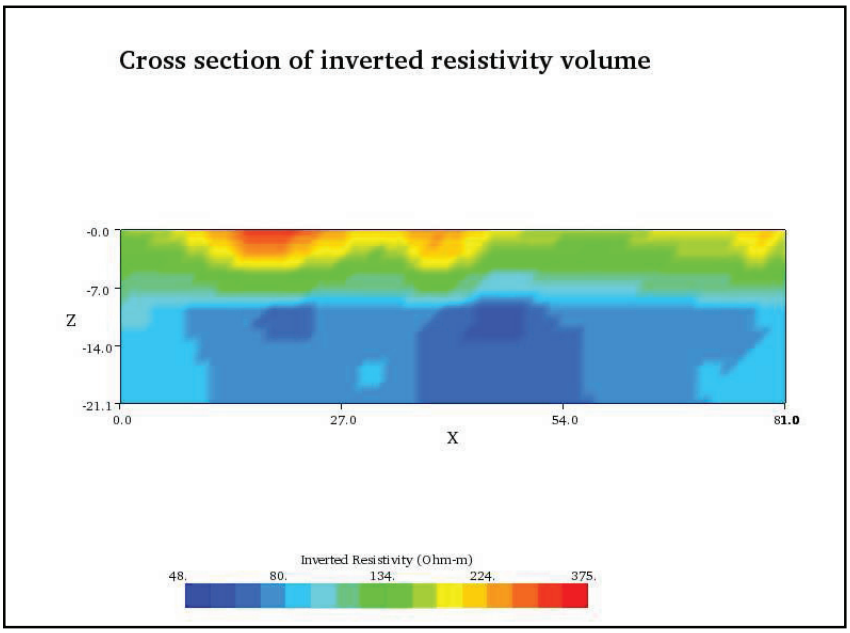

Figure 5.4: A slice from the resistivity inversion which is also transect 3 on vegetation index plot

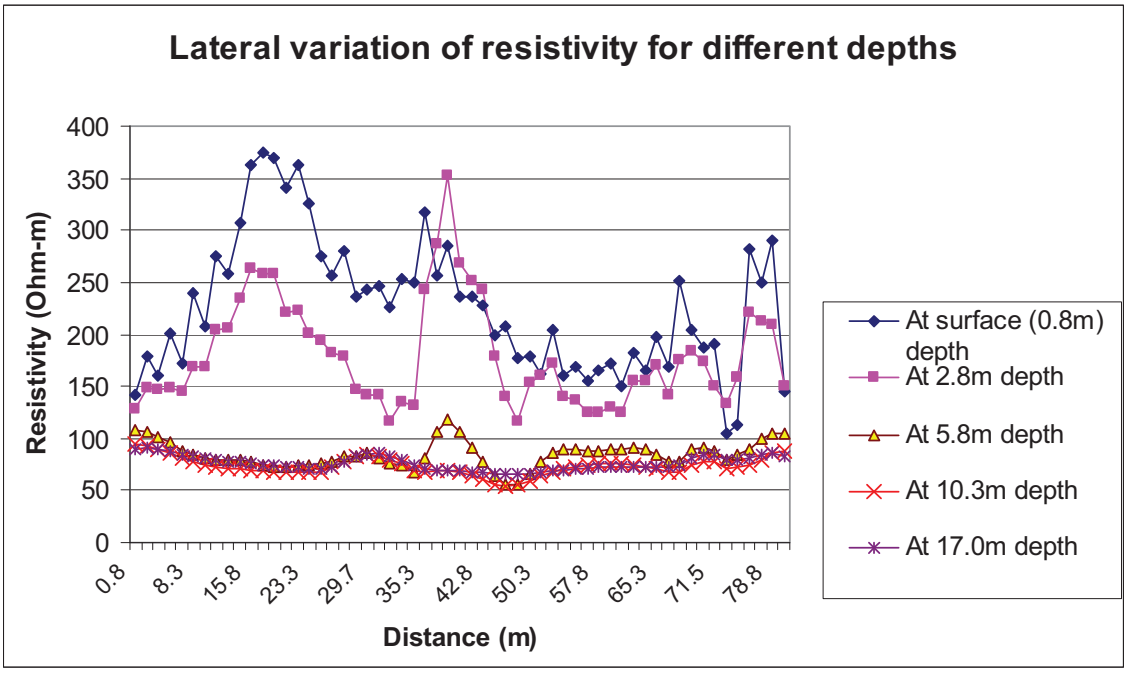

Figure 5.5: A plot of variation of resistivity with depth for the cross-section plot above

5.3.2. Discussion

Usually, hydrocarbons become heavier after undergoing biodegradation (Bailey et al., 1973) and hence, they tend to settle below the groundwater level (Modin et al., 1997). Hydrocarbons are also more easily recognized in sandy-clayish environments rather than purely sandy zones (Shevnin et al., 2003) and hence, with an increase in hydrocarbon-transforming bacteria due to the hydrocarbon pollution, the tendency for groundwater salinity to rise is higher, thereby lowering groundwater resistivity (Atekwana et al., 2001; Sauck, 1998, 2000). Other factors which cannot be overlooked when trying to establish hydrocarbon anomalous zones are the lithology and the position of the groundwater level. In the contaminated zone therefore, high salinity may result and pollutants may move to clayey zones due to bound water by clay minerals; this may cause resistivity contrasts between polluted and non-polluted soils in a highly saline environment to be very minimal, hence posing difficulty in establishing hydrocarbon polluted zones.

Contrasts in resistivity between the polluted site and the surrounding environment could also be dependent on the spillage; where a "matured spill" (e.g. seepage of beyond three months) could produce low resistivity anomalies and the presence of fresh seeps may indicate high anomalous zones. Many low resistive zones due to hydrocarbon spillage, however, have occurred in recent times (Atekwana et al., 2001; Sauck and McNeil, 1994) which may have been caused by intense bacterial action resulting in chemical reactions between organic acids, carbon dioxide and the environment.

The shape of the contours as seen in fig 5.3 above, seem to be homogenous after about 2meters below the ground level and continues up to about 9 meters. This trend, however, starts changing from about 10 meters below the ground level indicating lower zones of resistivity as well as a change in the shape of the contours. Since the environment (study area) is highly sandy with a few clayey zones it is expected to have very high resistivity ranges between approximately 800-10,000 Ohm-m (with reference to table 5.1) as well as, if it is a fresh seep; however, it is possible that, the pollution may have settled in the clayey environment and which is then in agreement with Shevnin and Delgado (2002) as shown by the lower contour values (fig. 5.3). This may be an indication of a high concentration of the pollutant within a boulder of clay**.**

The high resistivity values near to the surface and around 20 and 40 meters in fig. 5.5, along the profile may have been due to the holes in the ground caused by moles (with reference to section 3.2.2) or probably because the soil at those sites is relatively dry and hence creating the high resistivity values; which was explained by Modin et al. (1997) cited in (Shevnin et al., 2003) as probably being due to the inhomogeneities in the subsurface. Furthermore from fig. 5.5, low values of resistivity are observed from below a depth of 10metres ranging between about 50-100 Ohm-m and this may suggest that, the polluted zone may be below this depth.

6. Soil spectra

6.1. Spectra processing procedure

The exported data point table (.dpt) files were accessed in ENVI by building spectral libraries from spectra for each borehole. These were done for spectra acquired for both the mid- and near (shortwave) infrared regions of the EM spectrum. The samples which were considerably very wet were then dried at about 105^{o}C for about 48 hours. The moisture content was then calculated as shown in table 6.1. Spectra were again acquired after finely crushing the hardened dried samples.

Table 6.1: Soil properties (depth, texture, colour and moisture content) within each borehole

Barcode renamed	Depth From / m	Depth To / m	Texture	Munsell colour chart	Moisture content (%)
1997_C	0.0	0.5	Silty fine sand	10YR 2/1 Black	28.99
2017_C	0.5	1.0	Fine clayey sand	5Y 2.5/1 Black	23.82
2000_C	1.0	1.5	Fine Sand	2.5Y 4/3 Olive brown	25.05
2006_C	1.5	2.0	Fine loamy sand	5Y 5/2 Olive gray	25.91
1996_C	2.0	2.5	Very fine loamy sand	5Y 5/2 Olive gray	25.93
2004_C	2.5	3.0	Very fine loamy sand	5Y 6/2 Light olive gray	26.93
2012_C	3.0	3.5	Fine loamy sand	5Y 5/2 Olive gray	26.70
1999_C	3.5	4.0	Very fine loamy sand	5Y 5/2 Olive gray	21.20
1948_C	4.0	4.5	Clayey sand	5Y 7/1 Light gray	26.21
2211_C	4.5	5.0	Very fine sand	2.5Y 5/3 Light olive brown	26.32
2267_C	5.0	5.5	Very fine sand	5Y 5/2 Gray	26.31
2251_C	5.5	6.0	Fine Sand	2.5Y 4/4 Olive brown	27.45
2257_C	6.0	6.5	Fine Sand	5Y 5/4 Olive	27.65
2253_C	6.5	7.0	Fine Sand	2.5Y 4/2 Dark grayish brown	26.98
2265_C	7.0	7.5	Very fine sand	2.5Y 3/3 Dark olive brown	25.73
2262_C	7.5	8.0	Very fine sand	5Y 2.5/2 Black	24.97
2195_U	0.0	0.5	Humic sand	10Y 2/1 Black	22.68
2203_U	0.5	1.0	Fine sand	2.5Y 5/4 Light olive brown	21.57
2104_U	1.0	1.5	Fine sand	5Y 7/3 Pale yellow	21.43
1985_U	1.5	2.0	Fine sand	5Y 5/3 Olive	26.08
1936_U	2.0	2.5	Very fine sand	5Y 6/3 Pale olive	25.68
1984_U	2.5	3.0	Very fine sand	5Y 5/3 Olive	27.07
2204_U	3.0	3.5	Very fine sand	5Y 5/3 Olive	26.42
2213_U	3.5	4.0	Very fine silty sand	5Y 5/3 Olive	25.44
2149_U	4.0	4.5	Very fine silty sand	5Y 5/2 Olive gray	25.47
2206_U	4.5	5.0	Fine sand	5Y 5/3 Olive	23.64
1970_U	5.0	5.5	Fine sand	5Y 5/3 Olive	25.18
1975_U	5.5	6.0	Fine sand	5Y 5/4 Gray	26.83
1929_U	6.0	6.5	Fine sand	5Y 5/2 Olive gray	27.51
1969_U	6.5	7.0	Fine sand	5Y 4/2 Olive gray	27.50
1981_U	7.0	7.5	Fine sand	5Y 5/2 Olive gray	26.09
1956_U	7.5	8.0	Fine sand	5Y 4/3 Olive	27.56

C – refers to almost “clean” borehole sample at the side of the plume i.e. BH-DH9920

U – refers to “unclean” borehole sample at the centre of the plume i.e. BH-ITC

6.2. Visual analysis of spectra by comparison of absorption features

Since almost all the soil samples were considerably wet, spectra which were measured from the wet samples in the MIR were compared with the spectrum of distilled water, from a standard library to observe any differences aside the absorption features found in distilled water. These would then be isolated and used in further analysis of absorption feature parameters. For clarity of each spectrum, the borehole at the centre of the plume (BH-ITC) was divided into four making the comparison of four spectra each with that of distilled water. The first four was from the surface to a depth of 2m of the borehole and the others followed as such as shown in figure 6.1.

The naming of spectra was done by taking the name of the installation which is "vries" and adding the last four digits of the label on each bottle in addition to "wet_MIR" if it is measured as a wet sample and in the MIR wavelength region. If it is a dry sample, and measured in the SWIR region, the phrase "dry_NIR" is added to the installation name and the last four digits as found on the bottle.

For the dry samples, since most of the soil samples had fine sandy texture, spectra measured in the MIR were compared with spectra (sand and quartz) from standard spectral libraries; to observe other absorption features apart from those found in the sand and quartz spectra.

6.2.1. Results from comparison of wet samples absorption features in MIR

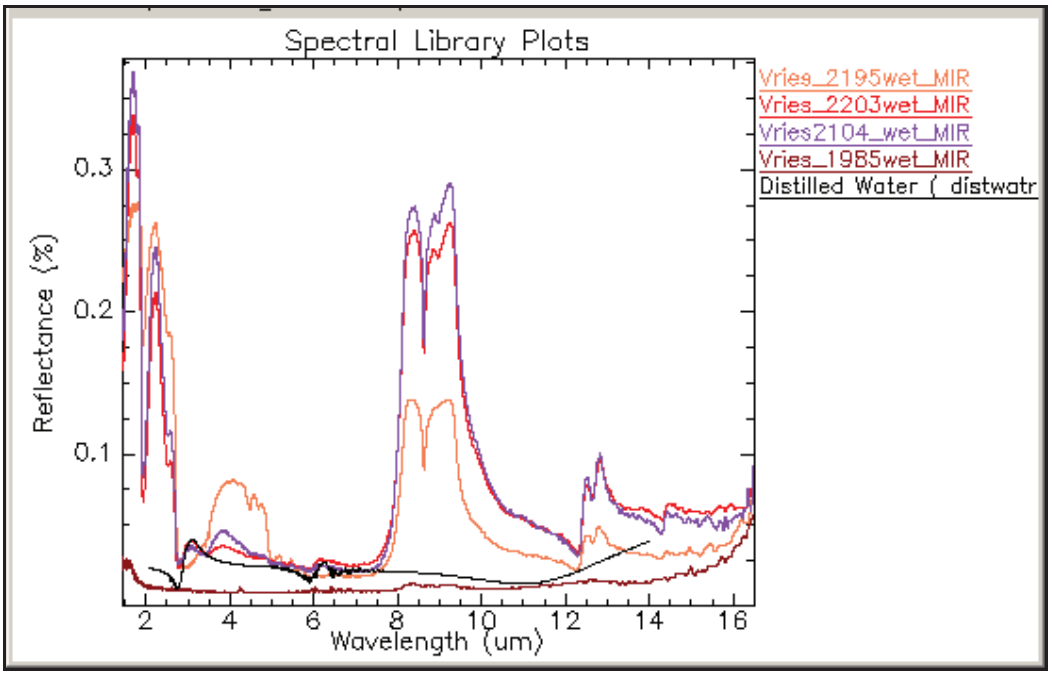

Figure 6.1: Spectra comparison of centre of plume BH samples with that of distilled water from the surface to 2m depth. Note that each spectrum represents 0.5m depth of sample within the borehole

Spectra from the surface up to 2m depth within the borehole showed a bit of similarity with that of distilled water having absorption features at around 2.74µm with one (vries1985_wet_MIR) having a

spectrum similar to that of the open port space. However, the spectrum of vries2195 showed a broader absorption feature from 2.78-3.25µm; as well as small absorptions from 3.38-3.43µm and 3.49-3.51µm. A difference in spectra is also observed in vries2203, which has absorption apart from that of distilled water from 3.13-3.82µm as well as a difference in vries2104 from 3.10-3.76µm. There were also some quartz absorption features evident at 8.6µm in all four spectra.

Spectra from 2 – 4 m depth, however, did not show any significant difference compared to that of distilled water. Absorption features of all four spectra coincided with that of distilled water at 2.78µm. However, quartz absorption features were evident at 8.6µm. This is shown in appendix 2.

In appendix 3, not very significant difference was observed in spectra from 4 - 6 m depth, which was also observed to have similar absorptions with that of distilled water at around 2.76µm, and showed the absorption feature of quartz clearly at around 8.6µm; however, sample vries2149 showed a low reflectance compared to the others and with distilled water, though had the absorption similar to that of distilled water and to quartz.

The last four spectra presented in appendix 4 also showed no significant differences compared with distilled water, except for sample vries1981, which showed a significant absorption feature apart from that of distilled water and quartz evident at 3.20-3.72µm.

For the borehole at the side of the plume (i.e. BH-DH9920), eight spectra from the surface to the midpoint, i.e. to 4m depth, were compared to that of distilled water, since they were wet as well; and this is shown in figure 6.2.

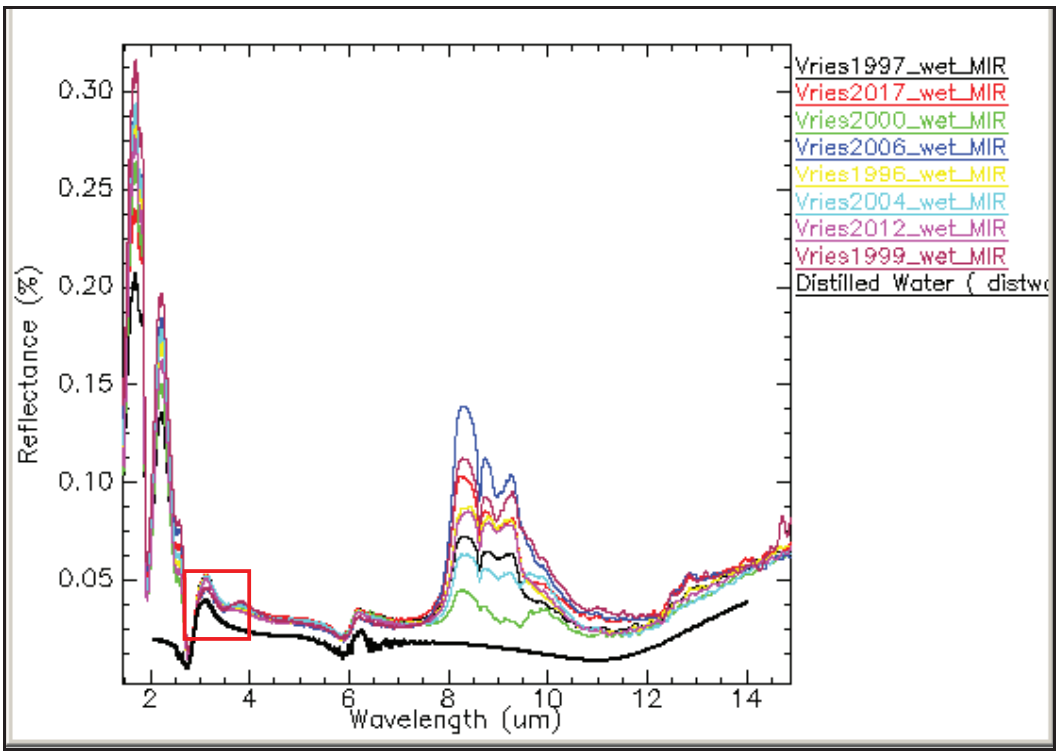

Figure 6.2: Spectra comparison of side of plume BH samples with that of distilled water from the surface to 4m depth. Note that each spectrum represents 0.5m depth of sample within the borehole

From figure 6.2, it is evident that, all spectra measured from the borehole at the side of the plume (BH-DH9920), have similar absorption features at 2.76µm compared to that of distilled water; and the quartz absorption feature is also visible at 8.16µm. However, samples vries2006 and vries1999 (shown in appendix 5 as continuum removed plots) seem to show a slight absorption from 3.14-3.72µm (shown in red box), which is not very significant in all the other spectra, though all the other spectra seem to have very weak absorptions in that range as well.

Appendix 6 presents spectra from the midpoint to the bottom of the borehole, which is from 4-8m depth; two spectra of samples vries2253 and vries2265 showed less reflectance compared to the others and to distilled water, though they seem to have similar but slight absorption at 2.75µm as evident in distilled water.

6.2.2. Results from comparison of wet samples absorption features in SWIR

Spectra measured from borehole samples at the centre of the plume (i.e. BH-ITC) but measured in the SWIR were also compared to that of soil. Soil was chosen because, at the time of measurement, almost all the water had evaporated. The spectrum of "brown to dark brown sand" was chosen from the 'jhu' spectral library, since from table 6.1, all samples are sandy and either brownish or greyish in colour. The spectra representing samples from the borehole was however, divided into two, until the middle, which is 4m depth. Results are as presented in fig. 6.3.

It was observed that, two spectra (vries2203 and vries1936) are different from all others, but which are similar to spectrum of the open port space. All other spectra, however, show similar absorption features to that of the soil which have the strong absorptions of OH bond at 1.4 and 1.9µm respectively. There is also the significant absorption of mica at 2.2µm in all samples with very weak absorptions at 2.31 and 2.34µm on spectrum vries2195. Mica absorption was also evident at the 2.2 µm wavelength position.

The remaining half of spectra comparison with that of soil is found in appendix 7. All spectra show the OH bond absorption feature at 1.4 and 1.9µm with the exception of spectrum vries2149, which is flat and similar to an open port space spectrum. Also, spectra vries1975 and vries1929 show a slight difference in absorption at the 1.4 and 1.9µm wavelength regions. These are shown as very broad absorptions and had low reflectance compared with the others. Spectra from the side of the plume borehole, (i.e. BH-DH9920) however, did not show much difference, with the exception of vries1999 which had a flat spectrum comparable to that from an open port space. These are presented in appendix 8.

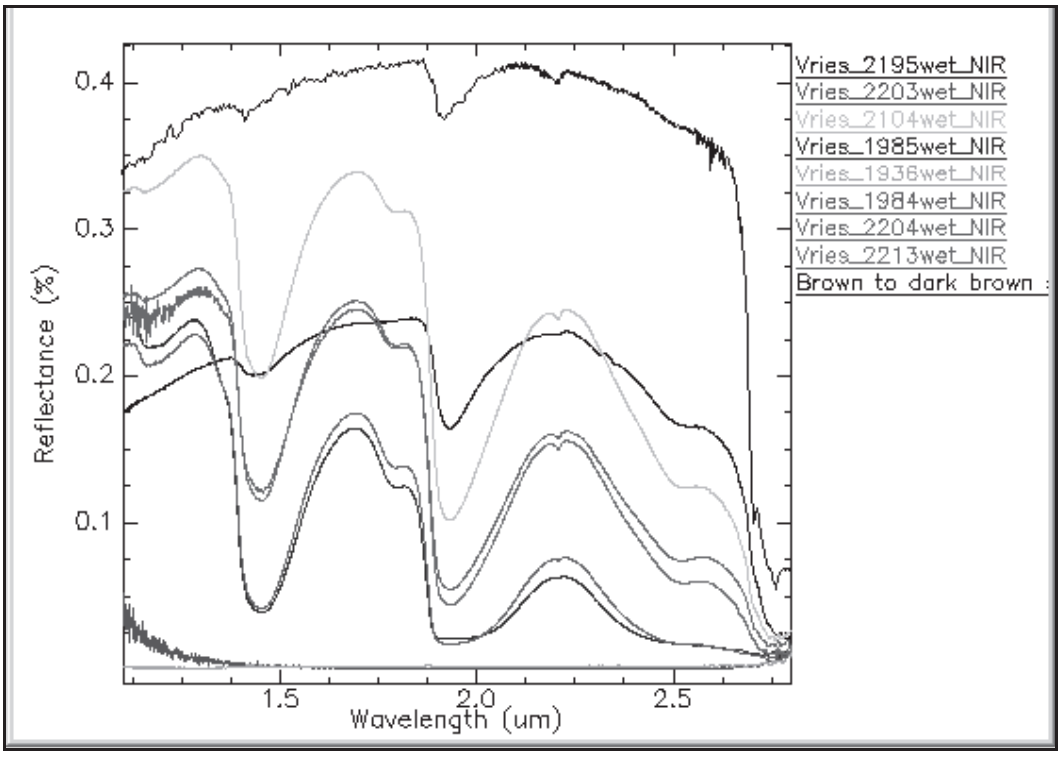

Figure 6.3: Spectra comparison of centre of plume BH samples with that of soil from the surface to 4m depth. Note that each spectrum represents 0.5m depth of sample within the borehole

6.2.3. Results from comparison of dry samples absorption features in MIR

Spectra (from the centre of the plume borehole, i.e. BH-ITC) shown up to a depth of 2m for dry samples and compared to the spectrum of soil have very distinct absorption of the OH feature at 1.9µm and the quartz absorption feature also very distinct at 8.6µm. Spectrum of dry sample vries2203, however, is flat and similar to an open port spectrum. Only dry sample vries2195 however, has other distinct absorption features at 3.41 and 3.50µm respectively; apart from the spectrum of soil. These are represented in appendix 9. From the plot of the last eight spectra within the borehole, spectrum vries1936 showed a similar spectrum to that of an open port space, but all the remaining had a similar feature like that of brown sand, with strong absorptions of the OH bond at 1.9µm and the quartz absorption feature at 8.16µm. All spectra also showed a higher reflectance than the one found from the standard library. These are represented in appendix 10.

All spectra from the borehole at the side of the plume (i.e. BH-DH9920) had similar absorptions at the 1.9µm region showing the OH absorption band, as well as the quartz absorption at 8.6µm just like the spectrum from the standard spectral library. However, three spectra, i.e. vries2006, vries2004 and vries2012 have flat spectra which can be likened to that from the open port space. Three other spectra (vries1997, vries2000 and vries2017) also show some very distinct features at 3.41 and 3.50µm; however, it cannot be said to be the absorption feature for hydrocarbons. Further analysis will be made to determine the absorption feature parameters for these. These are shown in appendix 11.

6.2.4. Results from comparison of dry samples absorption features in SWIR

Five spectra (vries2104, vries1984, vries2204, vries2206 and vries1929) from the borehole at the centre of the plume (BH-ITC) and measured in the SWIR show flat signatures but which are comparable to the open port space spectrum. The remaining eleven spectra though, show distinct absorptions of the OH bond at 1.4 and 1.9µm respectively with the exception of sample vries2195 which shows a very weak absorption at the 1.4µm wavelength. All eleven spectra also have strong absorption of mica at 2.2µm with the exception of vries2195 which has a relatively very weak absorption at that wavelength. Spectrum vries2195 also shows a unique absorption starting from 2.42-2.59µm, which is not characterized by the others. These are shown in appendix 12.

For spectra from the borehole at the side of the plume (BH-DH9920) however, all spectra (with the exception of vries2265) showed characteristic absorption of the OH bond at 1.4 and 1.9µm respectively as well as the 2.2µm absorption feature of mica. The spectrum of vries2265, however, had similarity with the spectrum of the open port space spectrum. The fifteen spectra also showed higher reflectance compared to that from the standard library. Spectra vries1997 and vries2017,

however, had unique absorptions from 2.30 - 2.34µm, but they also show broad features from 2.44 – 2.56µm. These will however be investigated further, but are represented in appendix 13.

A further comparison of absorption features in the MIR for spectra from both boreholes (i.e. BH-ITC and BH-DH9920) is presented in appendix 14, to show differences in absorptions.

6.3. Discussion from visual inspection of spectra by comparison of absorption features

From section 6.2.1, wet samples spectra from the borehole at the centre of the plume (i.e. BH-ITC) showed similar absorptions at around 3.3µm to 3.45µm; which is also the approximate wavelength position of hydrocarbons in the MIR from previous studies (Brown, 2007; Duley et al., 2005; Stuart, 2004) as expected. All the spectra from wet samples from the borehole at the side of the plume (BH-DH9920) with weak absorptions, as well as the distinct absorptions observed in vries2006 and vries1999, were however, not expected to have absorptions at the expected wavelength position, i.e. around 3.4 µm. It is however, possible that, since the hydrocarbons are liquid or gaseous substances, they may have migrated to this "supposedly clean" site; which is the borehole at the side of the plume and hence observed in those spectra.

The observation made from measurement in the SWIR (with reference to section 6.2.2) from wet spectrum vries2195 (BH-ITC) with weak absorptions around 2.31 and 2.34µm could be said to be that from hydrocarbons as mentioned by Brown (2007) which is expected, or probably that of calcite CO_3^2 owing to an alteration of the soil due to hydrocarbon effect as explained by van der Meer et al.(2000).

For the dry sample measurements from the borehole at the centre of the plume (BH-ITC) in the MIR, which showed a higher reflectance (with reference to section 6.2.3) than the one found from the standard library, it may have been due to the evaporation of moisture as well as the grain size as discussed by van der Meer (2004). The distinct features at 3.41 and 3.50µm of three spectra (vries1997, vries2000 and vries2017) are also characteristic of hydrocarbons in the MIR and in agreement with the findings of Stuart (2004). These, however, cannot be said to be the absorption feature for hydrocarbons since the samples had been dried and expected to have evaporated if there was indeed any pollution. Further analysis will however be done to determine the absorption feature parameters for these; for verification under section 6.4.

Dry sample spectrum vries2195 measured from the borehole in the centre of the plume (i.e. BH-ITC) in the SWIR which showed absorption between 2.42 -2.59µm (with reference to section 6.2.4) could be likened to the absorption of carbonate (CO_3^{2-}) ion which is an alteration product of hydrocarbon

effect on soils (van der Meer et al., 2000); since the hydrocarbons are expected to have evaporated after drying.

6.4. Quantification of pollution by analysis of absorption feature parameters

Numerous studies suggest that, a change in the absorption band position, shape, depth and width of a material, is largely dependent on the composition of the material (Cloutis, 1996; van der Meer, 2004). With most soil materials exhibiting fundamental vibrations in the MIR with some exhibiting broader and weaker combinations and overtones in the shortwave infrared part of the spectrum (Brown, 2007); as for e.g. seen in C-H stretches, which has absorptions at 3.4µm in the MIR and shows some overtones at 1.7 and 1.15µm in the NIR, it will be possible to analyze the hydrocarbon absorptions both in the mid and near infrared range of the spectrum. Based on the above therefore, the differences in spectra observed from section 6.2 and with a combination of table 6.2 are used for further analysis of HC absorptions in the spectra.

Table 6.2: Mid and near – infrared absorptions of some hydrocarbons

Hydrocarbon group	Wavelength range	Literature
CH_2 and CH_3	3.3 - 3.4 µm	(Brown, 2007; Duley et al., 2005; Joblin et al., 1995; Stuart, 2004)
Crude oil and methane	1.18, 1.38 µm, narrow, sharply defined, though fairly weak absorption	(Xu et al., 2008)
Crude oil and methane	1.68-1.72; 2.3-2.45 µm; broader but much stronger absorption	(Brown, 2007; Xu et al., 2008)

The depth of absorption is known to be an indicator of how much of a material causes the absorption in a sample. The band depth also has a relation to the grain size of a material, since the amount of light scattered or absorbed by a grain is largely related to the grain size (van der Meer, 2004). The composition therefore, and hence the quantity of HC if present in the soil samples, can be determined by the absorption band depth of the spectra measured from the soil samples.

The "DISPEC" tool embedded in ENVI was used for this analysis. With the differences observed from the wet soil samples in relation to the standard library distilled water, as well as the differences in the dry samples relatively to the standard library sand; spectra were resized at the particular wavelengths and analyzed by the absorption parameters, i.e. depth, position, width, etc., as shown in appendix 15.

6.4.1. Results from absorption feature analysis of wet spectra in SWIR

From the analysis using DISPEC, the spectrum vries2195 from the borehole at the center of the plume (BH-ITC) shows absorption wavelength position of 2.313μm and an absorption band depth of 0.01, and all others had relatively no absorption features in that wavelength. For spectra from the borehole at the side of the plume (BH-DH9920) however, no distinctive absorption feature was observed at the expected wavelength positions (with reference to table 6.2).

6.4.2. Results from absorption feature analysis of wet spectra in MIR

A plot of values obtained from analysis of samples from the MIR of the borehole at the side of the plume (i.e. BH-DH9920) is presented in figure 6.4.

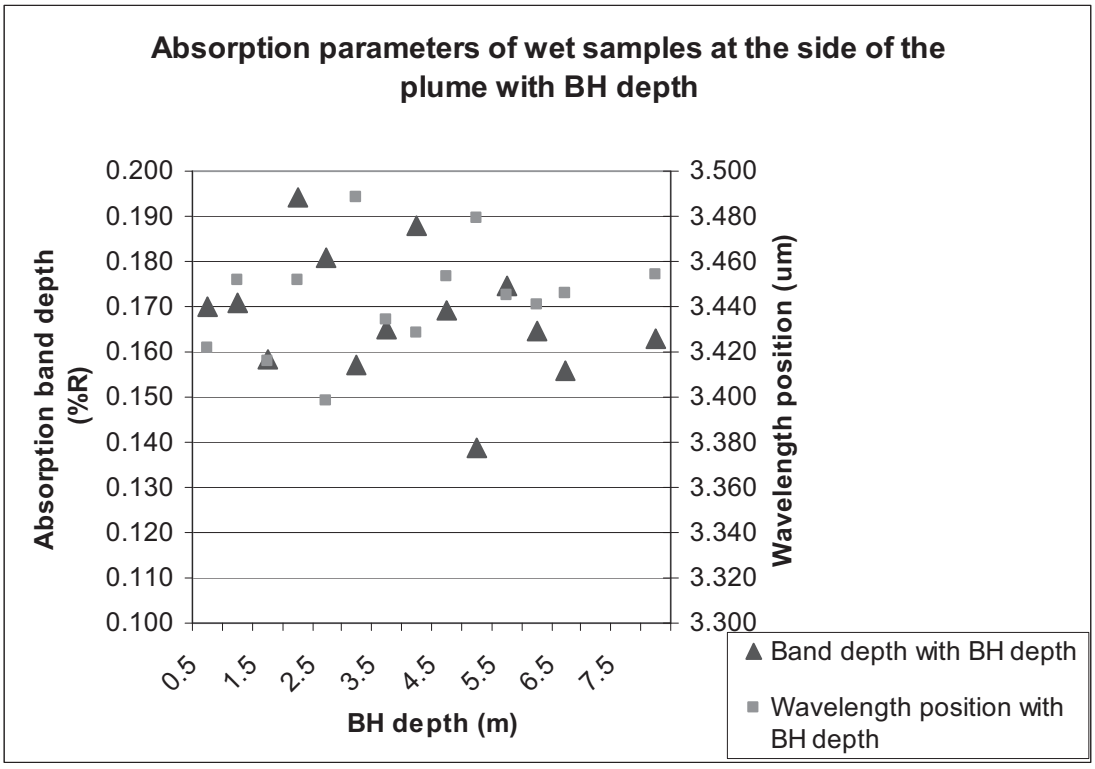

Figure 6.4: Absorption feature parameter plot with borehole depth at the side of the plume in MIR

It is clear from fig. 6.4 that, at a depth of 2 and 4 meter depth respectively, absorption band depths are 0.194 and 0.188 respectively and together with all others (fig. 6.4 and table 6.3), does not show any consistency. Values of wavelength positions ranged from about 3.41 – 3.48μm. It should however be noted that, not all samples had absorption features as explained under section 6.2.1. Appendices 16 and 17 show wet, as well as dry and MIR absorption feature parameters of samples in boreholes at the centre and side of the plume respectively.

Table 6.3: Wet and MIR absorption feature parameters of samples at the side of the plume borehole

Sample number	Wavelength position	Absorption band depth	Width	Area	Asymmetry	BH-depth
Vries1997_wet_MIR	3.422	0.170	0.41672	0.06012	-0.33680	0.5
Vries2017_wet_MIR	3.452	0.171	0.40096	0.06248	-0.05030	1.0
Vries2000_wet_MIR	3.416	0.158	0.39308	0.06048	-0.43510	1.5
Vries2006_wet_MIR	3.452	0.194	0.35685	0.06898	-0.06070	2.0
Vries1996_wet_MIR	3.398	0.181	0.41356	0.06955	-0.52740	2.5
Vries2004_wet_MIR	3.488	0.157	0.37418	0.05601	0.17190	3.0
Vries2012_wet_MIR	3.434	0.165	0.38048	0.06020	-0.28760	3.5
Vries1999_wet_MIR	3.428	0.188	0.35528	0.06537	-0.26700	4.0
Vries1948_wet_MIR	3.454	0.169	0.38678	0.05874	-0.16120	4.5
Vries2211_wet_MIR	3.480	0.139	0.38678	0.05105	0.03775	5.0
Vries2267_wet_MIR	3.445	0.175	0.36866	0.06435	-0.20940	5.5
Vries2251_wet_MIR	3.441	0.164	0.38835	0.05842	-0.26340	6.0
Vries2257_wet_MIR	3.446	0.156	0.37969	0.05469	-0.19040	6.5
Vries2253_wet_MIR	0.000	0.000	0.00000	0.00000	0.00000	0.0
Vries2265_wet_MIR	0.000	0.000	0.00000	0.00000	0.00000	0.0
Vries2262_wet_MIR	3.454	0.163	0.35685	0.05658	-0.04090	8.0

For the borehole at the centre of the plume (i.e.BH-ITC) though, not all spectra showed absorption (with reference to section 6.2.1) and, that which showed absorption are plotted as shown in figure 6.5.

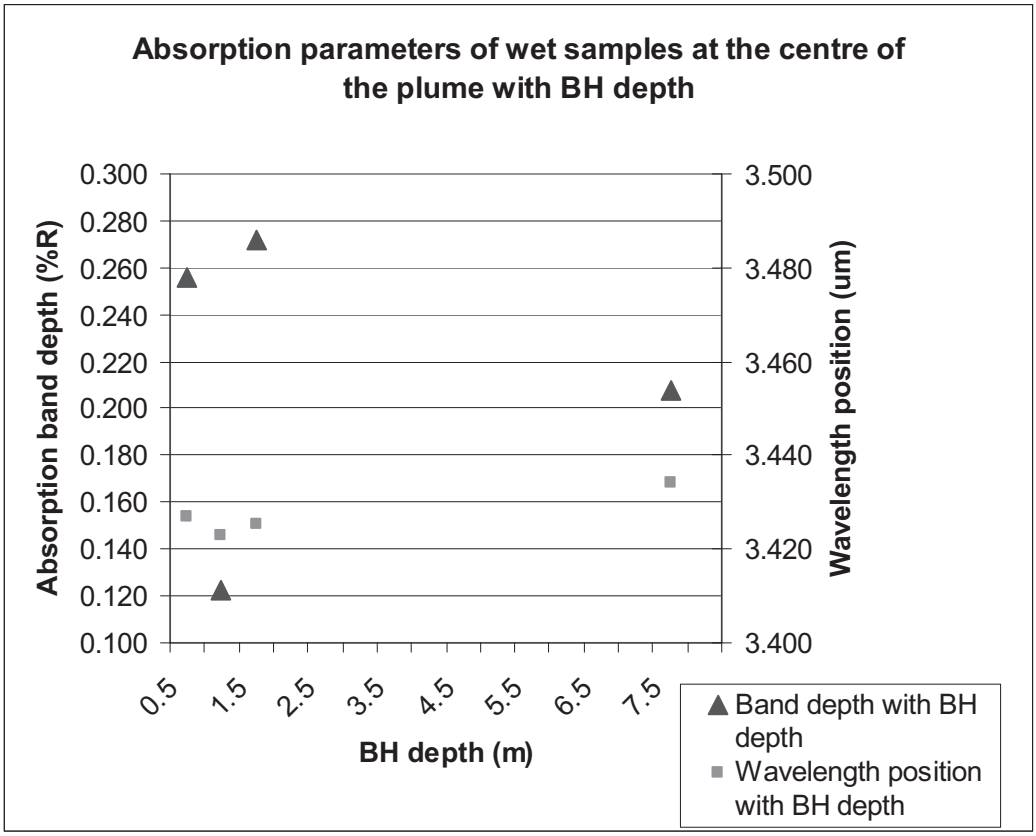

Figure 6.5: Absorption feature parameter plot with borehole depth at the centre of the plume in MIR

Values depicted from figure 6.5 suggest that absorption band depth does not follow a consistent range as was expected. Spectrum at a borehole depth of 7.5m has an absorption band depth of about 0.208 whereas spectrum at a depth of 1.5 meters has an absorption band depth of about 0.272. The spectra, however, showed absorptions around the 3.4µm wavelength range.

6.4.3. Results from absorption feature analysis of dry spectra in MIR

Spectra analysis of dry samples at the centre of the plume borehole (i.e. BH-ITC) measured in the MIR did not show much absorption with the exception of sample vries2195 (at a borehole depth of 0.5) which showed absorption at a wavelength position of 3.42µm and at an absorption band depth of 0.33. Sample vries2104 (at a borehole depth of 1.5) also showed a very weak absorption at the 3.41 µm wavelength at a band depth of 0.032. Other spectra within the borehole however, did not show any significant absorption.

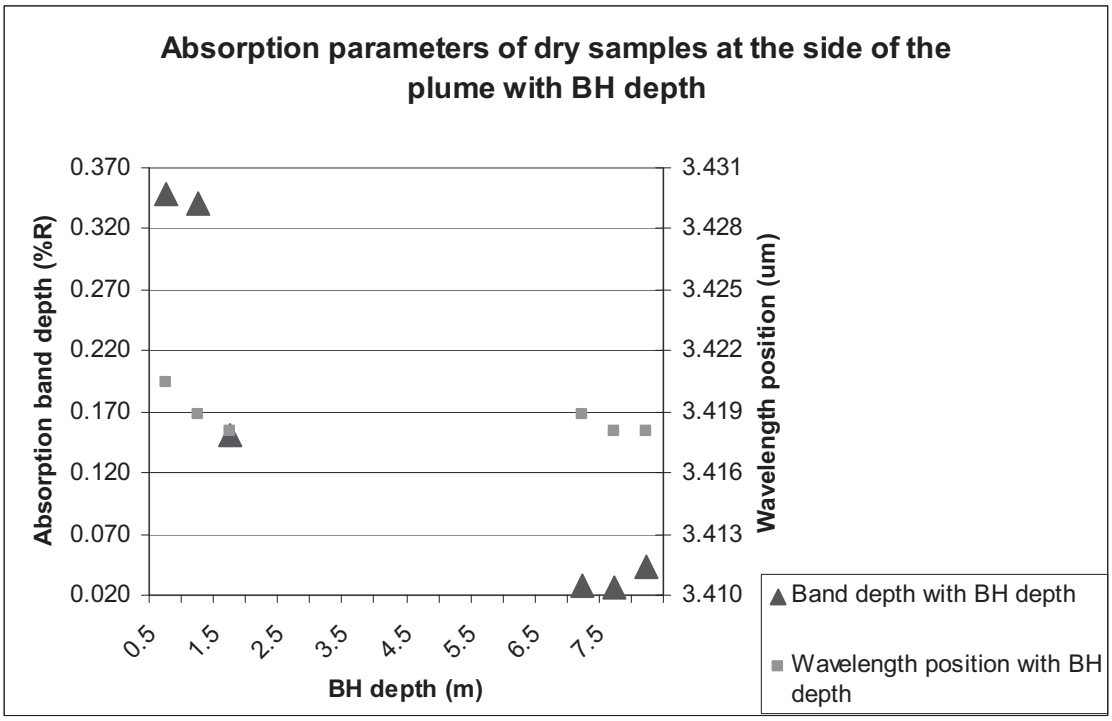

Figure 6.6: Absorption feature parameter plot with borehole depth at the side of the plume in MIR

The analysis of dry spectra in the MIR from the borehole at the side of the plume (BH-DH9920) yielded the results in fig. 6.6. Not all spectra showed absorptions at the expected wavelength, (i.e. around 3.4 µm), except for a few. For example, samples vries1997 at 0.5m depth had absorption band depth at 0.349 and vries2017 at 1m depth showed absorption with a band depth of 0.341. The rest showed very weak absorption band depths from 0.026 to 0.152; this is presented in appendix 17.

6.4.4. Results from absorption feature analysis of dry spectra in SWIR

Analysis of spectra from dry samples measured in the SWIR from samples from the centre of the plume borehole (i.e. BH-ITC) showed one distinct absorption feature from sample vires2195 found at 0.5m depth in the borehole. The absorption feature was however very weak and found at a wavelength position of 2.309µm and a weak band depth of 0.019. All other spectra did not show significant absorption at this wavelength.

The analysis of dry spectra from the borehole at the side of the plume showed that sample vries1997 at depth 0.5m had a weak absorption at 2.306µm and an absorption band depth of 0.011. All other spectra did not show any significant absorption at the expected wavelength.

6.5. Discussion of absorption feature parameter analysis

The results from wet sample vries2195 and at a depth of 0.5m within the borehole at the centre of the plume (i.e. BH-ITC, with reference to section 6.4.1), and measured in the SWIR showed a wavelength position of 2.313µm which is expected as for e.g. found by Xu et al.(2007); however, with a very low absorption band depth of 0.01, it is not conclusive whether the absorption is from hydrocarbons or not and if it is from hydrocarbons, its "quantity" can be said to be negligible.

For the plot from figure 6.4 (from wet measurements in MIR for the borehole at the side of the plume), it is expected that if the pollution is from the surface and migrating into the subsurface towards the ground water, then the absorption band depth (quantity) would increase with depth, i.e., being more concentrated in the subsurface than on the surface. This is however, not the case in this area since spectrum from the surface (vries1997) and which represents a depth of 0.5m shows an absorption band depth of 0.170 and is at a wavelength position of 3.422µm; and the spectrum of vries2262 at a depth of 8m had an absorption band depth of 0.163 and a position of 3.454µm. Together with the absorption band depths at 0.194 and 0.188 at depths of 2 and 4 meter respectively, (table 6.3); suggests that, the consistency in band depth is not as expected, i.e., from low to high values if the pollution is indeed migrating towards the subsurface. Values of the wavelength positions, which range from about 3.41 – 3.48µm, can be said to be acceptable and as expected, as found from previous studies (Brown, 2007; Duley et al., 2005; Stuart, 2004). However, the borehole from which these values were obtained is at the side of the plume and expected to be clean (i.e. BH-DH9920); but from the findings, it can be considered as contaminated; hence for an accurate conclusion, the values can be compared with levels of pollutant concentration from a chemical analysis from drill data by the NAM oil company. For spectra (from the centre of the plume borehole, i.e. BH-ITC), which showed absorptions around the 3.4µm range suggests that the range of absorption wavelength position (3.41-3.43µm) is as expected; and the absorption band depth values seem higher (i.e. ranging between

0.123-0.272) than that obtained from the borehole at the side of the plume (i.e. ranging between 0.139-0.194). The quantities of HC if present can therefore be said to be higher from samples in the centre of the plume borehole than at the side of the plume. Also according to Stuart (2004), the existence of hydrogen bonding in a compound may introduce some other information into spectra and hence leading to a false interpretation. Hence it cannot be concluded with high certainty that, the absorptions found at the specific wavelengths are from hydrocarbons.

For the wet samples measured in the MIR from both boreholes and which were found to have absorptions at the expected wavelengths (i.e. between 3.3-3.5μm), it was expected that, there would be corresponding absorption features in the SWIR from the same wet samples, but in this case, only sample vries2195 from the centre of the plume borehole had an absorption as stated in section 6.4.4. However, the absorption band depth (0.01) of this sample could be said to be negligible and therefore, it cannot be concluded with certainty that, the absorptions found in the MIR were those of HCs.

The few dry spectra measured in the MIR which showed approximate absorptions at the expected wavelength (from the borehole at the side of the plume) did not show consistency in absorption band depth values, although the values were high for the first 1m within the borehole (i.e. 0.349 and 0.341 for 0.5m and 1m respectively). These spectra though, were not expected to show hydrocarbon absorptions at the expected wavelength and with such high absorption band depth values; since they are located in the borehole at the side of the plume and are as well dried. With the drying therefore, it is expected that, hydrocarbons would have evaporated if they were present.

Results from dry spectrum vries2195 which showed absorption at around 2.3 to 2.4μm in the measurement of dry samples in the SWIR as well as that found in vries1997, could be that of calcite. If there was indeed pollution from hydrocarbon, the spectrum may have been an alteration product of the effect of the hydrocarbon as discussed by van der Meer et al. (2000). Since not all spectra were observed to be consistent in absorption features of hydrocarbons within both boreholes, it suggests that, probably, the HC's may have settled in, or have been absorbed by the few clayey boulders found in the area; because during the first phase of contamination, they can be concentrated in the sandy environment, but will migrate with time and be absorbed by clays as described by Shevnin et al. (2003).

Generally from the findings if there is HC present, it can be concluded that, the borehole at the side of the plume (i.e., BH-DH9920) is more polluted than the borehole at the centre (i.e. BH-ITC); though band depth values (quantities) obtained from BH-ITC seem to be higher, more spectra from BH-DH9920 showed absorption depths suggesting more pollution.

7. Integration of results

The results from chapters 4 to 6 are integrated to estimate the level and quantity of pollution. From fig. 7.1, transects from vegetation measurements intersect with that from geophysical measurements (at transect A-B, which is also 'transect 3' after the flight, with reference to chapter 4) and hence, the results from both analyses are integrated to establish a correlation. The borehole analyses by spectra information are also correlated with that from vegetation and geophysics by visual and statistical analysis respectively.

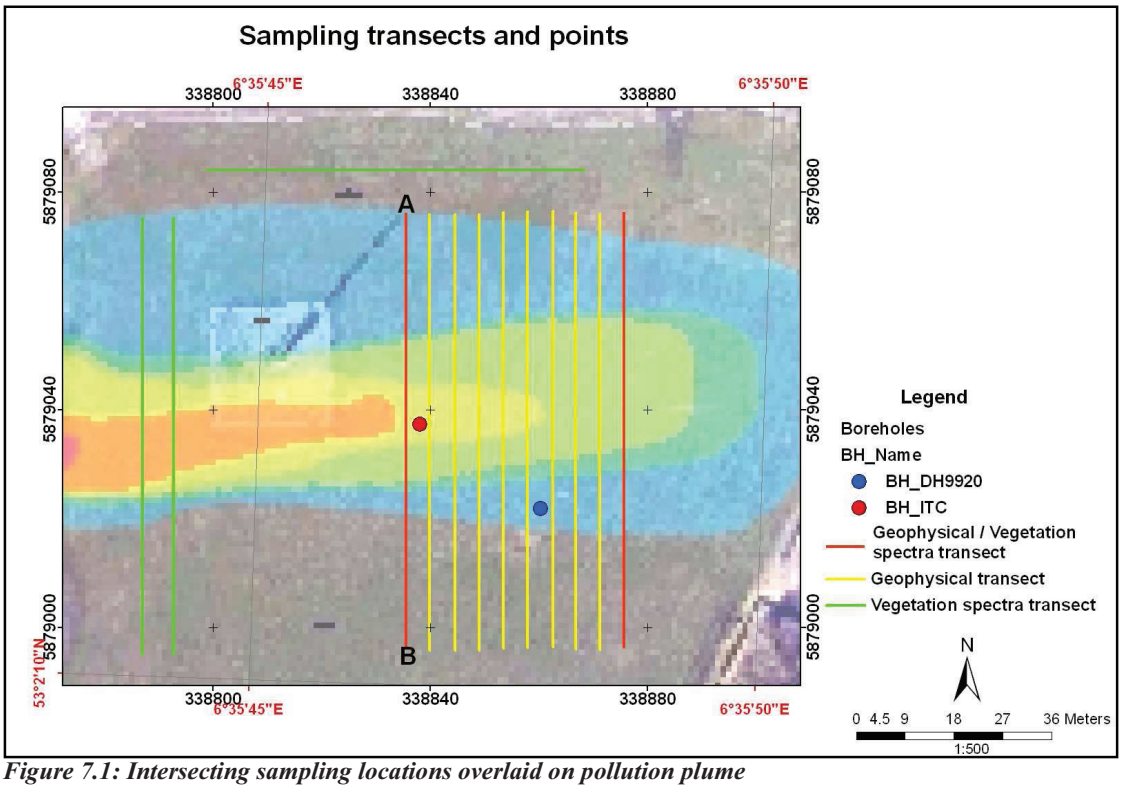

Figure 7.1: Intersecting sampling locations overlaid on pollution plume

7.1. Integration of vegetation and resistivity analyses results

A plot of vegetation red-edge position values from transect A – B (transect 3 after flight) is plotted with extracted results from the first profile of resistivity measurements (since they intersect with each other as observed in fig. 7.1) to establish correlations. The values are presented in appendix18. The surface values of bulk resistivity (with reference to figure 5.5) were chosen since it is that, which is likely to affect the vegetation. The lateral variation plot is presented in figure 7.2.

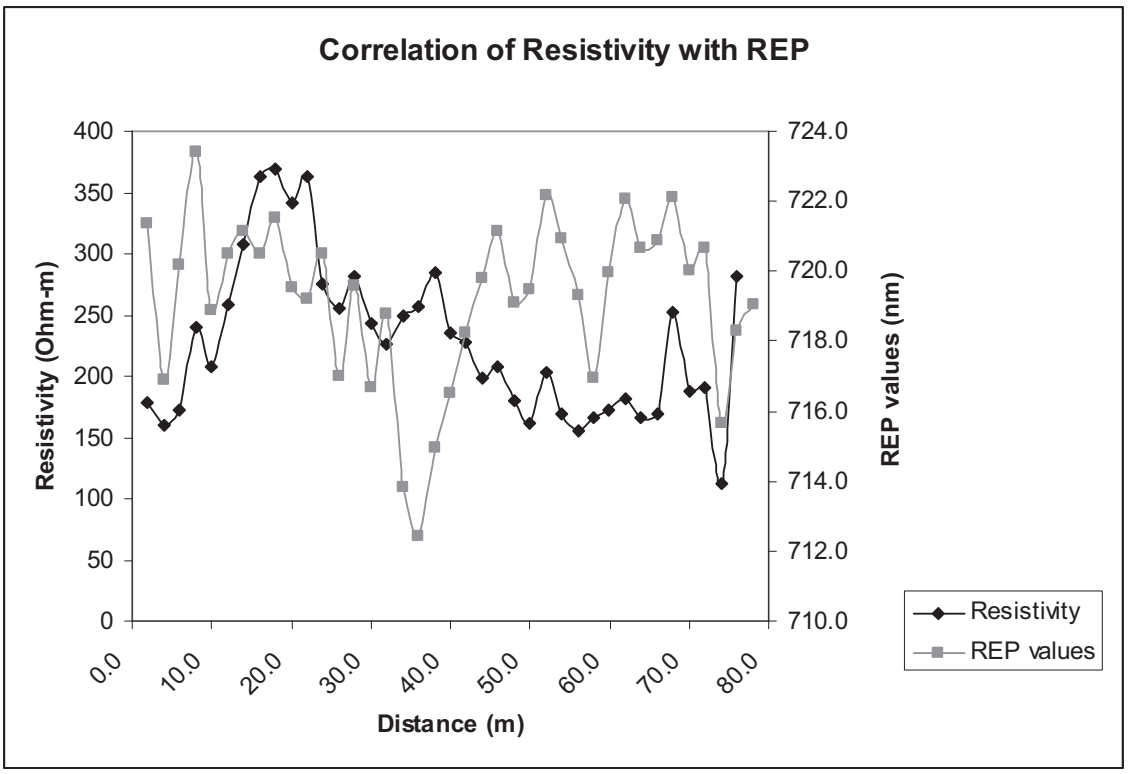

Figure 7.2: Combined analysis of bulk resistivity and vegetation red edge values for transect A - B

Figure 7.2 shows a combined analysis of bulk geophysical resistivity on the surface and vegetation red edge position values with a correlation coefficient of R^2 0.01. For red edge position values shifting towards shorter wavelengths (which indicate vegetation stress), resistivity values in the surface indicate relatively lower values (though these values are high with respect to the range of values of resistivity with depth); except for a few points and especially at a distance of about 36m that a REP value produces a corresponding high value of resistivity. If the HC is migrating towards the subsurface, it is clear from the resistivity plot for different depths (with reference to fig. 5.5) that, it is concentrated at a depth from about 10meters below the surface. However, it is not very clear if the effect on vegetation red edge values shifting towards shorter wavelengths was caused by the HC pollution. Since grass is the type of vegetation from which spectroscopic measurements were conducted and grass roots are known to have very shallow depths (Schwinning et al., 2005) and with the detection of the pollution over three years ago, it is possible that, its effect on the grass may have been minimal. In addition to the homogeneous layers observed in the resistivity model, it is possible that, if HC is present, it may not have migrated beyond the layers towards the surface (if it is in the subsurface), to affect the vegetation.

7.2. Integration of resistivity and HC quantification results from soil spectra

From the plot of absorption band depth values with borehole depth, there was no consistency in band depth values (quantified pollution) being indicative of pollution migrating with depth. With the band depth values obtained (with reference to fig. 6.5), it was observed from the borehole at the centre of the plume (i.e. BH-ITC) that, higher values were obtained though not consistent with depth; and from the side of the plume borehole (i.e. BH-DH9920), there were some "quantified" pollution i.e. from absorption band depth values which were not, however expected, since it was distant away from the plume.

From the geophysical inversion model (with reference to fig. 5.2 and 5.3) low resistivity zones which were observed from a depth of about 10 meters below the surface are indicative as anomalous zones, which is in agreement with studies undertaken by Palacky (1987) and could possibly be pollution zones. Absorption band depth values from the centre of the plume borehole (i.e. BH-ITC) were correlated with resistivity values extracted at location 42m on the geophysical transect (presented in appendix 19); which resulted in a correlation coefficient of 0.55. However, the two drilled boreholes were both to a depth of 8meters, and the anomalous zones observed from the resistivity model are from 10meters and below; it is therefore possible that, the higher concentration of HC pollution if present, is from 10meters and below; hence not very evident from the soil parameters and hence, the less correlation.

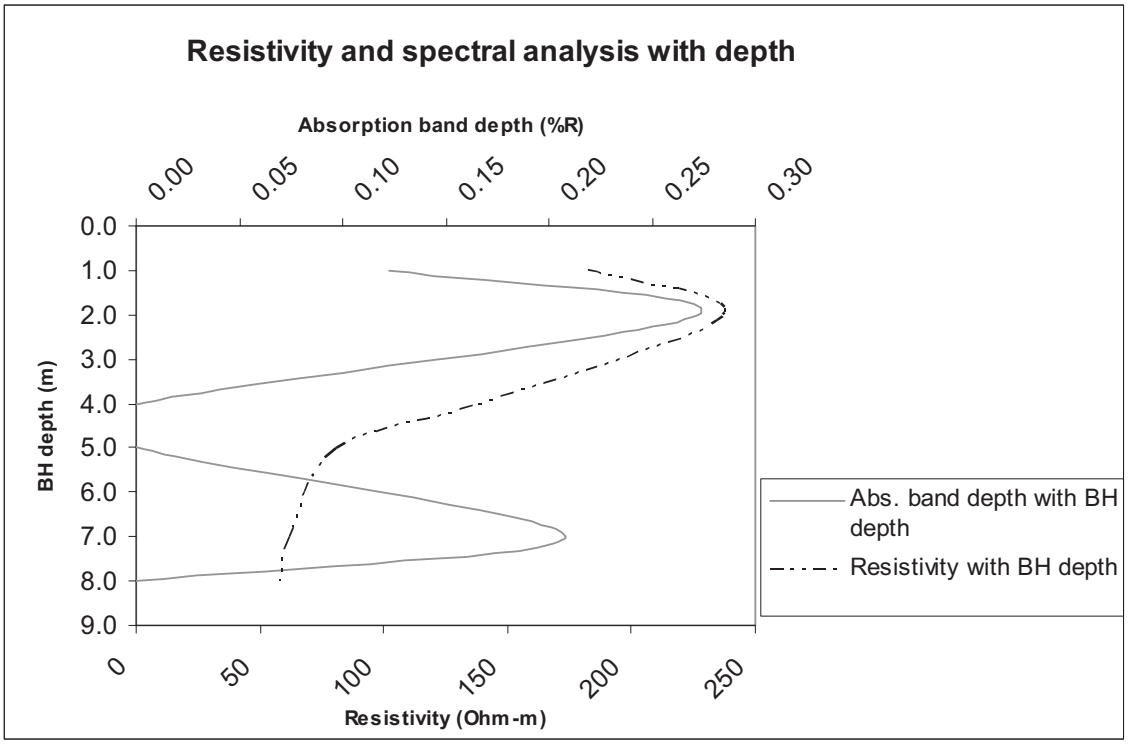

Figure 7.3: Variation of resistivity and spectral analysis with depth, for borehole at centre of plume

However, with the limited number of absorption band depth values obtained from samples from the centre of the plume borehole, it cannot be concluded with high certainty if the absorptions are from HCs.

7.3. Integration of soil parameters and vegetation indices results

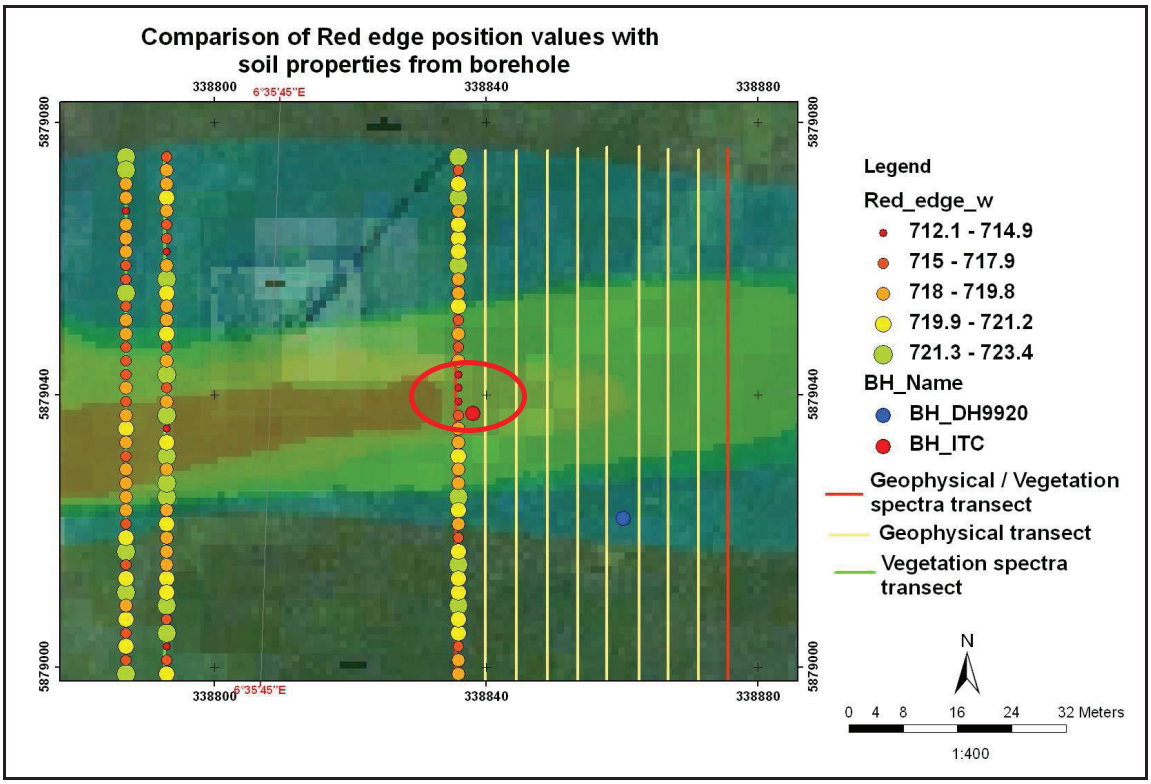

Figure 7.4: Combined analysis of vegetation red edge values with borehole at the centre of the plume. Affected vegetation and borehole bound in red-circle

Vegetation red-edge position values shifting to shorter wavelengths are considered as anomalous or stressed (Li et al., 2005). From fig. 7.3, the centre of the plume borehole (i.e. BH-ITC) is seen to have been drilled very close to the transect (bound in red circle); from which follows a similar pattern of all vegetation indices (i.e. REP, NDVI and OSAVI bound in red circles from figures 4.1- 4.3) indicating stress in vegetation. Since the spectra from the surface (which represented 0.5m depth from the borehole) was found to have an absorption band depth of 0.256 (in appendix16), showing the "quantity" of pollution at the particular location; and since grass is considered to have a shallow depth, it can be said that, this area may be polluted having a relatively higher band depth value and REP values shifting towards shorter wavelengths; being an indication of a geobotanical anomaly of hydrocarbon pollution effect on vegetation being in agreement with findings from Yang et al. (1998).

7.4. Validation of analysis results with chemical analysis data from NAM

Chemical analysis from drill data, suggests that several samples within the side of the plume borehole (BH-DH9920) contained different levels of the contaminant as shown in appendix 20. Appendix 21 however showed that, only one sample and at a depth of 5.0m within the centre of the plume borehole (BH-ITC) had been contaminated. Out of the hydrocarbon product BTEX, benzene was observed to be the main contaminant having concentrations of between 0.1 to 1.5 mg/kg. A plot of benzene quantities were plotted with absorption band depth values (which also represents the "quantity" or composition of a material (van der Meer, 2004)) from wet sample measurements in the MIR; to identify the variation of both chemical and spectral analysis with borehole depth. This was used as a form of validation to complement results from the analysis of spectra.

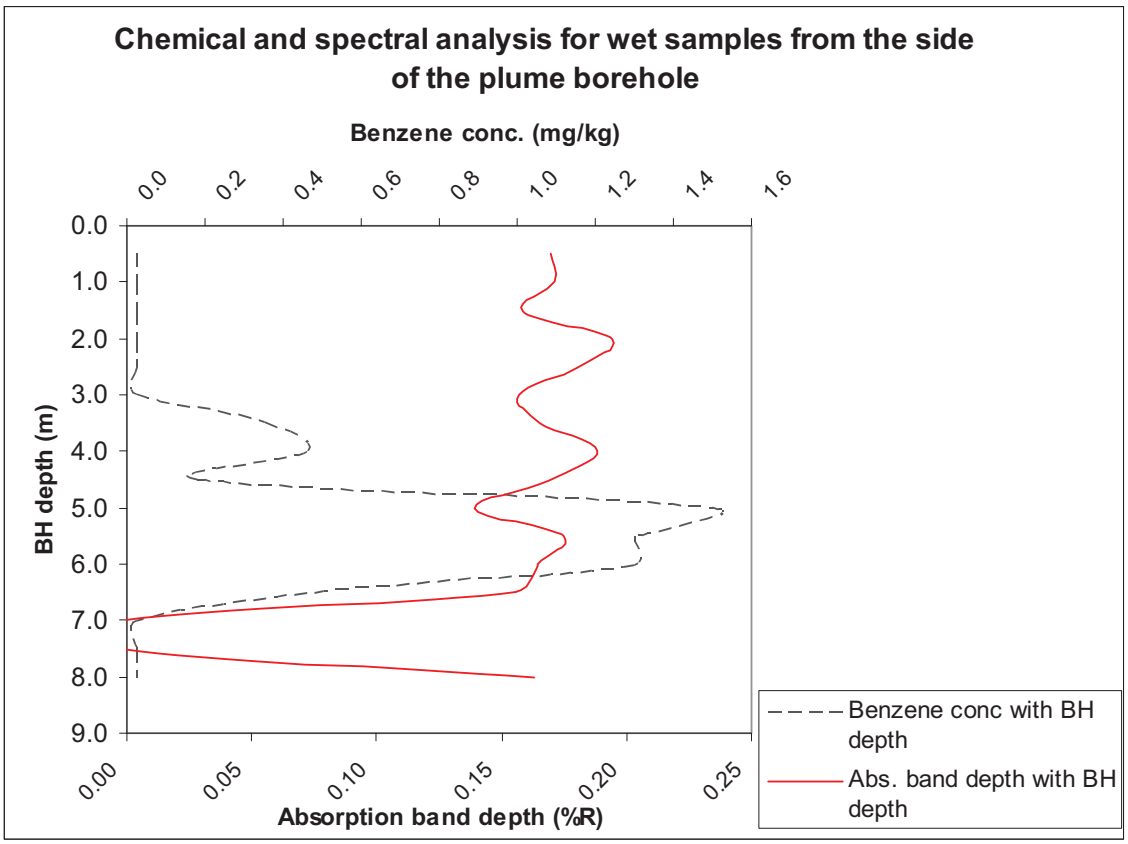

Figure 7.5: Correlation of chemical and spectral analysis variation within the borehole at the side of the plume for wet and MIR measurements

The detection limit of the chemical analysis suggests that below 0.05 (i.e. <0.05) mg/kg, the concentrations are acceptable. Due to this, it was assumed that, all concentrations below 0.05mg/kg were taken as 0.025mg/kg and used in the plot of concentration variation with depth. The combined analysis of the wet spectra absorption band depth and the benzene concentrations yielded a correlation coefficient of 0.16 (fig. 7.5). The correlation was performed for only the side of plume borehole (i.e. BH-DH9920), since it was that which had most benzene quantities as well as absorption band depths (quantities) observed; and therefore considered as most polluted.

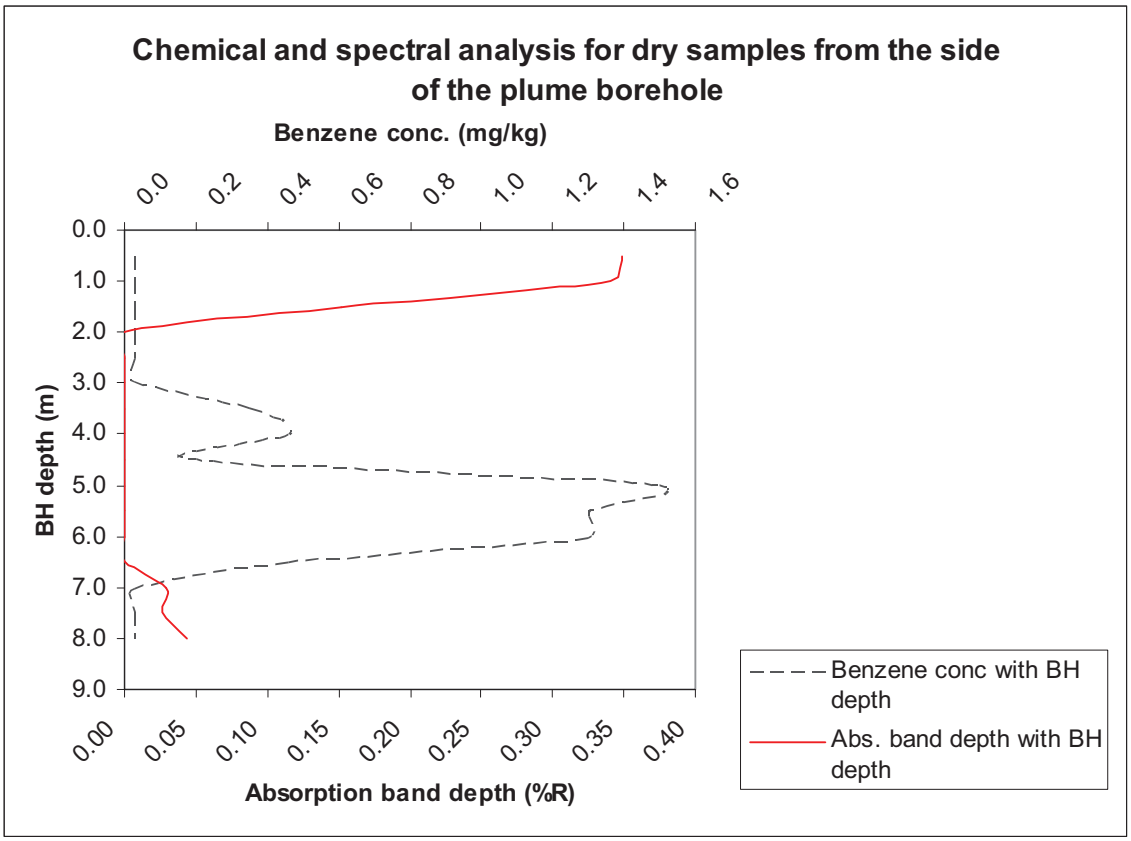

Figure 7.6: Correlation of chemical and spectral analysis variation within the borehole at the side of the plume for dry and MIR measurements

Since information from the Oil Company did not state clearly whether the benzene quantities were from the original wet samples or they were obtained after the drying of the samples, the same chemical analysis values were correlated with dry spectra absorption depth values obtained and this resulted in a correlation coefficient of 0.34, presented in fig. 7.6. However, since not all the spectra which had absorption band depths when measured as wet samples retained their absorption depths after dry measurements, it is not with high certainty as to whether the band depths obtained after dry measurements is that of HCs or not.

From appendix 18, not all the spectra which were observed to have absorption band depth values had benzene concentrations recorded from the analysis. Assuming then that, the analytical data is good and with high accuracy in measurement procedures; the findings from spectra in absorption band depths ("quantities"), and which did not have a corresponding chemical analytical data may be said not to have been from HCs but from something else.

8. Conclusions and Recommendations

8.1. Conclusions

The main objective of this study was to quantify and map the extent and level of HC pollution, in soil in the Assen area using the combination of field spectrometry, hyperspectral image and geophysical surveys (resistivity surveys); and in response to the specific objectives and research questions, we draw the following conclusions:

1. Will there be a gradient in absorption features of soils taken at different depths (3D) indicating less to highly polluted surfaces, and can these be quantified?

From the results and discussions on soil spectra, it is evident that there is no consistency in absorption features and specifically, absorption band depth values within the soil core. It was expected that, if the pollutants were migrating with depth, then more concentrations of the pollutants, will be within deeper depths and hence show higher absorption band depth values. This is however, not the case in this situation. However, the borehole which was at the side of the plume (i.e. BH-DH9920) and distant away from the centre of the plume borehole (i.e. BH-ITC) was found to have more absorption band depths as well as more benzene quantities. This could therefore suggest that, the pollutant may have moved laterally with the groundwater and not vertically downwards or towards the surface. Though the absorption band depths have been used in "quantifying" the HC composition of the soil, and with an assumption that the chemical analysis was accurately carried out; it is not with high certainty, however, whether the pollutants are from hydrocarbons or from some other soil constituent.

2. How can the geophysical measurements be related to spectra of soils taken at different depths?

From the correlation plot of resistivity with soil spectral analysis, it is evident that values of resistivity variation with depth can be extracted and related with spectral parameters calculated for different depths within a borehole; though with less correlation in this case.

3. Can vegetation spectra be used as an intermediate source of information to link the surface to the subsurface using the HyMap Image?

Analysis from vegetation spectra has been able to show which individual measured points are stressed (with the assumption that stress is a measure of the health status of the vegetation) and the comparisons with the HyMap image suggests that, there is almost no significant differences in value ranges if the image is taken at the same time of field measurements. However, if the findings were able to establish with certainty (which was not the case in this situation) whether the stress in vegetation was from the pollution of hydrocarbons; then surface information from vegetation spectra, (from the HyMap image) can be used to link the subsurface.

4. Will there be differences when expected results drawn from field spectrometry measurements are compared to the hyperspectral image of the contaminated site?

Findings from comparisons of field and image values of vegetation indices indicate that, no significant differences were observed between field and image values for all indices applied (i.e. REP, NDVI, OSAVI); for field values measured at the same time of acquisition of image.

8.2. Recommendations

With the borehole depth analysis not being able to establish with certainty whether the findings are really from hydrocarbons or not, it is recommended that different soil components and their properties are taken into consideration; during the detection of hydrocarbons using hyperspectral remote sensing, since hydrocarbon contamination of soils may be a mixture of other constituents such as soil moisture, soil, salts and hydrocarbons. In addition, since most of the absorptions observed in the MIR were around 3.4µm, with no corresponding SWIR absorption bands, it is possible that, the absorptions in the MIR may be due to other soil constituents; and therefore recommended that further studies would explore for hydrocarbon bands in the SWIR. A further study into hydrocarbon induced plant stress is also recommended since it is not with high certainty whether the stress is from lack of chlorophyll concentration or from hydrocarbons.

The geophysical technique was able to delineate anomalous zones which may be potential pollutant zones and so, it is recommended that drill data will correspond exactly with data (with regards to depth information) extracted from geophysical information for a proper correlation. It is again recommended that, to integrate results from three different techniques, measurements should be taken approximately at the same time, with less time lapse to establish accurate correlations.

References

Abdel-Kader, A. F., S. M. Nasr, H. I. El-Gamily, and M. El-Raey, 1998, Environmental sensitivity analysis of potential oil spill for Ras-Mohammed coastal zone, Egypt: Journal of Coastal Research, v. 14, p. 502-511.

AGI, 2007, Resisitivity Data Processing with Eathimager 1D, 2D & 3D, Advanced Geosciences, Inc., Austin, Texas.

Almeida, R., 2002, Remote detection of hydrocarbon microseepage areas in the Serra do Tona region, Tucano basin, Brazil: Canadian Journal of Remote Sensing, v. 28, p. 750-757.

ASD, 2008, NIR Solutions for the Real World Product Specifications — FieldSpec® 3 Analytical Spectral Devices Inc.

Asner, G. P., 1998, Biophysical and Biochemical Sources of Variability in Canopy Reflectance: Remote Sensing of Environment, v. 64, p. 234-253.

Atekwana, E., D. P. Cassidy, C. Magnuson, A. L. Endres, D. D. Werkema JR., and W. A. Sauck, 2001, Changes in geoelectrical properties accompanying microbial degradation of LNAPL: In: Proceedings of the Symposium on the Application of Geophysics to Engineering and Environmental Problems, p. 1–10.

Atekwana, E. A., E. Atekwana, F. D. Legall, and R. V. Krishnamurthy, 2004a, Field evidence for geophysical detection of subsurface zones of enhanced microbial activity: Geophysical Research Letters, v. 31.

Atekwana, E. A., W. A. Sauck, and D. D. Werkema, 2000, Investigations of geoelectrical signatures at a hydrocarbon contaminated site: Journal of Applied Geophysics, v. 44, p. 167-180.

Atekwana, E. A., D. D. Werkema, J. W. Duris, S. Rossbach, W. A. Sauck, D. P. Cassidy, J. Means, and F. D. Legall, 2004b, In-situ apparent conductivity measurements and microbial population distribution at a hydrocarbon-contaminated site: Geophysics, v. 69, p. 56-63.

Bailey, N. J. L., C. R. E. Krouse, and M. A. Rogers, 1973, Alteration of Crude Oil by Waters and Bacteria - Evidence from Geochemical and Isotope Studies, American Association of Petroleum Geologists Bulletin.

Bammel, B. H., and R. W. Birnie, 1994, SPECTRAL REFLECTANCE RESPONSE OF BIG SAGEBRUSH TO HYDROCARBON-INDUCED STRESS IN THE BIGHORN BASIN, WYOMING: Photogrammetric Engineering and Remote Sensing, v. 60, p. 87-96.

Baret, F., S. Jacquemoud, G. Guyot, and C. Leprieur, 1992, MODELED ANALYSIS OF THE BIOPHYSICAL NATURE OF SPECTRAL SHIFTS AND COMPARISON WITH INFORMATION-CONTENT OF BROAD BANDS: Remote Sensing of Environment, v. 41, p. 133-142.

Batkhuyag, O., 2008, Spectral indicators for assessing the effect of hydrocarbon leakage on vegetation, ITC, Enschede, 79 p.

Benson, A. K., and J. Wu, 1999, A modeling solution for predicting (a) dry rock bulk modulus, rigidity modulus and (b) seismic velocities and reflection coefficients in porous, fluid-filled

rocks with applications to laboratory rock samples and well logs: Journal of Applied Geophysics, v. 41, p. 49-73.

Boegh, E., H. Soegaard, N. Broge, C. B. Hasager, N. O. Jensen, K. Schelde, and A. Thomsen, 2002, Airborne multispectral data for quantifying leaf area index, nitrogen concentration, and photosynthetic efficiency in agriculture: Remote Sensing of Environment, v. 81, p. 179-193.

Boru, G., T. Vantoai, J. Alves, D. Hua, and M. Knee, 2003, Responses of soybean to oxygen deficiency and elevated root-zone carbon dioxide concentration: Annals of Botany, v. 91, p. 447-453.

Brown, D. J., 2007, Using a global VNIR soil-spectral library for local soil characterization and landscape modeling in a 2nd-order Uganda watershed: Geoderma, v. 140, p. 444-453.

Cann, P. M., and H. A. Spikes, 2005, In-Contact IR Spectroscopy of Hydrocarbon Lubricants: Tribology Letters, v. 19, p. 289-297.

Cho, M. A., and A. K. Skidmore, 2006, A new technique for extracting the red edge position from hyperspectral data: The linear extrapolation method: Remote Sensing of Environment, v. 101, p. 181-193.

Cloutis, E. A., 1989, Spectral Reflectance Properties of Hydrocarbons: Remote-Sensing Implications: Science, v. 245, p. 165-168.

Cloutis, E. A., 1996, Spectral Properties of Hydrocarbon-bearing Geological Materials: Lunar and Planetary Science, v. 27, p. 237.

Cundill, L. S., 2008, Investigation of soil reflectances for detecting hydrocarbon pipeline leakages, ITC, Enschede, 67 p.

Dahlin, T., and C. Bernstone, 1997, A roll-along technique for 3D resistivity data acquisition with multi-electrode arrays, SAGEEP'97, Lund, Sweden, Lund University, p. 927-935.

Dawson, T. P., and P. J. Curran, 1998, A new technique for interpolating the reflectance red edge position: International Journal of Remote Sensing v. 19, p. 2133-2139

Duley, W. W., V. I. Grishko, J. Kenel, G. Lee-Dadswell, and A. Scott, 2005, Laboratory and theoretical simulation of 3.4 mu m spectra of hydrocarbons in interstellar sources: Astrophysical Journal, v. 626, p. 933-939.

Etiope, G., and R. W. Klusman, 2002, Geologic emissions of methane to the atmosphere: Chemosphere, v. 49, p. 777-789.

Fabio Fava, S. B. P. C. A. P. L. M., 2004, Effects of humic substances and soya lecithin on the aerobic bioremediation of a soil historically contaminated by polycyclic aromatic hydrocarbons (PAHs): Biotechnology and Bioengineering, v. 88, p. 214-223.

Fomenko, V. M., O. A. Shushakov, and V. S. Kuskovskii, 2008, Detection of groundwater contamination with hydrocarbons: Russian Geology and Geophysics, v. 49, p. 183-186.

Fuchs, H. V., and R. Riehle, 1991, 10 YEARS OF EXPERIENCE WITH LEAK DETECTION BY ACOUSTIC-SIGNAL ANALYSIS: Applied Acoustics, v. 33, p. 1-19.

Geiger, G., 2006, State-of-the-art in leak detection and localization: Oil Gas-European Magazine, v. 32, p. 193-198.

Giao, P. H., S. G. Chung, D. Y. Kim, and H. Tanaka, 2003, Electric imaging and laboratory resistivity testing for geotechnical investigation of Pusan clay deposits: Journal of Applied Geophysics, v. 52, p. 157-175.

Goetz, A. F. H., 1992, IMAGING SPECTROMETRY FOR EARTH OBSERVATIONS: Episodes, v. 15, p. 7-14.

Grandjean, G., 2006, A seismic multi-approach method for characterizing contaminated sites: Journal of Applied Geophysics, v. 58, p. 87-98.

Green, A. A., and M. D. Graig, 1985, Analysis of aircraft spectrometer data with logarithmic residuals. In: Vane, G., Goetz, A.F.H. (Eds.), Proceedings of the Airborne Imaging Spectrometer Data Analysis Workshop, p. 111-119.

Grégoire, C., P. K. Joesten, and J. J. W. Lane, 2006, Use of borehole radar reflection logging to monitor steam-enhanced remediation in fractured limestone--results of numerical modelling and a field experiment: Journal of Applied Geophysics, v. 60, p. 41-54.

Guyot, G., and F. Baret, 1988, Utilisation de la haute resolution spectrale pour suivre l'etat des couverts vegetaux, *Proceedings of the 4th International Colloquim on Spectral Signatures of Objects in Remote Sensing ESA* v. SP-287 p. 279–286.

Hao, T. Y., Z. H. Zhu, M. H. Zhang, X. X. Huang, H. B. Song, and W. W. Jiang, 2001, Alteration zone from the marine oil-gas seepage and its geophysical detection methods: Chinese Journal of Geophysics-Chinese Edition, v. 44, p. 245-+.

Heiden, U., K. Segl, S. Roessner, and H. Kaufmann, 2007, Determination of robust spectral features for identification of urban surface materials in hyperspectral remote sensing data: Remote Sensing of Environment, v. 111, p. 537-552.

Horig, B., F. Kuhn, F. Oschutz, and F. Lehmann, 2001, HyMap hyperspectral remote sensing to detect hydrocarbons: International Journal of Remote Sensing, v. 22, p. 1413-1422.

Howari, F. M., 2004, Investigation of hydrocarbon pollution in the vicinity of United Arab Emirates coasts using visible and near infrared remote sensing data: Journal of Coastal Research, v. 20, p. 1089-1095.

Huete, A. R., 1988, A soil-adjusted vegetation index (SAVI): Remote Sensing of Environment, v. 25, p. 295-309.

Hwang, Y. K., A. L. Endres, S. D. Piggott, and B. L. Parker, 2008, Long-term ground penetrating radar monitoring of a small volume DNAPL release in a natural groundwater flow field: Journal of Contaminant Hydrology, v. 97, p. 1-12.

Jarlan, L., S. Mangiarotti, E. Mougin, P. Mazzega, P. Hiernaux, and V. Le Dantec, 2008, Assimilation of SPOT/VEGETATION NDVI data into a sahelian vegetation dynamics model: Remote Sensing of Environment, v. 112, p. 1381-1394.

Jones, J. W., 1996, Preliminary Spatially Distributed Estimates of Evapotranspiration Using In-situ and Satellite Remote Sensing Data, South Florida Information Access.

King, T. V. V., and R. N. Clark, 1989, Reflectance Spectroscopy (0.2 to 20 microns) as an Analytical Method for the Detection of Organics *In: Soils: Proceedings First International Symposium: Field Screening Methods for Harzadous Waste Site Investigations*, EPA, p. 485-488.

Kuhn, F., K. Oppermann, and B. Horig, 2004, Hydrocarbon Index - an algorithm for hyperspectral detection of hydrocarbons: International Journal of Remote Sensing, v. 25, p. 2467-2473.

Leyval, C., and P. Binet, 1998, Effect of Polyaromatic Hydrocarbons in Soil on Arbuscular Mycorrhizal Plants: J Environ Qual, v. 27, p. 402-407.

Li, L., S. L. Ustin, and M. Lay, 2005, Application of AVIRIS data in detection of oil-induced vegetation stress and cover change at Jornada, New Mexico: Remote Sensing of Environment, v. 94, p. 1-16.

Lile, O. B., K. R. Backe, H. Elvebakk, and J. E. Buan, 1994, Resistivity measurements on the sea bottom to map fracture zones in the bedrock underneath sediments¹: Geophysical Prospecting, v. 42, p. 813-824.

Luyendyk, B., J. Kennett, and J. F. Clark, 2005, Hypothesis for increased atmospheric methane input from hydrocarbon seeps on exposed continental shelves during glacial low sea level: Marine and Petroleum Geology, v. 22, p. 591-596.

Martinez, A., and V. Moreno, 1996, An oil spill monitoring system based on SAR images: Spill Science & Technology Bulletin, v. 3, p. 65-71.

Meheni, Y., R. Guerin, Y. Benderitter, and A. Tabbagh, 1996, Subsurface DC resistivity mapping: approximate 1-D interpretation: Journal of Applied Geophysics, v. 34, p. 255-269.

Mendoza, R. E., 1998, Hydrocarbon Leaching, Microbial Population, and Plant Growth in Soil Amended with Petroleum: Bioremediation Journal, v. 1, p. 223 - 231.

Modin, I. N., V. A. Shevnin, A. A. Bobatchev, D. K. Bolshakov, D. A. Leonov, and M. L. Vladov, 1997, Investigations of oil pollution with electrical prospecting methods: In: Proceedings of the 3rd EEGS-ES
Meeting, p. 267-270.

Momeni, M., and M. R. Saradjian, 2007, Evaluating NDVI-based emissivities of MODIS bands 31 and 32 using emissivities derived by Day/Night LST algorithm: Remote Sensing of Environment, v. 106, p. 190-198.

Morard, P., and J. Silvestre, 1996, Plant injury due to oxygen deficiency in the root environment of soilless culture: A review: Plant and Soil, v. 184, p. 243-254.

NAM, 2006, Overview Drawing in place and monitoring boreholes (1:500): Nederlandse Aardolie Maatschappij

Nie, Z. D., J. G. Han, L. D. Zhang, and J. H. Li, 2007, Applications of near infrared reflectance spectroscopy technique (NIRS) to grassland ecology research: Spectroscopy and Spectral Analysis, v. 27, p. 691-696.

Noomen, M. F., 2007, Hyperspectral reflectance of vegetation affected by underground hydrocarbon gas seepage, International Institute for Geo-information Science & Earth Observation, ITC, Enschede, 151 p.

Noomen, M. F., K. L. Smith, J. J. Colls, M. D. Stevens, A. K. Skidmore, and F. D. van der Meer, 2008, Hyperspectral indices for detecting changes in canopy reflectance as a result of underground natural gas leakage: International Journal of Remote Sensing, p. 22.

Onwurah, I. N. E., V. N. Ogugua, N. B. Onyike, A. E. Ochonogor, and O. F. Otitoju, 2007, Crude oil spills in the environment, effects and some innovative clean-up biotechnologies: International Journal of Environmental Research, v. 1, p. 307-320.

Orlov, D. S., I. M. Ammosova, and E. A. Bocharnikova, 1993, Remote monitoring of oil-polluted soils using soil reflectance spectra: CIS Selected Papers: Optical Monitoring of the Environment, p. 321-325.

Palacky, G. V., 1987, Resistivity characteristics of geologic targets: in Electromagnetic Methods in Applied Geophysics, v. 1, p. 53-129.

Petrovic, A., S. D. Khan, and H. S. Chafetz, 2008, Remote detection and geochemical studies for finding hydrocarbon-induced alterations in Lisbon Valley, Utah: Marine and Petroleum Geology, v. 25, p. 696-705.

Pettersson, J. K., and D. C. Nobes, 2003, Environmental geophysics at Scott Base: ground penetrating radar and electromagnetic induction as tools for mapping contaminated ground at Antarctic research bases: Cold Regions Science and Technology, v. 37, p. 187-195.

Pitas, I., and A. N. Venetsanopoulos, 1993, KNOWLEDGE-BASED IMAGE-ANALYSIS FOR GEOPHYSICAL INTERPRETATION: Journal of Intelligent & Robotic Systems, v. 7, p. 115-137.

Pollard, S. J. T., S. E. Hrudey, M. Rawluk, and B. J. Fuhr, 2004, Characterisation of weathered hydrocarbon wastes at contaminated sites by GC-simulated distillation and nitrous oxide chemical ionisation GC/MS, with implications for bioremediation: Journal of Environmental Monitoring, v. 6, p. 731-718.

PSA, 2008, Preventing environmental damage Norway, Petroleum Safety Authority, Norway.

Readman, J. W., S. W. Fowler, J.-P. Villeneuve, C. Cattini, B. Oregioni, and L. D. Mee, 1992, Oil and combustion-product contamination of the Gulf marine environment following the war: Nature v. 358 p. 662-665.

RITZ, M., H. ROBAIN, E. PERVAGO, Y. ALBOUY, C. CAMERLYNCK, M. DESCLOITRES, and A. MARIKO, 1999, Improvement to resistivity pseudosection modelling by removal of near-surface inhomogeneity effects : application to a soil system in south Cameroon: Geophysical prospecting v. 47, p. 85-101.

Rondeaux, G., M. Steven, and F. Baret, 1996, Optimization of Soil-Adjusted Vegetation Indices: Remote Sensing of Environment, v. 55, p. 95-107.

Samouëlian, A., I. Cousin, A. Tabbagh, A. Bruand, and G. Richard, 2005, Electrical resistivity survey in soil science: a review: Soil and Tillage Research, v. 83, p. 173-193.

Sauck, W. A., 1998, A conceptual model for the geoelectrical response of LNAPL plumes in granular sediments.: *In:* Proceedings of the Symposium on the Application of Geophysics to Engineering and Environmental Problems, p. 805-817.

Sauck, W. A., 2000, A model for the resistivity structure of LNAPL plumes and their environs in sandy sediments. : Journal of Applied Geophysics, v. 44, p. 151-165.

Sauck, W. A., and J. McNeil, 1994, Some problems associated with GPR detection of hydrocarbon plumes, Fifth International Conference on Ground Penetrating Radar (GPR'94).

Sauer, T. C., J. S. Brown, P. D. Boehm, D. V. Aurand, J. Michel, and M. O. Hayes, 1993, Hydrocarbon source identification and weathering characterization of intertidal and subtidal sediments along the Saudi Arabian coast after the Gulf War oil spill: Marine Pollution Bulletin, v. 27, p. 117-134.

Scholte, K. H., F. D. p. van der Meer, and S. B. p. Kroonenberg, 2005, Hyperspectral remote sensing and mud volcanism in Azerbaijan, Delft University of Technology, Delft, 147 p.

Schumacher, D., 1996, Hydrocarbon-induced alteration of soils and sediments: AAPG Memoir v. 66, p. pp. 71–89.

Schumacher, D., and M. A. Abrams, eds., 1996, Hydrocarbon Migration and its Near-Surface Expression: AAPG Memoir, v. 66, 445 p.

Schwinning, S., B. I. Starr, and J. R. Ehleringer, 2005, Summer and winter drought in a cold desert ecosystem (Colorado Plateau) part II: effects on plant carbon assimilation and growth: Journal of Arid Environments, v. 61, p. 61-78.

Serrano, A., M. Gallego, J. L. González, and M. Tejada, 2008, Natural attenuation of diesel aliphatic hydrocarbons in contaminated agricultural soil: Environmental Pollution, v. 151, p. 494-502.

Shevnin, V., O. Delgado-Rodríguez, A. Mousatov, E. Nakamura-Labastida, and A. Mejía-Aguilar, 2003, Oil pollution detection using resistivity sounding: Geofísica Internacional, v. 42
p. 613-622.

Shevnin, V., and O. Delgado, 2002, Application of resistivity sounding method for oil pollution study in urban and rural areas., *In:* Proceedings of the Symposium on the Application of Geophysics to Engineering and Environmental Problems.

Smith, K. L., M. D. Steven, and J. J. Colls, 2004a, Spectral responses of pot-grown plants to displacement of soil oxygen: International Journal of Remote Sensing, v. 25, p. 4395-4410.

Smith, K. L., M. D. Steven, and J. J. Colls, 2004b, Use of hyperspectral derivative ratios in the red-edge region to identify plant stress responses to gas leaks: Remote Sensing of Environment, v. 92, p. 207-217.

Steur, G. G. L., and W. Heijink, 1980, Bodemkaart van Nederland : algemene begrippen en indelingen : schaal 1 : 50.000: Wageningen, Stichting voor Bodemkartering (STIBOKA), 28 p.

Steven, M. D., 1998, The Sensitivity of the OSAVI Vegetation Index to Observational Parameters: Remote Sensing of Environment, v. 63, p. 49-60.

Steven, M. D., K. L. Smith, M. D. Beardsley, and J. J. Colls, 2006, Oxygen and methane depletion in soil affected by leakage of natural gas: European Journal of Soil Science, v. 57, p. 800-807.

Stichting voor Bodemkartering (STIBOKA), 1991, Bodemkaart van Nederland : 12 West Assen : schaal 1 : 50 000 : toelichting bij de kaartbladen: Wageningen, Stichting voor Bodemkartering (STIBOKA), 166 p.

Stuart, A. D., 1993, SOME APPLICATIONS OF INFRARED OPTICAL SENSING: Sensors and Actuators B-Chemical, v. 11, p. 185-193.

Stuart, B. H., 2004, Infrared spectroscopy : fundamentals and applications: Anaytical techniques in sciences ANTS;: Chichester etc., Wiley & Sons, 224 p.

Stummer, P., H. Maurer, and A. G. Green, 2004, Experimental design: Electrical resistivity data sets that provide optimum subsurface information: Geophysics, v. 69, p. 120-139.

Šumanovac, F., K. URUMOVIĆ, and I. DRAGIČEVIĆ, 2003, HYDROGEOLOGICAL MAPPING OF A MIOCENE AQUIFER BY TWO-DIMENSIONAL ELECTRICAL IMAGING: Rudarsko-geološko-naftni zbornik, v. 15, p. 13.

Topouzelis, K., V. Karathanassi, P. Pavlakis, and D. Rokos, 2007, Detection and discrimination between oil spills and look-alike phenomena through neural networks: Isprs Journal of Photogrammetry and Remote Sensing, v. 62, p. 264-270.

Urrestarazu, M., and P. C. Mazuela, 2005, Effect of slow-release oxygen supply by fertigation on horticultural crops under soilless culture: Scientia Horticulturae, v. 106, p. 484-490.

van der Meer, F., 2004, Analysis of spectral absorption features in hyperspectral imagery: International Journal of Applied Earth Observation and Geoinformation, v. 5, p. 55-68.

van der Meer, F., P. van Dijk, H. van der Werff, and H. Yang, 2002, Remote sensing and petroleum seepage: a review and case study: Terra Nova, v. 14, p. 1-17.

van der Meer, F. D., and S. M. de Jong, eds., 2001, Imaging spectrometry : basic principles and prospective applications: Remote sensing and digital image processing;4: Dordrecht etc., Kluwer Academic, 403 p.

van der Meer, F. D., H. Yang, and S. B. Kroonenberg, 2000, Imaging spectrometry and petroleum geology : hydrocarbon microseepage as a source of global methane production: In: 2000 Proceedings of the 28th International Symposium on Remote Sensing of the Environment : information for sustainable development, March 27-31 2000 Cape Town, South Africa. Cat. 5. pp. 36-39.

van der Meijde, M., H. M. A. van der Werff, P. F. Jansma, F. D. van der Meer, and G. J. Groothuis, 2008, A spectral-geophysical approach for detecting pipeline leakage: International Journal of Applied Earth Observation and Geoinformation, p. 24.

van der Meijde, M., H. M. A. van der Werff, J. F. Kooistra, and F. D. van der Meer, 2005, Pipeline leakage revealed by vegetation anomalies measured with reflectance spectroscopy: In: Proceedings of the international workshop Hanoi geoengineering 2005, 25 November 2005, Hanoi / ed. by Pham Huy Giao et al, Hanoi, Vietnam National University Publishing House, 2005. pp. 151-155.

van der Meijde, M., H. M. A. van der Werff, J. F. Kooistra, and F. D. van der Meer, 2006, Spatial - spectral approach from visualization of vegetation stress resulting from pipeline leakage: In: ISPRS 2006 : ISPRS mid-term symposium 2006 remote sensing : from pixels to processes, 8-11 May 2006, Enschede, the Netherlands. Enschede : ITC, 2006. 5 p.

van der Werff, H., M. van der Meijde, F. Jansma, F. van der Meer, and G. J. Groothuis, 2008, A spatial-spectral approach for visualization of vegetation stress resulting from pipeline leakage: Sensors, v. 8, p. 3733-3743.

van der Werff, H. M. A., W. H. Bakker, F. D. van der Meer, and W. Siderius, 2006, Combining spectral signals and spatial patterns using multiple Hough transforms: An application for detection of natural gas seepages: Computers & Geosciences, v. 32, p. 1334-1343.

White, D. C., 2007, HYPERSPECTRAL REMOTE SENSING OF CANOPY SCALE VEGETATION STRESS ASSOCIATED WITH BURIED GAS PIPELINES: Doctor of Philosophy thesis, Newcastle University, Newcastle, 306 p.

Winkelmann, K. H., 2005, On the applicability of imaging spectrometry for the detection and investigation of contaminated sites with particular consideration given to the detection of fuel hydrocarbon contaminants in soil: PhD thesis, Brandenburgischen Technischen Universität Cottbus, Cottbus, 243 p p.

Xu, D.-Q., G.-Q. Ni, L.-L. Jiang, Y.-T. Shen, T. Li, S.-L. Ge, and X.-B. Shu, 2008, Exploring for natural gas using reflectance spectra of surface soils: Advances in Space Research, v. 41, p. 1800-1817.

Xu, D. Q., G. Q. Ni, L. L. Jiang, T. Li, S. L. Ge, and X. B. Shu, 2007, Study on exploring for gas based on analysis of spectral absorption features: Spectroscopy and Spectral Analysis, v. 27, p. 2150-2154.

Yang, H., J. Zhang, F. van der Meer, and S. B. Kroonenberg, 1998, Geochemistry and field spectrometry for detecting hydrocarbon microseepage: Terra Nova, v. 10, p. 231-235.

Yuan L., J. T. Morris, and D. C. Yoch, 1990, Chronic Low Level Hydrocarbon Amendments Stimulate Plant Growth and Microbial Activity in Salt-Marsh Microcosms The Journal of Applied Ecology, v. 27, p. 159-171

Zarco-Tejada, P. J., A. Berjón, and J. R. Miller, 2004, Stress Detection in Crops with Hyperspectral Remote Sensing and Physical Simulation Models, Proceedings of the Airborne Imaging Spectroscopy Workshop, Bruges, Belgium.

Zirnig, W., D. Hausamann, and G. Schreier, 2002, High-Resolution Remote Sensing Used to Monitor Natural Gas Pipelines, Earth Observation Magazine, Roland Mangold.

Appendices

Appendix 1: *Correlation plots of OSAVI and NDVI indices during and after flight, showing almost no correlation*

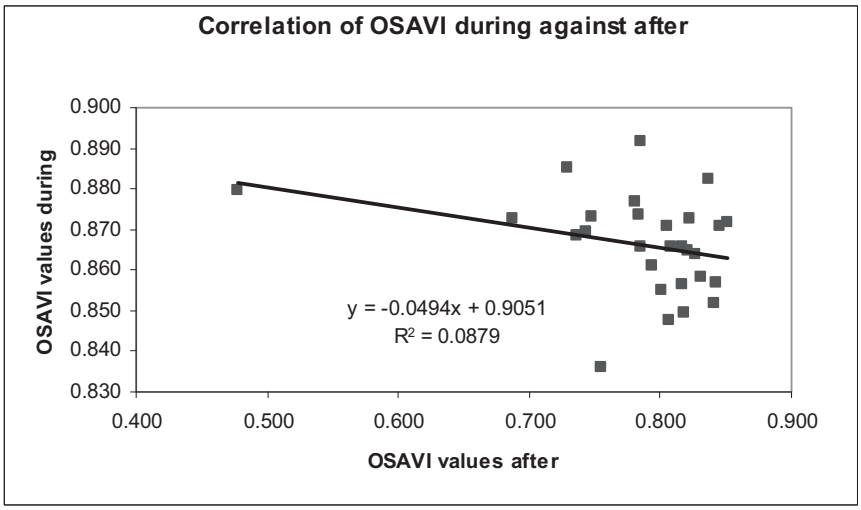

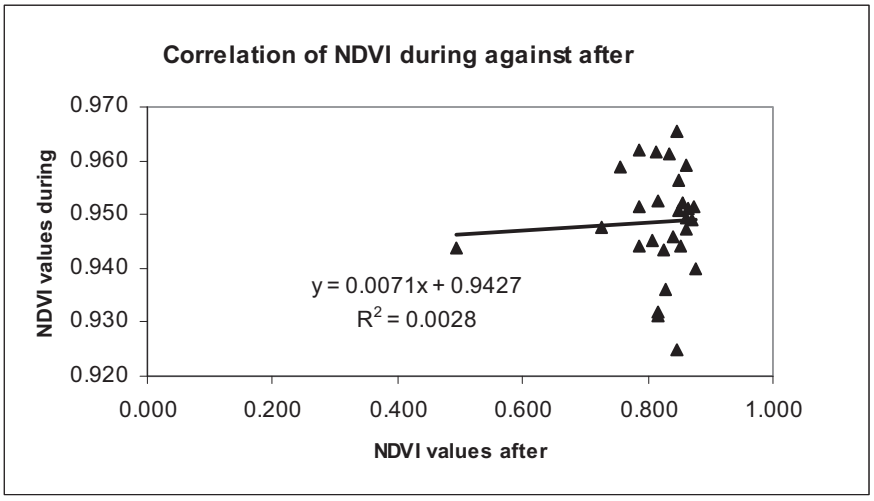

Appendix 2: *Spectra (MIR-wet) comparison of samples at centre of plume with that of distilled water from 2m-4m depth. Note that each spectrum represents 0.5m depth of sample within the borehole*

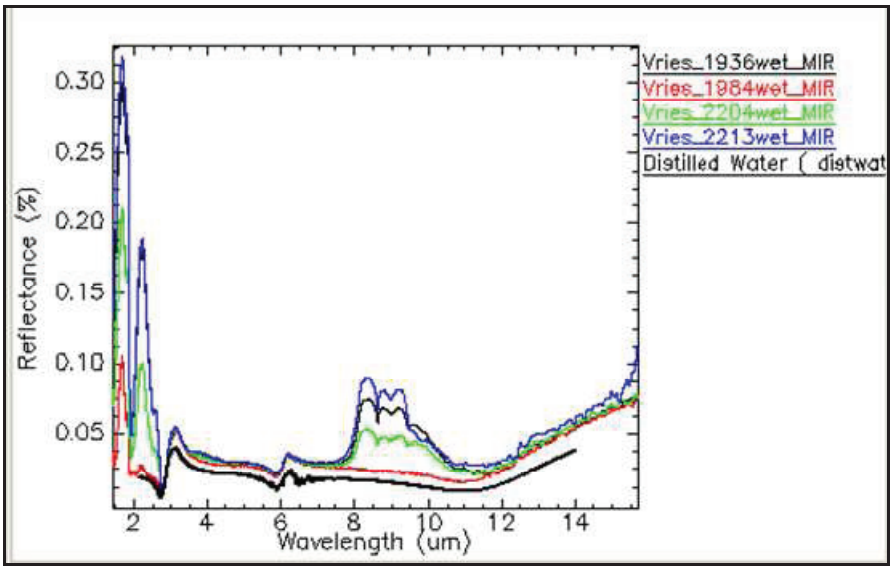

Appendix 3: *Spectra (MIR -wet) comparison of samples at centre of plume with that of distilled water from 4m-6m depth. Note that each spectrum represents 0.5m depth of sample within the borehole*

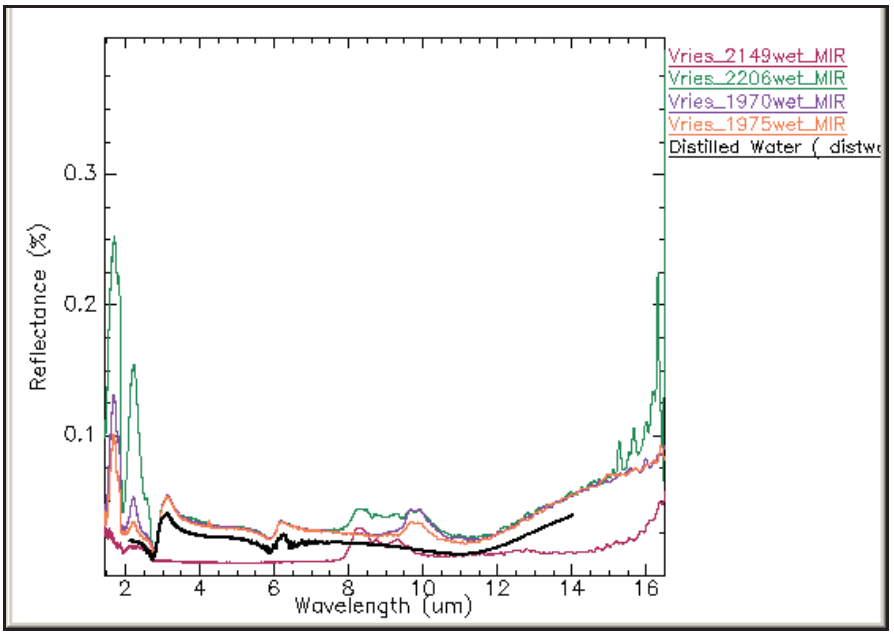

Appendix 4*: Spectra (MIR-wet) comparison of samples at centre of plume with that of distilled water from 6m-8m depth. Note that each spectrum represents 0.5m depth of sample within the borehole*

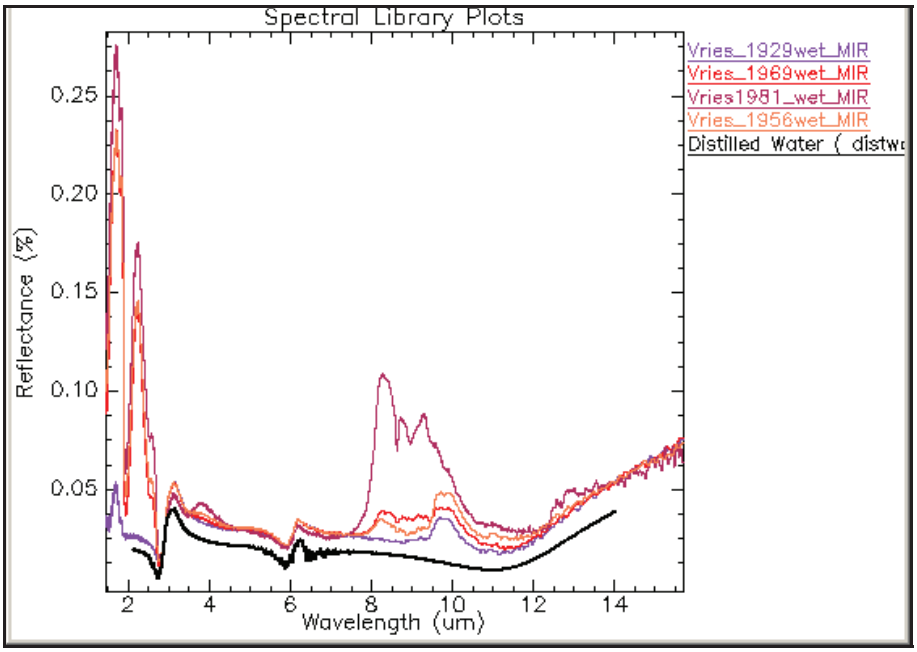

Appendix 5: *Continuum removed spectra showing differences in spectra with distilled water from borehole at the side of the plume*

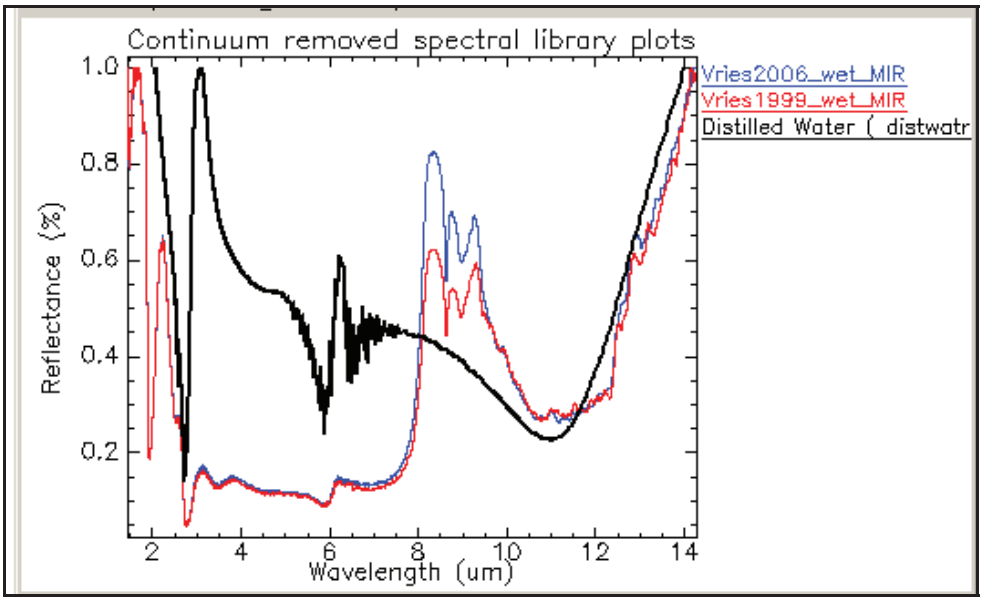

Appendix 6: *Spectra (MIR-wet) comparison of samples at the side of the plume with that of distilled water from 4m-8m depth. Note that each spectrum represents 0.5m depth of sample within the borehole*

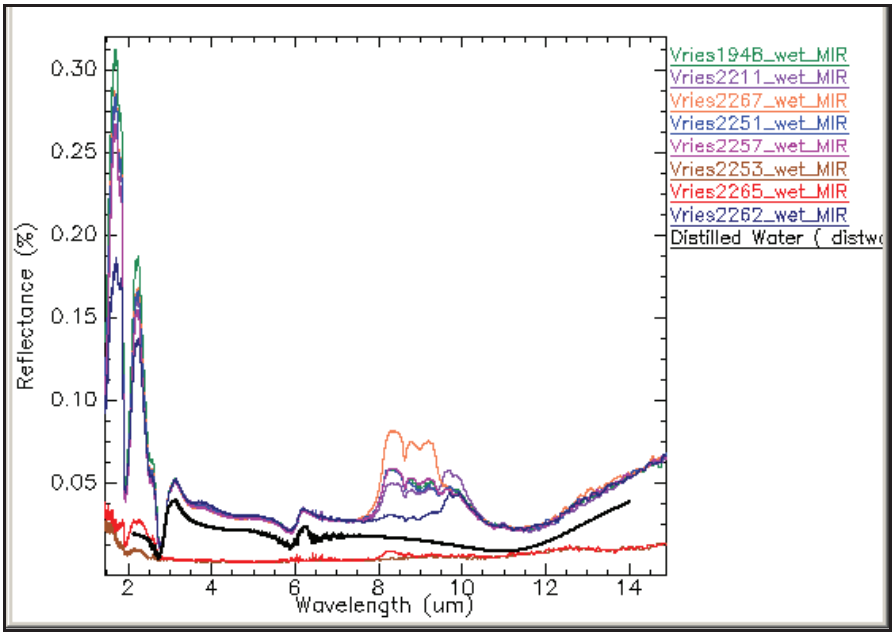

Appendix 7: *Spectra (SWIR -wet) comparison of samples at the centre of the plume with that of soil from 4-8m depth. Note that each spectrum represents 0.5m depth of sample within the borehole*

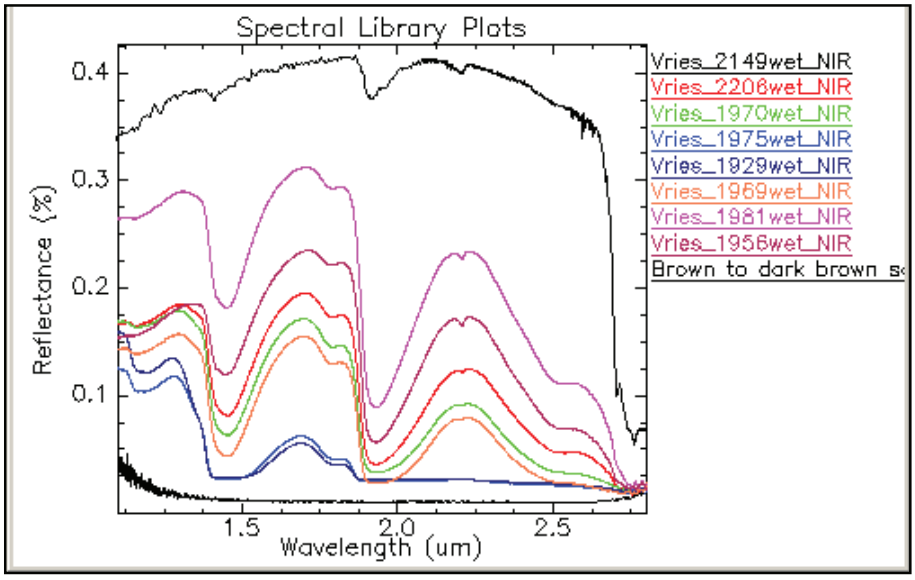

Appendix 8: *Spectra (SWIR -wet) comparison of samples at the side of the plume with that of soil from 0-8m depth. Note that each spectrum represents 0.5m depth of sample within the borehole*

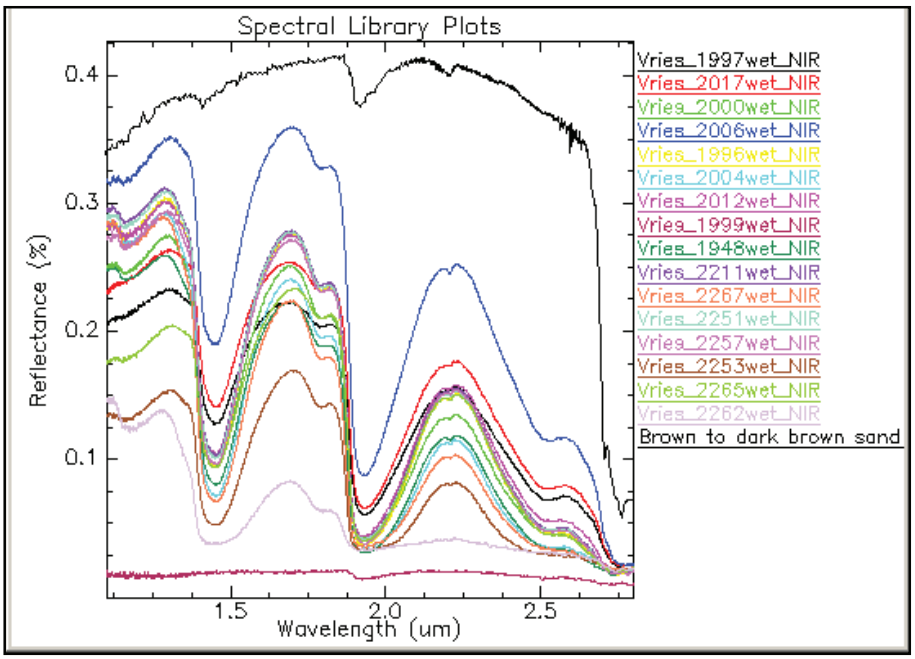

Appendix 9: *Spectra (MIR-dry) comparison of samples at the centre of the plume with that of soil from the surface to 2m depth. Note that each spectrum represents 0.5m depth of sample within the borehole*

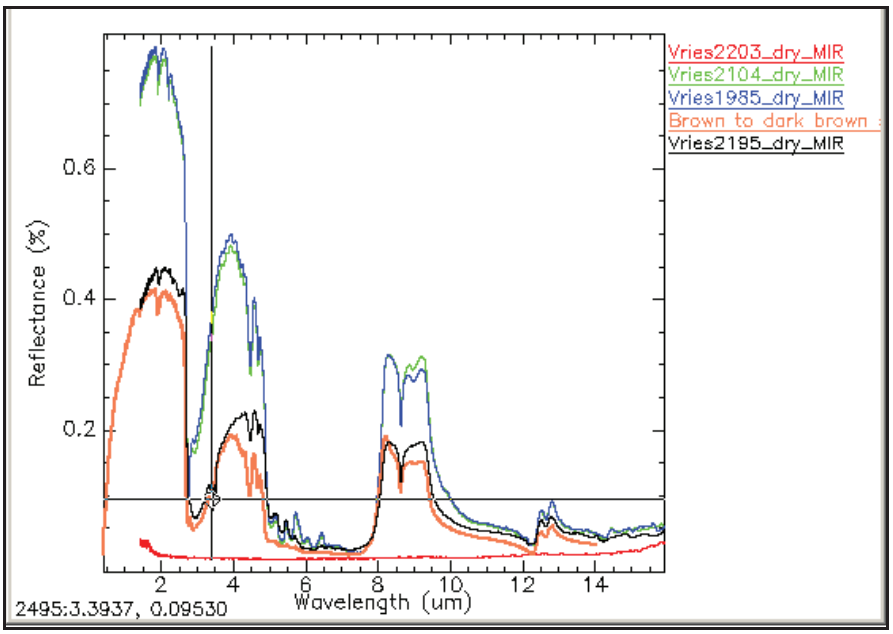

Appendix 10: *Spectra (MIR-dry) comparison of samples at the centre of the plume with that of soil from 2-8m depth. Note that each spectrum represents 0.5m depth of sample within the borehole*

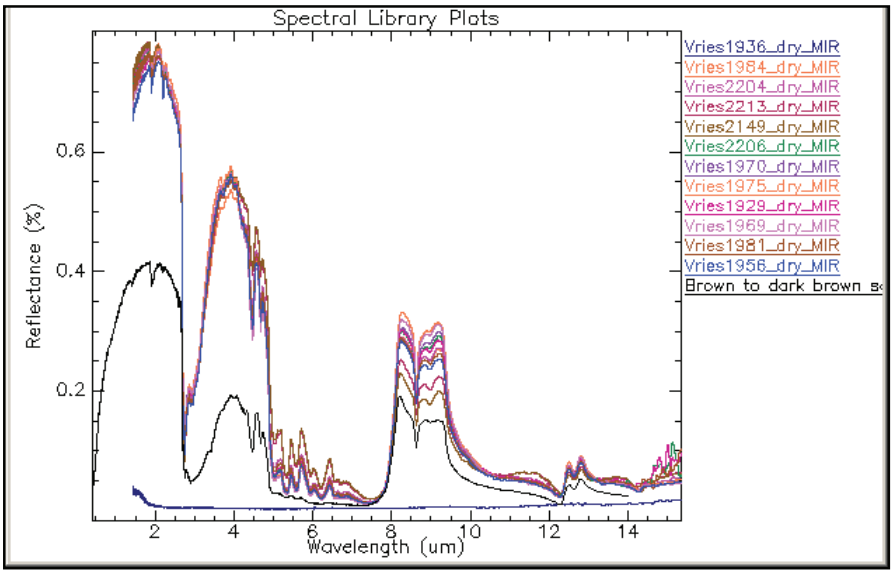

Appendix 11: *Spectra (MIR-dry) comparison of samples at the side of the plume with that of soil spectrum from a standard library from the surface to 8m depth*

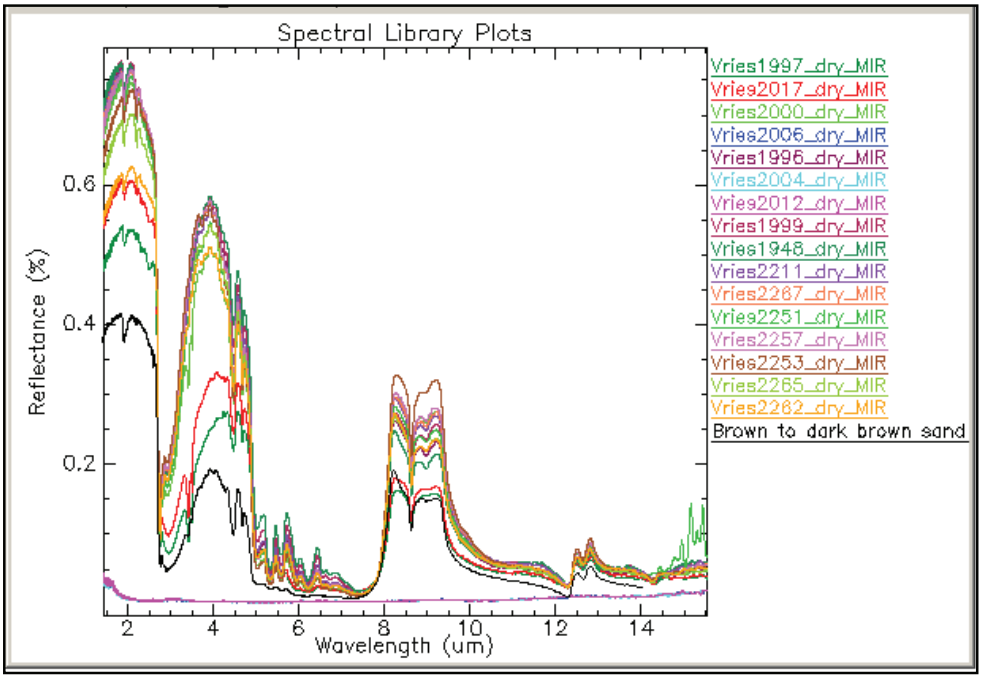

Appendix 12: *Spectra (SWIR-dry) comparison of samples at the centre of the plume with that of soil spectrum from a standard library from the surface to 8m depth.*

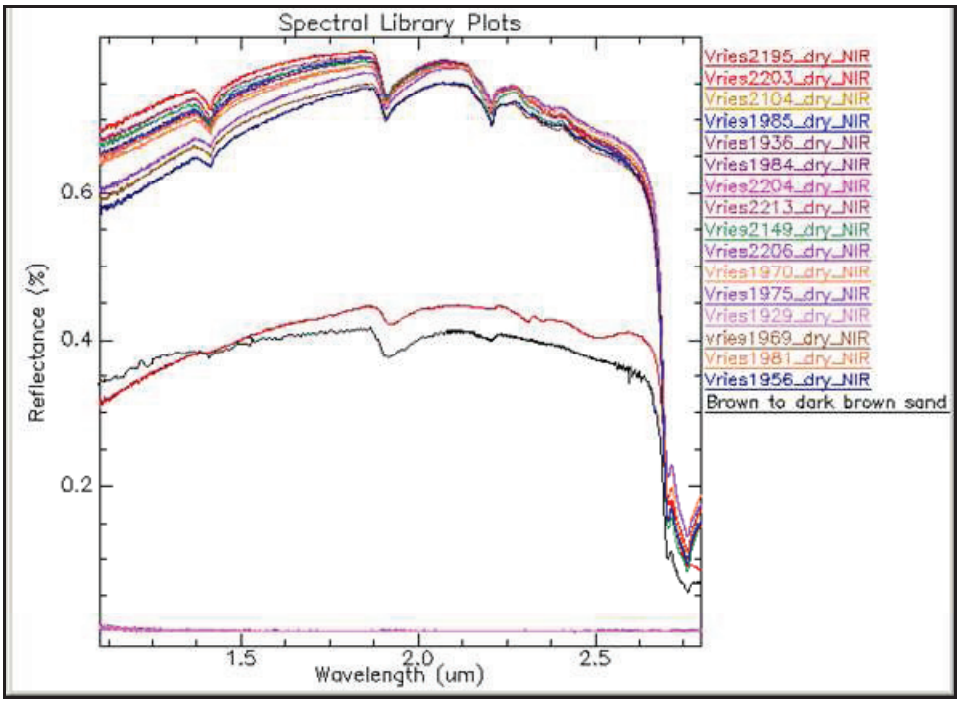

Appendix 13: *Spectra (SWIR-dry) comparison of samples at the side of the plume with that of soil spectrum from a standard library from the surface to 8m depth.*

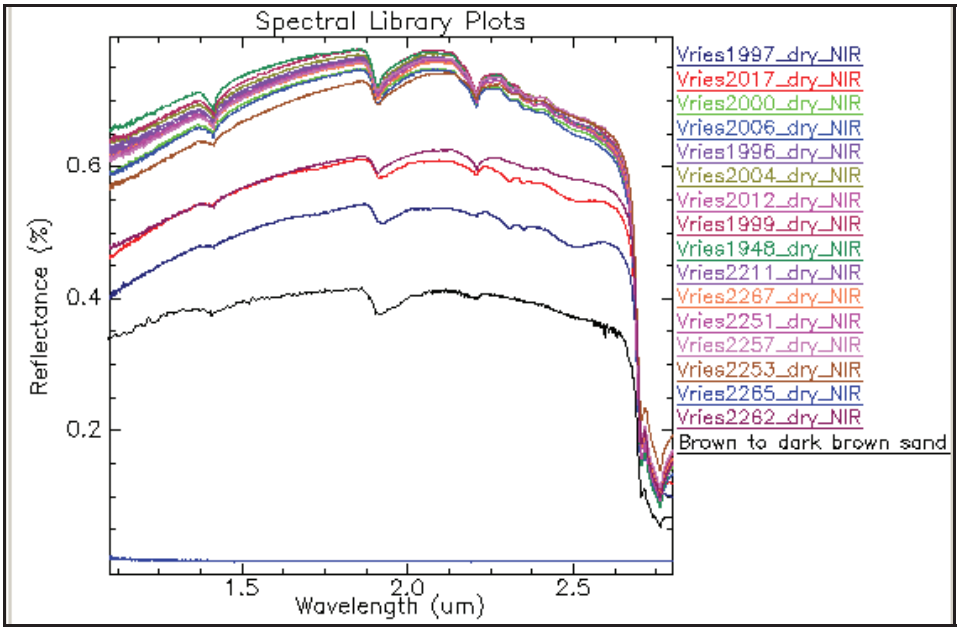

Appendix 14: *Spectra showing differences in absorption features at the 3.4µm wavelength. Thick red spectrum is from centre of plume BH, thick black is distilled water and the rest are from the side of plume BH. Difference is in oval shape.*

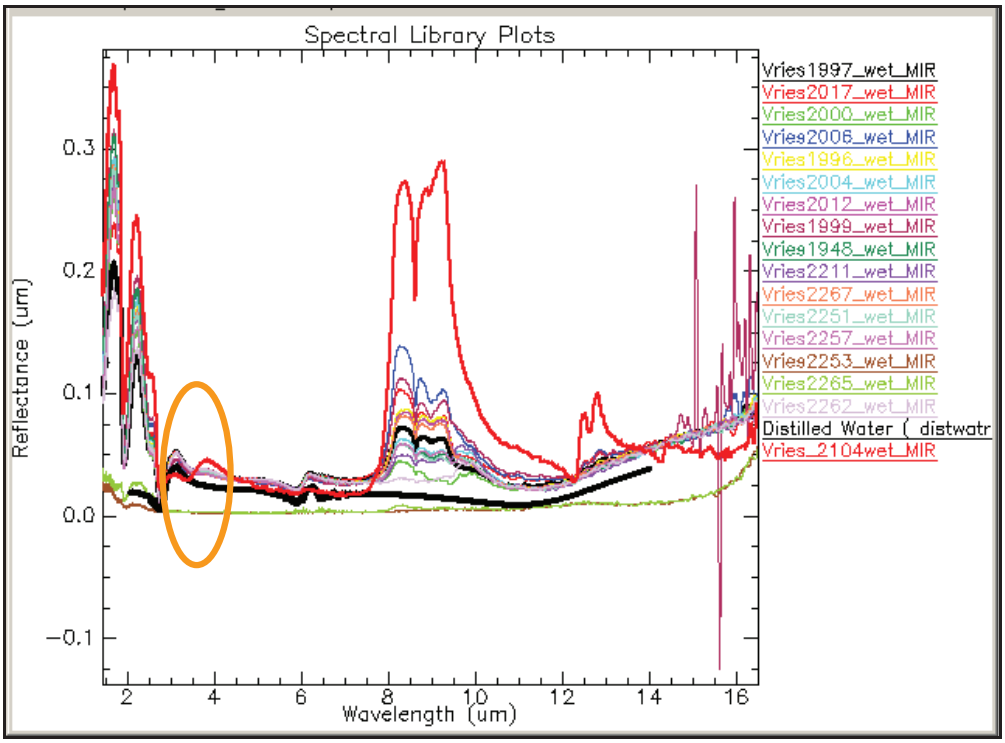

Appendix 15: *Continuum removed spectrum as shown for absorption feature analysis (absorption band depth) in the DISPEC tool embedded in ENVI*

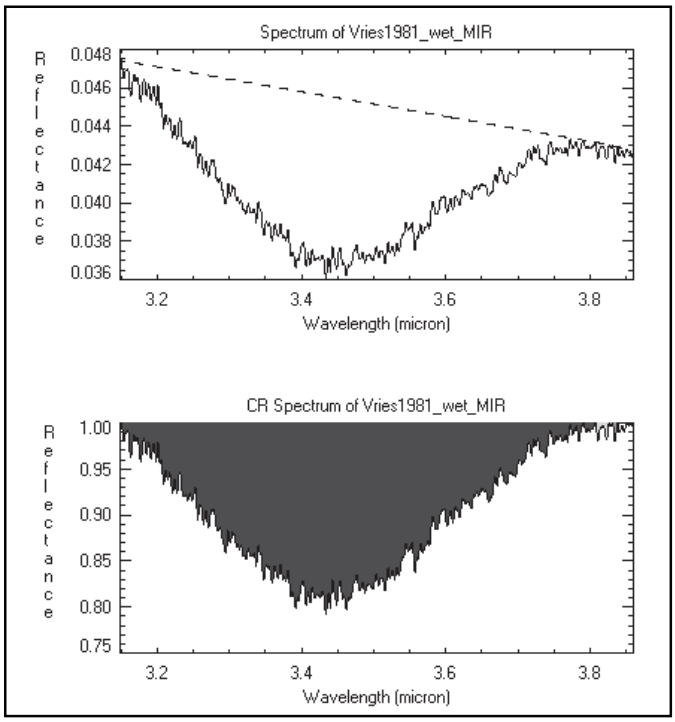

Absorption band depth D = 1-(R_b /R_c);

R_b = is the reflectance at the band bottom

R_c = is the reflectance of the continuum at the same wavelength as Rb (Green and Graig, 1985); cited in (van der Meer, 2004)

Appendix 16: *Wet and MIR absorption feature parameters of samples from the centre of plume borehole*

Sample number	Wavelength Position	Absorption band depth	Width	Area	Asymmetry	BH-depth
Vries2195_wet_MIR	3.427	0.256	0.08823	0.03044	-0.30750	0.5
Vries2203_wet_MIR	3.423	0.123	0.17409	0.02291	-0.57660	1.0
Vries2104_wet_MIR	3.425	0.272	0.30001	0.08629	0.08499	1.5
Vries1985_wet_MIR	0.000	0.000	0.00000	0.00000	0.00000	2.0
Vries1936_wet_MIR	0.000	0.000	0.00000	0.00000	0.00000	2.5
Vries1984_wet_MIR	0.000	0.000	0.00000	0.00000	0.00000	3.0
Vries2204_wet_MIR	0.000	0.000	0.00000	0.00000	0.00000	3.5
Vries2213_wet_MIR	0.000	0.000	0.00000	0.00000	0.00000	4.0
Vries2149_wet_MIR	0.000	0.000	0.00000	0.00000	0.00000	4.5
Vries2206_wet_MIR	0.000	0.000	0.00000	0.00000	0.00000	5.0
Vries1970_wet_MIR	0.000	0.000	0.00000	0.00000	0.00000	5.5
Vries1975_wet_MIR	0.000	0.000	0.00000	0.00000	0.00000	6.0
Vries1929_wet_MIR	0.000	0.000	0.00000	0.00000	0.00000	6.5
Vries1969_wet_MIR	0.000	0.000	0.00000	0.00000	0.00000	7.0
Vries1981_wet_MIR	3.434	0.208	0.33859	0.06797	-0.12200	7.5
Vries1956_wet_MIR	0.000	0.000	0.00000	0.00000	0.00000	8.0

Appendix 17: *Dry and MIR absorption feature parameters of samples from the side of plume borehole*

Sample number	Wavelength position	Absorption band depth	Width	Area	Asymmetry	BH-depth
Vries1997_dry_MIR	3.420	0.349	0.05356	0.02495	-0.00990	0.5
Vries2017_dry_MIR	3.419	0.341	0.11659	0.02390	-0.06640	1.0
Vries2000_dry_MIR	3.418	0.152	0.04175	0.00758	0.38857	1.5
Vries2006_dry_MIR	0.000	0.000	0.00000	0.00000	0.00000	2.0
Vires1996_dry_MIR	0.000	0.000	0.00000	0.00000	0.00000	2.5
Vries2004_dry_MIR	0.000	0.000	0.00000	0.00000	0.00000	3.0
Vries2012_dry_MIR	0.000	0.000	0.00000	0.00000	0.00000	3.5
Vries1999_dry_MIR	0.000	0.000	0.00000	0.00000	0.00000	4.0
Vries1948_dry_MIR	0.000	0.000	0.00000	0.00000	0.00000	4.5
Vries2211_dry_MIR	0.000	0.000	0.00000	0.00000	0.00000	5.0
Vries2267_dry_MIR	0.000	0.000	0.00000	0.00000	0.00000	5.5
Vries2251_dry_MIR	0.000	0.000	0.00000	0.00000	0.00000	6.0
Vries2257_dry_MIR	0.000	0.000	0.00000	0.00000	0.00000	6.5
Vries2253_dry_MIR	3.419	0.028	0.03465	0.00113	0.58962	7.0
Vries2265_dry_MIR	3.418	0.026	0.03860	0.00128	0.64591	7.5
Vries2262_dry_MIR	3.418	0.043	0.03623	0.00202	0.67998	8.0

These absorption features from the dried samples were not expected since they had been dried and if there were any hydrocarbons, they were expected to have evaporated.

Appendix 18: *Extracted resistivity and corresponding REP values along transect A-B*

Resistivity (Ohm-m)	REP values	Dist (m)
178.969	721.4	2.0
160.213	716.9	4.0
172.472	720.2	6.0
239.857	723.4	8.0
208.031	718.9	10.0
258.954	720.5	12.0
307.745	721.2	14.0
363.177	720.5	16.0
369.568	721.5	18.0
340.888	719.5	20.0
363.649	719.2	22.0
275.735	720.5	24.0
255.929	717.0	26.0
280.847	719.6	28.0
242.807	716.7	30.0
226.025	718.8	32.0
249.276	713.8	34.0
256.457	712.4	36.0
284.415	714.9	38.0
235.907	716.5	40.0
227.484	718.2	42.0
199.174	719.8	44.0
207.787	721.2	46.0
179.313	719.1	48.0
162.258	719.5	50.0
203.802	722.2	52.0
169.327	720.9	54.0
155.759	719.3	56.0
165.788	717.0	58.0
172.178	720.0	60.0
182.115	722.0	62.0
165.403	720.7	64.0
169.549	720.9	66.0
251.918	722.1	68.0
188.009	720.0	70.0
191.098	720.6	72.0
113.019	715.6	74.0
281.501	718.3	76.0
289.737	719.0	78.0

Appendix 19: *Resistivity plot and absorption band depth values with BH depth*

RES (Ohm-m)	Abs band depth	BH_depth
182.099	0.123	1.0
236.273	0.272	2.0
136.167	0.000	4.0
80.2786	0.000	5.0
61.9134	0.208	7.0
57.673	0.000	8.0

Appendix 20: *Chemical analysis of benzene quantities and absorption band depth ("quantities") values of borehole at the side of plume for both wet and dry samples*

BTEX quantities	BH-depth	Sample number	Wavelength position	Absorption band depth
0.025	0.5	Vries1997_wet_MIR	3.422	0.170
0.025	1.0	Vries2017_wet_MIR	3.452	0.171
0.025	1.5	Vries2000_wet_MIR	3.416	0.158
0.025	2.0	Vries2006_wet_MIR	3.452	0.194
0.025	2.5	Vries1996_wet_MIR	3.398	0.181
0.025	3.0	Vries2004_wet_MIR	3.488	0.157
0.350	3.5	Vries2012_wet_MIR	3.434	0.165
0.460	4.0	Vries1999_wet_MIR	3.428	0.188
0.180	4.5	Vries1948_wet_MIR	3.454	0.169
1.500	5.0	Vries2211_wet_MIR	3.480	0.139
1.300	5.5	Vries2267_wet_MIR	3.445	0.175
1.300	6.0	Vries2251_wet_MIR	3.441	0.164
0.460	6.5	Vries2257_wet_MIR	3.446	0.156
0.025	7.0	Vries2253_wet_MIR	0.000	0.000
0.025	7.5	Vries2265_wet_MIR	0.000	0.000
0.025	8.0	Vries2262_wet_MIR	3.454	0.163
0.025	0.5	Vries1997_dry_MIR	3.420	0.349
0.025	1.0	ries2017_dry_MIR	3.419	0.341
0.025	1.5	Vries2000_dry_MIR	3.418	0.152
0.025	2.0	Vries2006_dry_MIR	0.000	0.000
0.025	2.5	Vires1996_dry_MIR	0.000	0.000
0.025	3.0	Vries2004_dry_MIR	0.000	0.000
0.350	3.5	Vries2012_dry_MIR	0.000	0.000
0.460	4.0	Vries1999_dry_MIR	0.000	0.000
0.180	4.5	Vries1948_dry_MIR	0.000	0.000
1.500	5.0	Vries2211_dry_MIR	0.000	0.000
1.300	5.5	Vries2267_dry_MIR	0.000	0.000
1.300	6.0	Vries2251_dry_MIR	0.000	0.000
0.460	6.5	Vries2257_dry_MIR	0.000	0.000
0.025	7.0	Vries2253_dry_MIR	3.419	0.028
0.025	7.5	Vries2265_dry_MIR	3.418	0.026
0.025	8.0	Vries2262_dry_MIR	3.418	0.043

Appendix 21: *Chemical analysis of benzene quantities and absorption band depth ("quantities") values of borehole at the centre of plume for both wet and dry samples*

BTEX quantities	BH-depth	Sample number	Wavelength position	Absorption band depth
0.025	0.5	Vries2195_wet_MIR	3.427	0.256
0.025	1.0	Vries2203_wet_MIR	3.423	0.123
0.025	1.5	Vries2104_wet_MIR	3.425	0.272
0.025	2.0	Vries1985_wet_MIR	0.000	0.000
0.025	2.5	Vries1936_wet_MIR	0.000	0.000
0.025	3.0	Vries1984_wet_MIR	0.000	0.000
0.025	3.5	Vries2204_wet_MIR	0.000	0.000
0.025	4.0	Vries2213_wet_MIR	0.000	0.000
0.025	4.5	Vries2149_wet_MIR	0.000	0.000
0.210	5.0	Vries2206_wet_MIR	0.000	0.000

0.025	5.5	Vries1970_wet_MIR	0.000	0.000
0.025	6.0	Vries1975_wet_MIR	0.000	0.000
0.025	6.5	Vries1929_wet_MIR	0.000	0.000
0.025	7.0	Vries1969_wet_MIR	0.000	0.000
0.025	7.5	Vries1981_wet_MIR	3.434	0.208
0.025	8.0	Vries1956_wet_MIR	0.000	0.000
0.025	0.5	Vries2195_dry_MIR	3.420	0.331
0.025	1.0	Vries2203_dry_MIR	0.000	0.000
0.025	1.5	Vries2104_dry_MIR	3.417	0.032
0.025	2.0	Vries1985_dry_MIR	0.000	0.000
0.025	2.5	Vries1936_dry_MIR	0.000	0.000
0.025	3.0	Vries1984_dry_MIR	0.000	0.000
0.025	3.5	Vries2204_dry_MIR	0.000	0.000
0.025	4.0	Vries2213_dry_MIR	0.000	0.000
0.025	4.5	Vries2149_dry_MIR	0.000	0.000
0.210	5.0	Vries2206_dry_MIR	0.000	0.000
0.025	5.5	Vries1970_dry_MIR	0.000	0.000
0.025	6.0	Vries1975_dry_MIR	0.000	0.000
0.025	6.5	Vries1929_dry_MIR	0.000	0.000
0.025	7.0	Vries1969_dry_MIR	0.000	0.000
0.025	7.5	Vries1981_dry_MIR	0.000	0.000
0.025	8.0	Vries1956_dry_MIR	0.000	0.000

Appendix 22: *Illustrations from laboratory experiments*

a: shows how each bottled sample was thoroughly mixed before spectroscopic measurement

b: a few samples levelled to the brim in a petri dish

c: the FTIR spectrometer from Bruker Optics used for the mid- and near- infrared measurements

d: dried samples which were later crushed and measured to obtain dry spectra